Preparation and Structure of Ultra-Thin Zinc Oxide Films on Pt(111), Ag(111) and Cu(111)

Dissertation

Zur Erlangung des akademischen Grades des

Doktors der Naturwissenschaften (Dr. rer. nat.)

eingereicht im Fachbereich Biologie, Chemie, Pharmazie

der Freien Universität Berlin

Vorgelegt von

Bo-Hong Liu

Berlin 2015

Diese Arbeit wurde von März 2011 bis Dezember 2015 am Fritz-Haber-Institut der Max-Planck-Gesellschaft in der Abteilung Chemische Physik unter Anleitung von Herrn Prof. Dr. H.-J. Freund angefertigt.

Gutachter:

1. Prof. Dr. Hans-Joachim Freund
2. Prof. Dr. Thomas Risse
3. Prof. Dr. Sebastian Hasenstab-Riedel
4. Prof. Dr. P. Heretsch
5. Dr. Peter Clawin

Disputation am: 07.12.2015

Acknowledgement

I am fortunate to work in such an intelligent and international environment of the chemical physics department. I am grateful to all the colleagues: Bing Yang, Yulia Martynova, Emre Emmez, Xin Yu, Yi Cui, Qiushi Pan, Heloise Tissot, Xuefei Weng, Yi Pan, Xiang Shao, Christian Stieler, Leandro Pascua, Fernando Stavale, Niklas Nilius, Stefanie Stuckenholz, Christin Büchner, Leonid Lichtenstein, Kristen Burson, Mattias Peter, Casey O'Brien, Francisco Ivars-Barceló, Jan Seifert, Petr Dementyev, Francesca Mirabella, Karl-Heinz Dostert, Osman Karslioglu, Xin Song, Elena Primorac, Felix Feiten, Earl Davis, Hengshan Qiu, Zongfang Wu, Yuichi Fugimori, Florencia Calaza, Bill Kaden, Huifeng Wang, Alessandro Sala, Damien Cornu, Hagen Klemm and Francesca Genuzio, and the list goes on and on. To all of you whether or not I have named you here, you have shaped me into who I am today. I am happy about that, and grateful to all of you.

I have made quite a number of local friends, from my flat mates to people in the badminton club. We shared many interesting moments together. I deeply appreciate all the friendships, and I am grateful to them for helping me to get to know Berlin and Germany from many different prespectives.

I am deeply grateful to the unconditional love from my family. The remote yet genuine love from my parents has always been an important support over the years. Life would be even more difficult, without my sister Yu-Chun and my new brother-in-law Chris, who also live in Germany. I am grateful to them not only for helping me on trivial everyday things, but even more so, for opening their lives to me with love and patience.

Abstract

Thin oxide films grown on metal supports are often used in surface science studies aimed at understanding the surface properties of oxide metal surfaces. Besides the general interest in ultrathin oxide films as two-dimensional systems, the interest to ZnO films has recently been reinforced due to the observations of interlayer structural relaxations resulting in graphene-like structures. The presented work addresses preparation and atomic structure of ultrathin zinc oxide films on metal single crystal supports, namely Pt(111), Ag(111) and Cu(111), using zinc physical vapor deposition. On all substrates, the film grows in (0001) orientation. On Pt(111), the film grows in a layer-by-layer mode, starting from a monolayer, ultimately reaching surface structures characteristic for ZnO(0001) single crystal surfaces. On Ag(111), the films form bilayer structures (i.e. two ZnO sheets) from the onset. Further growth to obtain multilayer films turned out to be very difficult, indicating some sort of "self-limiting" growth. The latter behavior is observed on a Cu(111) substrate as well. In contrast to the films grown on Ag(111), all films on Pt(111) expose substantial amounts of hydroxyls. It therefore appears that surface restructuring of otherwise polar unstable ZnO(0001) surfaces may proceed more efficiently through hydroxylation rather than relaxation, provided that hydrogen atoms are available in the system. Apparently, Pt readily dissociates hydrogen and provides hydrogen atoms to form surface hydroxyls. Zinc oxide films on Pt(111) are found to exhibit a very rich structural variety depending on exposure conditions. Such a behavior is not observed on either Ag(111) or Cu(111), thus indicating strong support effects. The structural diversity of the ZnO films observed here suggests that ZnO-based catalytic materials must be considered as very dynamic, and their surface structure critically depend on the reaction conditions.

Zusammenfassung

Dünne, auf Metallsubstraten gewachsene Oxidschichten werden oft in Studien der Oberflächenphysik und –chemie verwendet, um die Eigenschaften von Metalloxid-Oberflächen auf atomistischem Niveau zu verstehen. Neben dem allgemeinen Interesse an ultradünnen Oxidschichten als zweidimensionale Systeme hat sich das Interesse an ZnO-Schichten in letzter Zeit aufgrund der Beobachtung von strukturellen Zwischenschichtrelaxationen, die zu graphenartigen Strukturen führen verstärkt. Die vorliegende Arbeit behandelt die Präparation und Untersuchung der atomaren Struktur von ultradünnen Zinkoxidfilmen, die durch Gasphasendeposition von metallischen Zink auf einkristallinen metallischen Trägern, nämlich Pt(111), Ag(111) und Cu(111) gewachsen wurden. Auf allen Substraten wächst der Film in (0001)-Orientierung. Auf Pt(111) wächst der Film in einem Schicht-für-Schicht-Modus, ausgehend von einer Monoschicht erhält man bei großen schichtdichen Oberflächenstrukturen, die charakteristisch für ZnO(0001)-Einkristalloberflächen sind. Auf Ag(111) bilden die Filme von Beginn an Doppelschichtstrukturen (d.h. zwei ZnO-Schichten). Weiteres Wachstum zu Mehrschichtfilmen erwies sich als sehr schwierig, was auf eine Art "selbstbegrenzendes" Wachstum hinweist. Dieses Verhalten wurde auch auf Cu(111)-Substraten beobachtet. Im Gegensatz zu den auf Ag(111) gewachsenen Filmen weisen alle auf Pt(111) gewachsenen Filme wesentliche Mengen an Hydroxyl-Gruppen auf. Dies legt nahe, dass die Umstrukturierung der ansonsten instabilen polaren ZnO(0001)-Oberflächen effizienter durch Hydroxylierung als durch Rekonstruktion vor sich geht, vorausgesetzt, dass Wasserstoffatome in dem System verfügbar sind. Offenbar dissoziiert Pt Wasserstoff und stellt Wasserstoffatome zur Verfügung, um Oberflächen-Hydroxyl-grouppen zu bilden. Es wurde ein sehr reiches, von den Expositionsbedingungen abhängiges strukturelles Phasendiagramm für Zinkoxid-Schichten auf Pt(111) beobachtet. Solch ein Verhalten wird weder auf Ag(111) oder Cu(111) beobachtet, was auf den starken Einfluss des Trägermaterials hinweist. Die Strukturvielfalt der hier beobachteten ZnO-Filme legt nahe, dass auf ZnO basierende katalytische Materialien als sehr dynamische Materialien betrachtet werden müssen, deren Oberflächenstruktur empfindlich von den Reaktionsbedingungen abhängt.

Table of Contents

Chapter 1 Introduction

Zinc oxide (ZnO) based compounds have many interesting electronic, optical and structural properties [1], resulting in many application in, e.g. electronics, photovoltaics, sensors, and catalysis. In addition, ZnO is used in many industrial manufacturing processes, including paints, cosmetics, pharmaceuticals, plastics, batteries, rubber, etc. [2]. As a result, zinc oxide has been a material that attracts intense fundamental and applied research interest.

Zinc oxide nano-objects exhibit a wide structural variety. The variety comes from the kinetic control of the growth rate of different facets [3]. In general, the area of lower index facets tends to be maximized due to the lower surface energy. By inducing defects and/or controlling the growth condition after the initial period of nucleation and incubation, a crystallite commonly develops into a three-dimensional object with well-defined, low index crystallographic faces. A huge collection of TEM images of such nano-structures of ZnO, in particular, nano-belts was reported in the literature [3, 4].

Gas sensing is a prominent application of zinc oxide [5]. It is used for fabricating toxic and combustible gas sensor. The gas sensing mechanism involves chemisorption of oxygen of the oxide surface followed by charge transfer during the redox reaction between chemisorbed oxygen and target gas molecules. This leads to a change in surface resistance, which can be used as a read-out for gas sensing. Since the probing reaction happens at the solid-gas interface, its structure and properties affect the performance profoundly. To gain more understanding, extensive knowledge about the interplay between surface structure and reactivity is necessary.

Catalysis is another important application of zinc oxide. It is an important ingredient of the industrial catalyst for methanol synthesis. The $Cu/ZnO/Al_2O_3$ catalyst that is almost exclusively used nowadays was developed by Imperial Chemical Industries (ICI). Despite the widespread use of this catalyst, the reaction mechanism is not yet fully understood, and has been a focus of research activity for decades [6-16].

Surface science has proven to be an important tool for studying heterogeneous catalysis [17, 18]. Traditional heterogeneous catalysis studies suffer from an information gap between

phenomenological data, e.g., reaction rates, apparent activation energies, order of reaction, etc., and the properties of the catalyst such as surface structure, chemical composition and electronic structure [19]. With the help of surface science tools, the influence of a single parameter, such as change of temperature or addition of an ad-layer, on surface properties, such as morphology and electronic structure can be studied. Traditionally, metal or metal oxide single crystal surfaces are used for this purpose. A relatively new approach is to adopt ultrathin metal oxide films, which circumvents charging effects that interfere with experiments such as photoelectron spectroscopy.

Indeed, ultrathin metal oxide film exhibits many unique properties in its own right [20, 21]. On one hand, they are flexible with respect to their structure and respond to external stimuli such as the chemical potential of the gas phase that they are exposed to. Another aspect is the controllable thickness. By controlling the thickness of an oxide layer, one has a unique opportunity to control charge transfer from the oxide-modified metal support to an adsorbate without using electrical control but by pure chemical means.

Moreover, thin oxide films were shown to be the active component of various model catalysts. $RuO_2(110)$ film grown on Ru(0001) is the active phase of low temperature CO oxidation[22-24]. Another example is the FeO/Pt(111), where initially grown bilayered FeO film transforms into a FeO_2 tri-layer phase under oxygen rich reaction condition, and catalyzes low temperature CO oxidation reaction through a Mars–van Krevelen type mechanism [25-27]. Such ultra-thin films may also be formed on the surfaces of oxide supported metal particles of heterogeneous catalyst as a result of so-called strong metal/support interaction.

A recent study on $Cu/ZnO/Al_2O_3$ catalysis, performed under industrial relevant condition, demonstrates that the copper particles are also partially covered by ZnO_x thin layer, which originates from the zinc oxide support. The new phase that is composed of a thin zinc oxide film and copper is accounted for the superior reactivity of Cu/ZnO system in methanol synthesis [13].

Beside the technological applications, ZnO is also an interesting model system for deeper understanding of physical principles of stabilization of polar surfaces. Basal planes of ZnO are classical systems for studying polar surfaces, and the corresponding dipole cancelation mechanism [28]. Along the [0001] direction, zinc oxide thin film obtains an inherent dipole moment, which diminishes as the film gets thinner. Down to a monolayer, the dipole moment of

the film is cancelled by relaxation between O-layer and Zn-layer, as predicted by DFT study for free standing ZnO sheet [29]. The depolarized ZnO phase was experimentally observed on Ag(111), by surface x-ray diffraction characterization [30]. This demonstrates the structural flexibility, which is unique for metal oxide ultrathin films. The observation of the new phase may lead to potentially new properties and applications, and therefore generates considerable research interests on the ultrathin zinc oxide film.

In order to gain a better understanding of the fundamental properties of zinc oxide material in the form of ultrathin film, in addition to the properties of single crystal surfaces, which can be mimicked by films that are above a critical thickness, preparation and structural characterization of ultrathin zinc oxide film on metal supports are necessary.

This thesis focuses on preparation and atomic structure of ultrathin ZnO film grown on metals. In chapter 2, the basic structural properties of zinc oxide and the property of its low index surface truncated from the single crystal are summarized. In addition, a literature survey of studies of metal supported ultrathin zinc oxide films is outlined. Afterwards, chapter 3 describes the setups and basic working principles of experimental tools that are used in this study.

In Chapter 4, the preparation of ultrathin zinc oxide film on Pt(111), Ag(111) and Cu(111) is reported. Further structure characterizations were reported in the first part of chapter 5, where infrared spectroscopy is applied to study surface hydroxylation of ultrathin zinc oxide film on different supports. The preference between depolarization and hydroxylation as the dipole cancelling mechanism depends on the metal substrate. In the second part of chapter 5, thermal stability of the hydroxyl group on the hydroxylated films is examined.

In chapter 6, it is shown that structure of ultra-thin zinc oxide film is even more diverse than known until now. This is in line with the structural variety observed in its nano-objects, which responds to the environment it was exposed to. In addition, the structural transformation of zinc oxide from one phase to another is recorded in situ by scanning tunneling microscopy.

Finally, chapter 7 reports the structural aspect of zinc oxide thin film based model catalyst for low temperature CO oxidation. Structures of the model catalysts are characterized before and after exposure to the reaction condition, for the sake of bridging the pressure gap.

This structural information is combined with previous reactivity measurements by Dr. Yulia Martynova and Dr. Qiushi Pan.

Chapter 2 Background

2.1 ZnO crystal structure

At ambient pressure and temperature, zinc oxide crystal adopts the Wurtzite structure, as shown in Figure 2-1a. This is a hexagonal lattice that belongs to space group $P6_3mc$. The tetrahedral coordination of this compound is a common indicator of sp^3 covalent bonding; however, the Zn-O bond possesses a rather strong ionic character. As a result, ZnO is borderline between a covalent and an ionic compound. The lattice parameters of the hexagonal unit cell are a = 3.2495 Å and c = 5.2069 Å [31]. The tetrahedral coordination also gives rise to a polar structure along the c axis. This polarity results in properties such as piezoelectricity and crystal polarization along the [0001] direction. The most common face terminations of ZnO are the polar, Zn-terminated [0001] and O-terminated [000$\bar{1}$] faces (c-axis oriented), and the non-polar [11$\bar{2}$0] (a-axis) and [10$\bar{1}$0] faces.

(a)　　　　　　　　(b)　　　　　　　　(c)
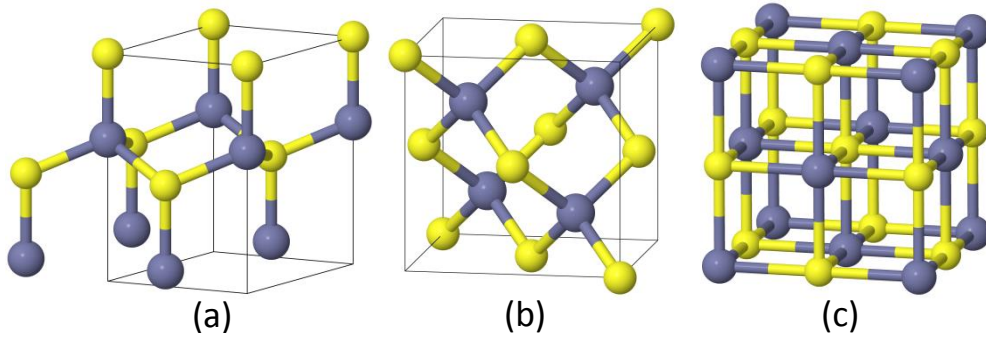
Figure 2-1. Unit cells of ZnO crystals, gray: zinc; yellow: oxygen. (a) Wurtzite structure. (b) Zinc blende structure. (c) Rock salt structure. Image courtesy of Xunhua Znao.

In addition to Wurtzite, ZnO also crystalizes in the cubic zinc blende and rock-salt structure. ZnO converts to rock salt structure at a pressure of about 10 GPa [32]; however, the zinc blende structure is favored only when grown on cubic substrates [33].

2.2 ZnO single crystal surfaces

Thanks to the low band gap (3.4 eV) of ZnO single crystals, standard surface science techniques, such as LEED, STM and XPS, can be applied to its surfaces in a fairly straightforward fashion. Most studies were performed on the surfaces along the (0001) direction, i.e. Zn terminated ZnO(0001) and O-terminated ZnO(000$\bar{1}$) surfaces [34, 35]. Other non-polar low

index surfaces, such as the $(10\bar{1}0)$ and $(11\bar{2}0)$, also attract plenty of research interest, because of their abundance in the nature.

2.2.1 The Zn-ZnO(0001) surface:

The structure of the ideal, unreconstructed Zn-ZnO(0001) surface is shown in Figure 2-2a. Even though IV-LEED measurement showed a moderate surface relaxation [36], the LEED pattern in Figure 2-2b shows no sign of reconstruction. Similar results were obtained from Helium atom scattering (HAS), where no peak other than that of the ideal (1x1) was observed [37]. However, the width of the HAS diffraction peak was relatively large, which means that the coherence length (i.e., the average size of patches) is rather small. This indicates a rough surface and/or a surface with high density of defect.
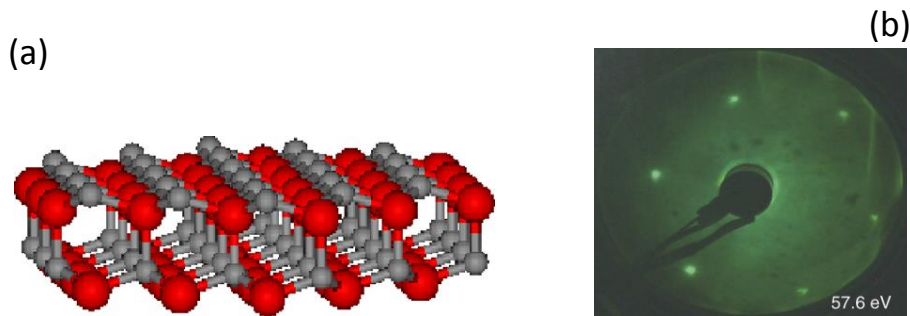
Figure 2-2. (a) Atomic model of the ideal Zn-ZnO(0001), gray: zinc; red: oxygen. (b) LEED pattern of the Zn-ZnO(0001) surface. Reproduced with permission from Wöll [28].

STM characterization showed local surface features [38]. As shown in Figure 2-3a, the surface is full of triangularly shaped pits and islands, which results in a lower extent of long range ordering that rises the background level of the LEED image. From DFT calculation the structural model was concluded, which is shown in Figure 2-3b, c and d. The edges of the triangular terraces consist of oxygen. This changes the overall stoichiometry of the surface: The fraction of Zn ions decreases, which reduces the surface charge. As a result, the dipole created by the unbalanced charge distribution is partially cancelled out. It was concluded that the polarity is the driving force of the observed reconstruction on the Zn-ZnO(0001) surface.
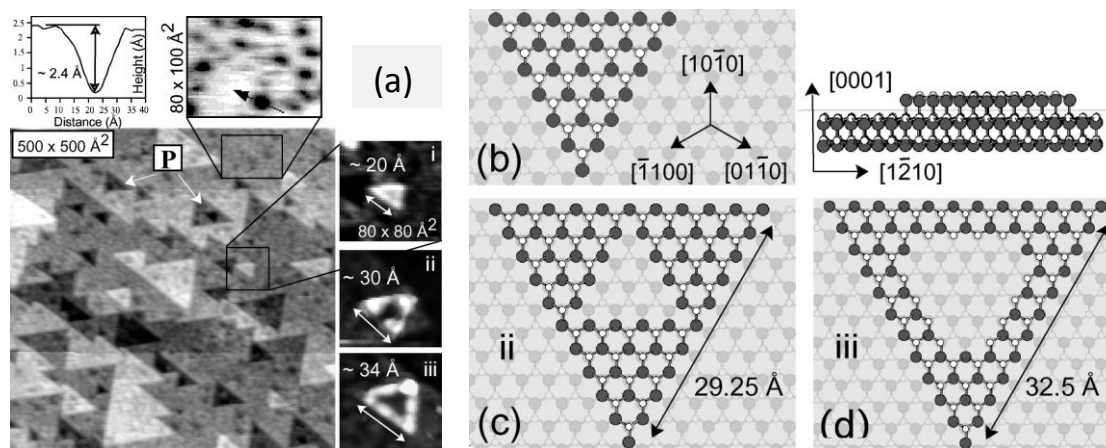
Figure 2-3. Zn-ZnO(0001) surface. (a) STM images; (b-d) DFT stimulated atomic structure. Reproduced with permission from Dulub et al. [38].

In addition to theoretical investigations [39, 40], the interaction of Zn-ZnO(0001) surface with CO was studied by HAS [41]. Upon dosing CO molecules, the specular peak from Zn-ZnO(0001) was strongly reduced, the absence of additional diffraction feature indicated the presence of an ordered (1x1)-adlayer of CO [28, 41]. As a possible cause [41] to the reduction of the specular peak is that, the diffraction peak is strongly attenuated due to the Debye-Waller effect [42, 43].

The thermal stability of hydrogen species on the Zn-ZnO(0001) surface, a system that was prepared by dosing atomic hydrogen onto the surface at 200 K, was studied by temperature programed helium atom reflectivity [37]. Results showed that at 385 K the Zn-H species disappeared; while at 536 K, the surface O-H vanished. The latter was somewhat unexpected, since the surface is initially terminated by zinc. One of the explanations involves a major reconstruction of the surface caused by H atom dosing. This hypothesis would be consistent with the fact that the long-range ordering measured by HAS disappears for prolonged H atom exposure. The ZnH-terminated surface is chemically rather inert, as demonstrated by CO adsorption experiments [39]. No adsorption of CO is observed at temperature above 50 K.

Not only H atoms, but also H_2 molecules modify the surface substaintially [44]. Upon exposing the Zn-ZnO(0001) surface with 10^{-5} mbar H_2 at elevated temperature, the surface is roughened, with the disappearance of the triangular structures. In addition, the surface becomes metalic as shown by tunneling spectroscopy. The Zn-ZnO(0001) surface is very reactive to H_2O. At room temperature, several Langmuirs (1L = 10^{-6} torr•sec) of H_2O dosage induce

severe morphological changes [45], as shown in Figure 2-4. These changes are caused by hydroxylation, as observed by XPS.
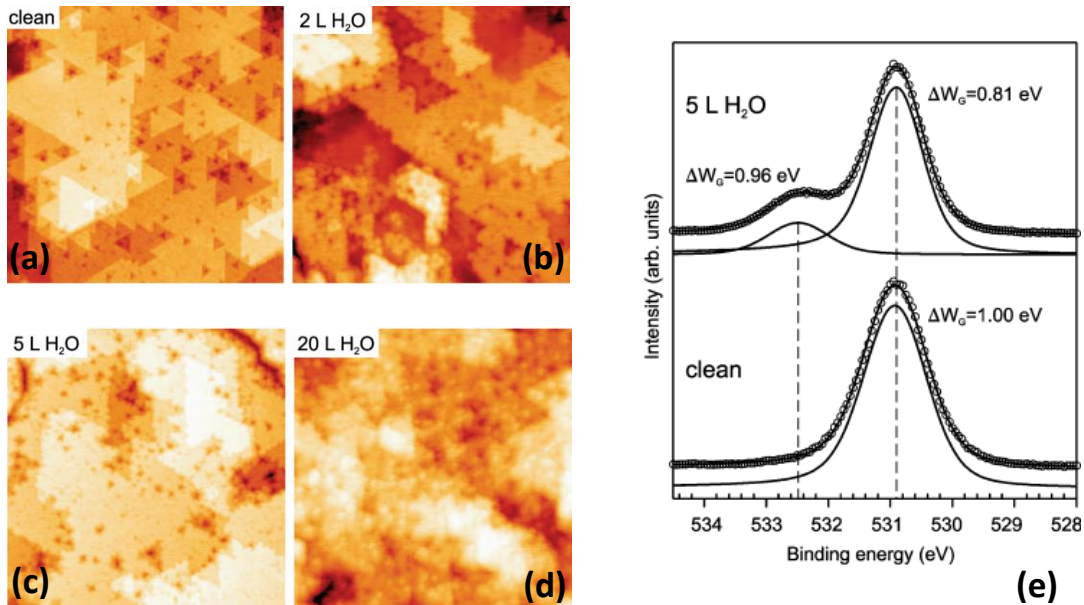
Figure 2-4. H₂O dosing experiments under room temperature on the Zn-ZnO(0001) surface recorded by STM. (a) As prepared surface. (b) Dosed 2 L H₂O. (c) Dosed 5 L H₂O. (d) Dosed 20 L H₂O. Tunnelling conditions: 3.0 V, 0.04 nA. (e) XPS spectra of the Zn-ZnO(0001) surface, before and after dosing 5 L H₂O at room temperature. Reproduced with permission from Onsten et al. [45].

2.2.2 The oxygen-terminated O-ZnO(000$\bar{1}$) surfaces:

The structural model of the ideal, unreconstructed O-ZnO(000$\bar{1}$) surface is illustrated in Figure 2-5. Early studies showed that this surface is stable. Dosing H atom on this surface could not induce any observable change [28]. This is unexpected, since the polar surface need to be stabilized.
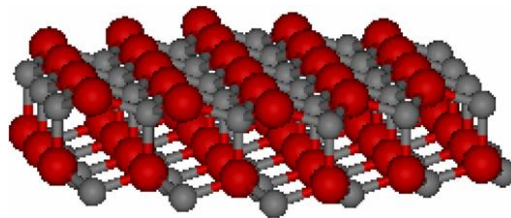
Figure 2-5. Atomic model of the ideal O-ZnO(0001), gray: zinc; red: oxygen. Reproduced with permission from Wöll [28].

It has turned out, however, that a surface prepared in sufficiently good UHV (<1x10^{10} mbar) to prevent reacting with the residual gas [46], showed the LEED pattern of a (1x3) reconstruction, as shown in Figure 2-6a. Based on LEED and HAS results, the corresponding model shown in Figure 2-6b was proposed. Note, however, that this structure is electrostatically unstable, as the surface is terminated by oxygen anions; therefore, there must be another mechanism to stabilize the surface. One possibility is the introduction of steps; another is hydroxylation of the oxygen, either fully or partially. Both possibilities, however, could not be evaluated solely by LEED and HAS experiments.
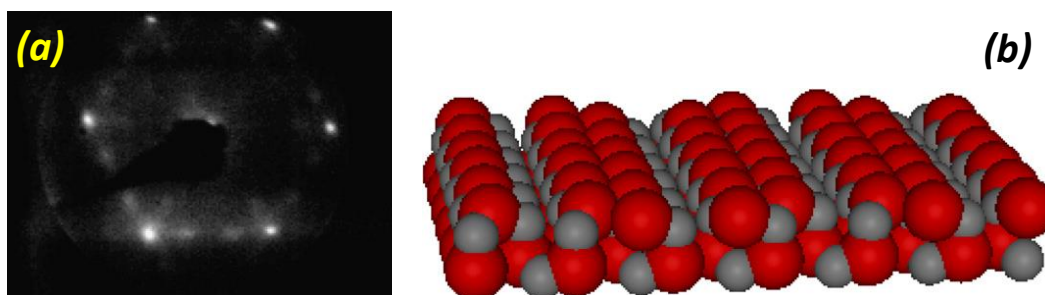
**Figure 2-6. The reconstructed (1x3) O-ZnO(000$\bar{1}$). (a) LEED pattern. (b) Proposed structural model, gray: zinc; red: oxygen. Reproduced with permission from Wöll [28].**

The observation of the (1x3)-ZnO(000$\bar{1}$) surface under particularly clean UHV condition indicates that the (1x1) surface prepared in the earlier studies is actually a surface after reacting with residual gases. Gas dosing experiments on the (1x3)-ZnO(000$\bar{1}$) surface support this hypothesis. Subsequently dosing water or H atoms converted the (1x3) structure into a (1x1) structure, as shown by LEED in Figure 2-7b. CO adsorption experiments were in agreement with the hydroxylation of the O-ZnO(000$\bar{1}$) surface [39, 47]. The formation of OH group on the ZnO(000$\bar{1}$) surface was further confirmed by a HREELS study [48] after dosing water or H atom on (1x3)-ZnO(000$\bar{1}$), as shown in Figure 2-7a. The dose of H$_2$O on the pristine surface resulted in an (OH) band at 3621 cm^{-1}, while the effect of H atoms was small. The proposed OH-ZnO(000$\bar{1}$) is illustrated in Figure 2-7c.
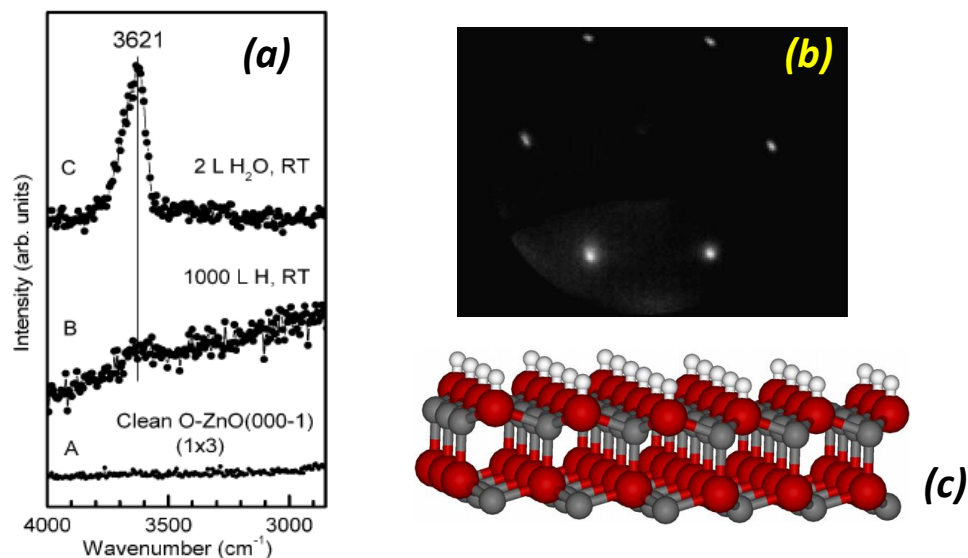
Figure 2-7. (a) The HREEL spectra, of the clean O-ZnO(000$\bar{1}$), and that dosed with 1000 L Hydrogen atom and 2 L H$_2$O, respectively. (b) LEED pattern. (c) Proposed structural model of (1x1)OH-ZnO(000$\bar{1}$), gray: zinc; red: oxygen; white: hydrogen. (a): Reproduced with permission from Noei et al. [48]; (b) and (c): Reproduced with permission from Wöll [28].

A STM study revealed the topography of the O-ZnO(000$\bar{1}$) surface [49]. As shown in Figure 2-8, it is very different to the Zn-ZnO(0001): no small holes, pits and islands. In contrast, hexagonal terraces and predominantly double steps (5.4 Å) are observed.
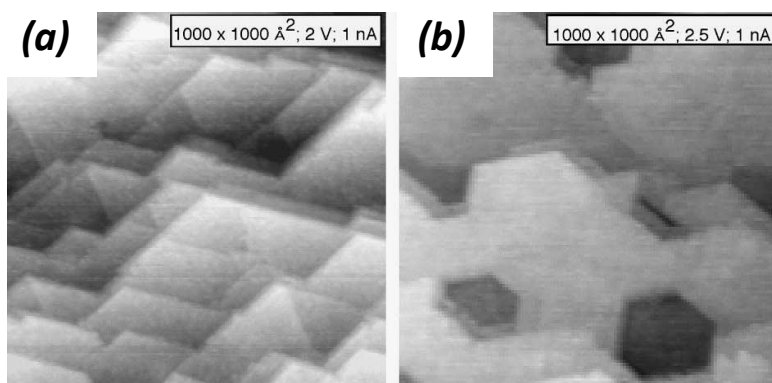
Figure 2-8. STM image of O-ZnO(000$\bar{1}$). Reproduced with permission from Dulub et al. [49].

A more recent study on the O-ZnO(000$\bar{1}$) shows that the half-hydroxylated surface forms a (1x2) structure, as shown in the non-contact atomic force microscope (nc-AFM) image in Figure 2-9a [50]. The source of hydrogen to form OH is not clear. It might come from the H$_2$ or H$_2$O of the residual gas, or from the interstitial H atoms commonly present in the bulk of the

crystal [51]. The hydroxyls disappear from the surface upon heating to 773 K. At 723 K, the surface exhibits a honeycomb reconstruction with a (5x5) periodicity with respect to the O-ZnO(000$\bar{1}$) surface unit lattice.
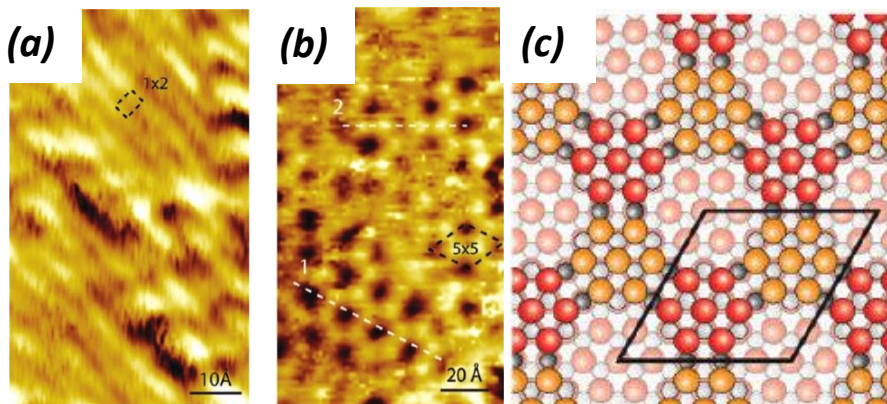
Figure 2-9. (a) nc-AFM image of the (1x2) structure of the 0.5 ML H covered O-ZnO(000$\bar{1}$). (b) STM image of the (5x5) honeycomb reconstruction on the O-ZnO(000$\bar{1}$). (c) The proposed atomic model for the 5x5 honeycomb structure. Reproduced with permission from Lauritsen et al. [50].

Experimentally, it is sometimes not simple to distinguish whether the surface along the [0001] direction is Zn or O terminated. A rather straightforward way to distinguish the Zn-ZnO(0001) and the HO-ZnO(000$\bar{1}$) surfaces is based on dosing pyridine at room temperature, the Zn-ZnO(0001) surface adsorbs the pyridine while the HO-ZnO(000$\bar{1}$) does not [52]. This difference is assigned to the Lewis acid base property. Zn^{2+} exposed on the Zn-ZnO(0001) surface is a Lewis acid: it reacts with pyridine, which possesses an electron lone pair. The difference in pyridine absorption have been applied to determine the surface orientation of sputter-deposited ZnO films on alumina substrates [53].

2.2.3 The mixed-terminated ZnO(10$\bar{1}$0) and ZnO(11$\bar{2}$0) surfaces:

The ZnO(10$\bar{1}$0) terminated surface has attracted considerable interest, since it is the lowest energy single crystal surface of ZnO [54-56]. Its electrostatic stability makes it simpler for theoretical calculations [57, 58], which concluded that the surfaces does not significantly

reconstruct. These studies agree well with earlier LEED studies [59], as shown in Figure 2-10a, and HAS studies [60]. The atomic model is shown in Figure 2-10b.
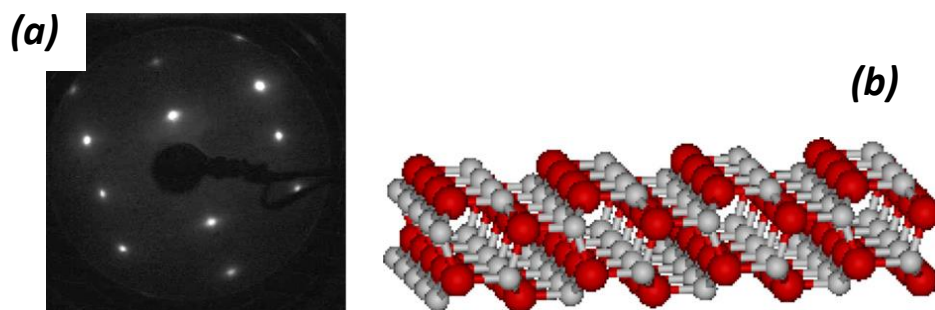
Figure 2-10. (a) LEED pattern of the ZnO($10\bar{1}0$) surface. Incident electron energy 71 eV. Reproduced with permission from Dulub et al. [49] (b) Structure model of ZnO($10\bar{1}0$) surface. Reproduced with permission from Wöll [28].

Several groups were successful in recording STM images of the ZnO($10\bar{1}0$) surface [49, 60-62]. Some examples are shown in Figure 2-11. The protrusions in these images are tentatively assigned to Zn atoms, since both the occupied and unoccupied states, which are closest to the Fermi energy, are mainly of Zn 3d character [63].
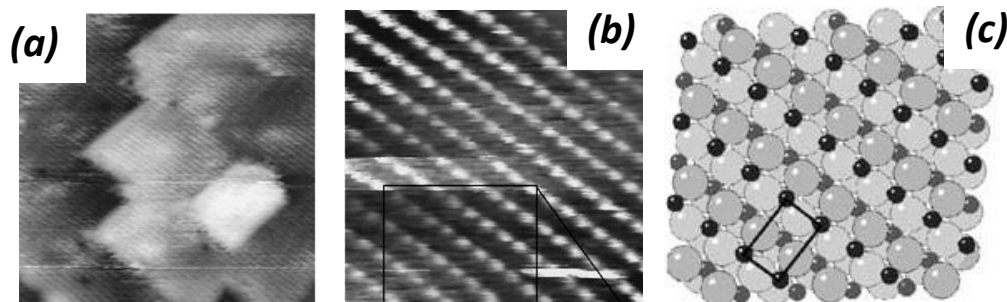
Figure 2-11. The STM image of the ZnO($10\bar{1}0$) surface. (a) STM image, 50 x 50 nm. (b) STM, 5 x 5 nm, -0.9 V, 8.3 nA. (c) The atomic model build from the STM image. Reproduced with permission from Diebold et al. [62].

Water dosing experiments were conducted on this surface. A combination of STM and DFT studies show that some of the water molecules adsorbed at room temperature are dissociated and form a (2x1) structure, while some remain intact, and arranged with a (1x1) periodicity [64]. The (2x1) phase and the (1x1) phases are quasi-reversible, since the (2x1) structure is only 0.1 eV lower in energy comparing to the (1x1) structure; in addition to that, the activation barrier for the H abstraction from the H_2O molecule, which is the energy barrier between the two phases, is as low as 0.05 eV. In fact, the coexistence of the two structures is

observed in STM as shown in Figure 2-12. In addition to the abovementioned two structures, another intermediate (IM) structure appears on the surface. It holds a (2x1) periodicity, yet the contrast in the STM image is much weaker.
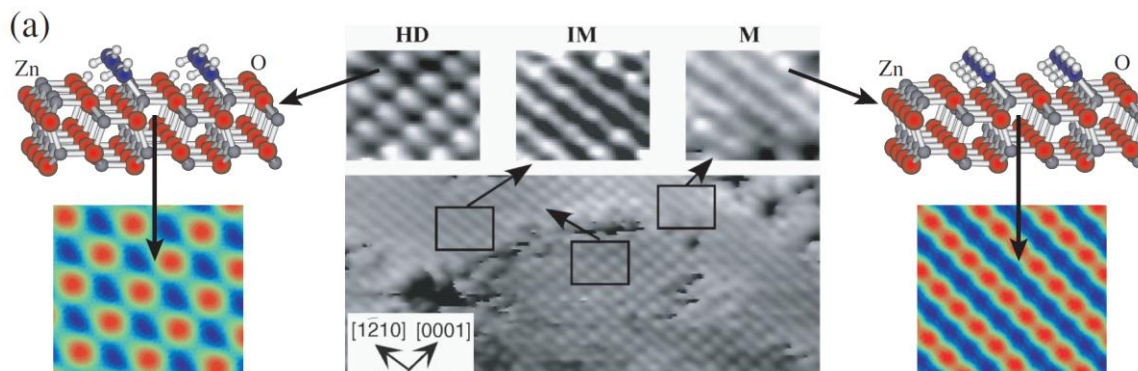
Figure 2-12. The STM images and corresponding structural model of water adsorbed ZnO(10$\overline{1}$0) surface. HD: half dissociated, 1x2 structure; M: molecular monolayer, 1x1 structure; IM: intermediate. Reproduced with permission from Dulub at al [64].

A H atom dosing experiment was also conducted on this surface [60, 61]. It was shown that a well-ordered (1x1) H adlayer is formed. The H atoms adsorbed on top of the oxygen atoms form hydroxyls, as indicated by STM and HREELS data. Tunneling spectroscopy and DFT revealed that the H atom induces metallization of the surface at room temperature. The hydrogen covered surface contains more missing lattice ions than the pristine surface.

Fewer studies on the nonpolar (11$\overline{2}$0) surface were reported [65, 66]. The LEED shown in Figure 2-13a suggests that the surface structure is essentially unreconstructed, same as the truncation of a single crystal as shown in Figure 2-13b. STM studies also suggested the same structure, as shown in Figure 2-14.
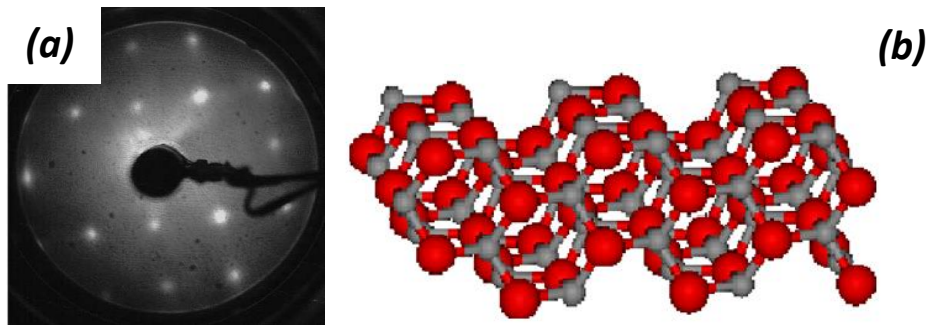
Figure 2-13. (a) LEED pattern of the ZnO(11$\overline{2}$0) surface, Reproduced with permission from Dulub et al.[49] (b) Structure of a bulk-truncated mixed-terminated ZnO(11$\overline{2}$0) surface. Reproduced with permission from Wöll [28].
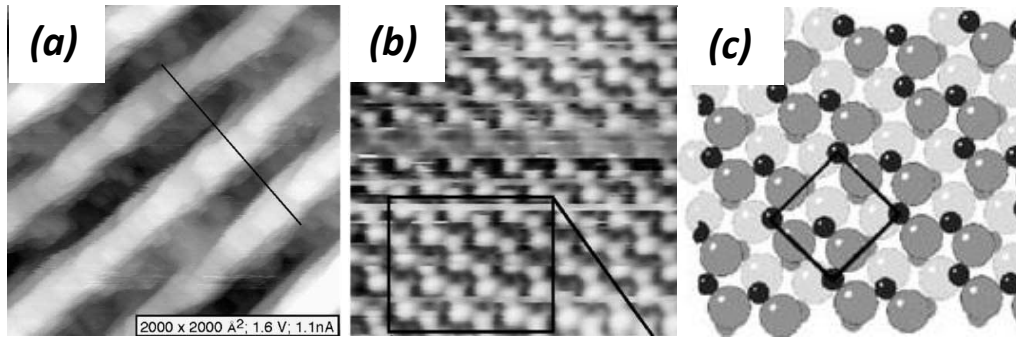
Figure 2-14. STM images of the ZnO(11$\bar{2}$0) surface. (a) 200 x 200 nm. The corrugation height along the black line is 4~7 nm. Tunneling condition: 2.2 V, 1.5 nA; (b) STM image showing the atomic arrangement. Image size: 5 x 5 nm, tunneling condition: 2.9 V, 0.8 nA; (c) The atomic model based on the STM image (b). (a): Reproduced with permission from Dulub et al. [49]; (b) and (c): Reproduced with permission from Diebold et al. [62].

Notably, in the LEED image shown in Figure 2-13a, the diffraction spots are immersed in an intense background [49]. This suggests that the surface contains high density of defect. In Figure 2-14a, the STM image shows big strips with step heights between 4~7 nm. On the other hand, the high resolution image in Figure 2-14b shows that the surface is partially atomically well-ordered. The atomic model of this surface is illustrated in Figure 2-14c.

2.3 Surface polarity and ultrathin films

In an ionic crystal, dipole may accumulate along certain directions. Tasker classified them into three classes [67], as shown in Figure 2-15.
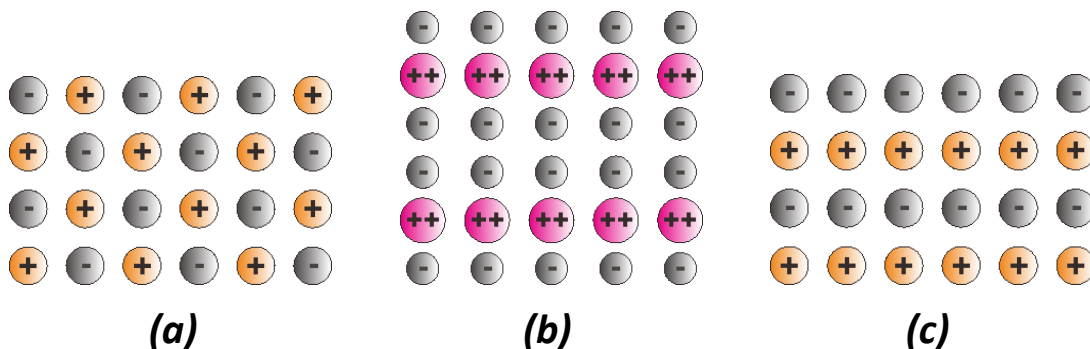
Figure 2-15. Surface of ionic crystal according to Tasker's classification. (a) Type I with equal anions and cations on each plane. (b) Type II with charged planes but no net dipole moment perpendicular to surface. (c) Type III with charged planes and dipole moment normal to surface.

A type-III structure, as shown in Figure 2-15, is unstable because it carries a dipole moment, which is a form of electrostatic potential energy. Surfaces that are created from truncating from type-III structures are therefore not stable. According to the "capacitor" model [68], the system can be seen as a plate capacitor. The total energy stored in the system can be described in the following formula:

$$E = \frac{1}{2}\varepsilon A dV^2,$$

Where ε: permittivity

A: the area of one layer

d: the distance between two layers

V: the electric potential between two layers

Considering that the layer thickness is quantized, the electrostatic energy stored in end layers could be illustrated as in Figure 2-16.

d: distance between adjacent cation and anion layer
D: distance between two repetition units
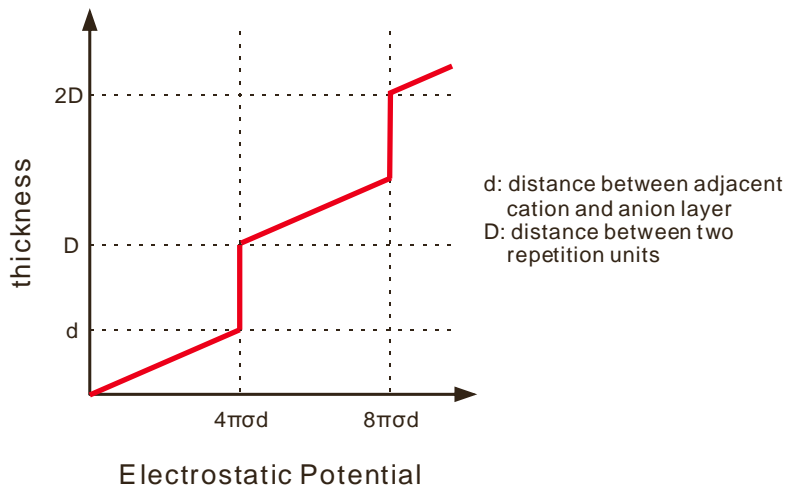
Figure 2-16. Thickness and electrostatic potential dependency of the type-III Tasker's model. Adapt from Nilius [69].

To lower this electrostatic energy, three surface-modifying mechanisms are considered [68, 69]. The first mechanism is a surface reconstruction, which creates planes of fractional occupancy resulting in modified charge distribution. The octapolar reconstruction of the rock-salt(111) surfaces is known best and was observed on NiO(111) [70] and MgO(111) [71] single

crystal surfaces. The second mechanism is the creation of surface states. In this scenario, the atomic surface structure is essentially unchanged. The electrons, however, partially filled in surface states, which metalize the surface. According to DFT studies, α-Al_2O_3(0001) [72] and unreconstructed MgO(111) film [73] adopt this mechanism to heal the polarity. The third mechanism is the binding of adspecies, which become charged upon adsorption. Hydrogen is the most common adspecies. By forming a hydroxyl group, the positively charged H^+ bond to lattice oxygen anions on the surface and partially neutralize the surface negative charges. This mechanism was proven experimentally on MgO(111) [74] and NiO(111) [75].

2.4 Ultrathin zinc oxide films

An earlier attempt of growing well-ordered zinc oxide films on Ag(100), Ag(110) and Ag(111) was reported. The films were characterized by LEED, AES and TPD. The metallic zinc was deposited onto the surfaces, followed by an oxidation in 5×10^{-7} torr oxygen at elevated temperatures. The kinetics of oxidation is different on the three crystal faces, indicating that the process is adsorption mediated. On all three faces the rate of zinc oxidation is markedly reduced over time. This is attributed to the formation of an amorphous zinc oxide passivating layer.

Before the state of the work reported in this thesis, preparation of well-ordered ultrathin zinc oxide film was reported in literature by using Ag(111) [30, 76], Pd(111) [77] as metal substrates. Following the substrate's registry, the films were orientated along the polar axis in the Wurtzite unit cell. Therefore, as in the case of the crystalline surface, the films need a way to cancel the inherent dipole.

On Ag(111), the zinc oxide films were grown by depositing zinc oxide on the substrate in oxygen environment by pulsed laser deposition (PLD), followed by annealing in UHV [30]. The structure was characterized by STM and surface X-ray diffraction (SXRD), as shown in Figure 2-17. The STM image in Figure 2-17a shows a well-ordered extended 2D surface. The surface X-ray diffraction (SXRD) measurements are summarized in the plot shown in Figure 2-17b. It was concluded that the film is bilayer; in addition to that, the distance between the zinc cation and oxygen anion layers is reduced down to one third of that in the bulk unit cell. The structure resembles that of hexagonal boron nitride (h-BN). In this case, the dipole moment of the film is cancelled out by the vertical relaxation of the zinc and oxygen sublayers. This relaxation is

enabled due to flexibility of ultrathin films. This result agrees with a DFT study [29], which concluded that the free-standing ZnO sheet adopts a coplanar structure. The film reverts to a Wurtzite structure as the thickness rises above 4 MLE on Ag(111), as depicted by the SXRD result. The surface morphology also gets roughened as shown in the STM image in the inset of Figure 2-17a.
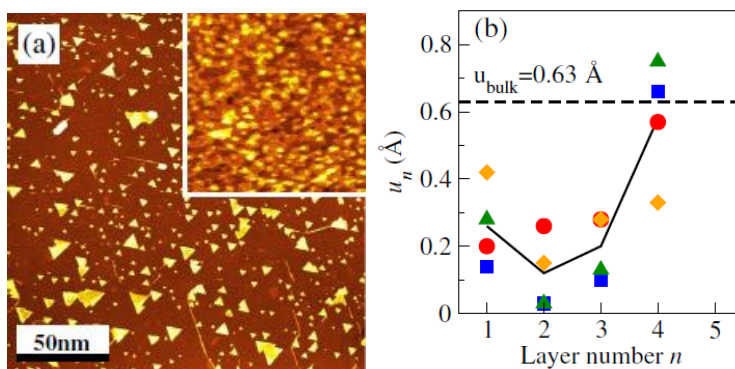
Figure 2-17. The zinc oxide film on Ag(111) support. (a) STM image; (b) The plot summarizing the SXRD result. Reproduced with permission from Tusche et al. [30].

The zinc oxide films on Pd(111) were grown by depositing zinc in oxygen at room temperature, followed by annealing in oxygen at 550 K [77]. The zinc oxide overlayer exhibits a wide range of structures, as shown in Figure 2-18, Figure 2-19 and Figure 2-20. The Figure 2-18 shows the close-packed layer, which has a superstructure consists of a unit cell of a (5x5) zinc oxide unit on a (6x6)-Pd(111) substrate unit. In addition to that, it appears in the form of the honeycomb (4x4)-Pd(111) structure shown in Figure 2-19. Moreover, a close-packed structure with a vacancy per unit cell is shown in Figure 2-20. Based on DFT calculations, the vacancy is assigned to a missing-oxygen. According to DFT calculations, the close-packed structure adopts a h-BN like structure similar to that on Ag(111), and the honeycomb (4x4)-Pd(111) structure is terminated with hydroxyls.
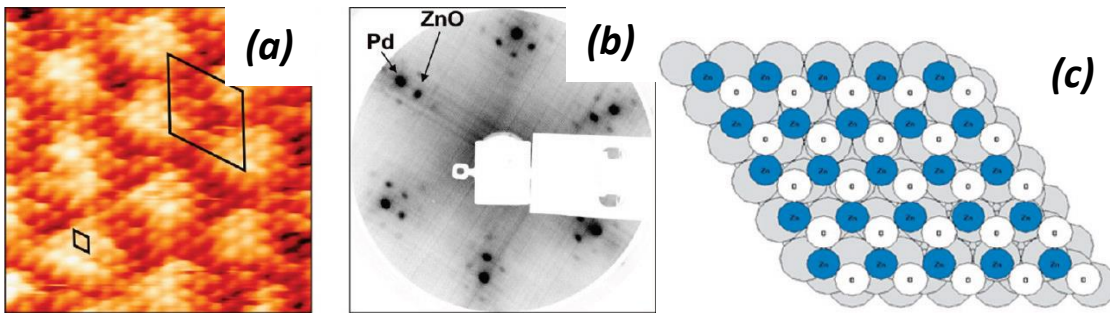
Figure 2-18. The close-packed zinc oxide overlayer on Pd(111) support. (a) The STM image. (b) The LEED pattern. (c) The structural model. Reproduced with permission from Weirum et al. [77].
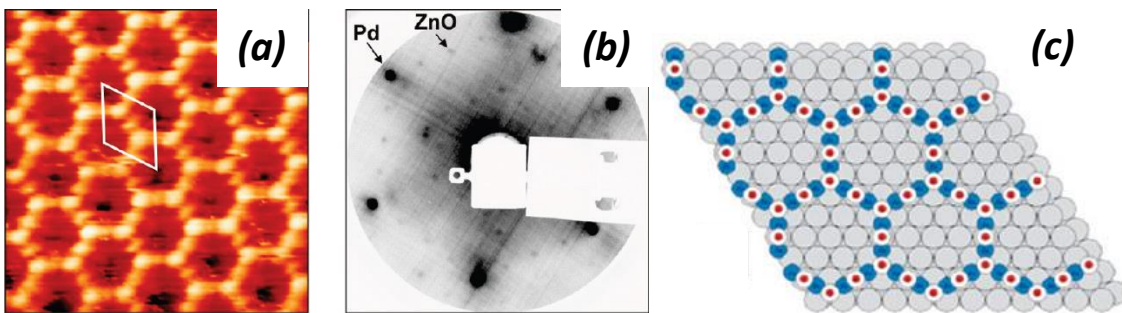
Figure 2-19. The honeycomb-like zinc oxide overlayer on Pd(111) support. (a) The STM image. (b) The LEED pattern. (c) The structural model. Reproduced with permission from Weirum et al. [77].
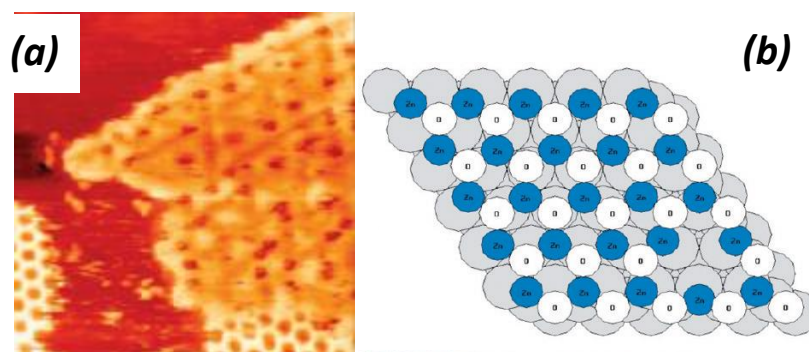
Figure 2-20. The close-packed zinc oxide overlayer with an oxygen vacancy per unit cell on Pd(111) support. (a) The STM image. (b) The structural model. Reproduced with permission from Weirum et al. [77].

Very recently, zinc oxide films were prepared on Fe(001) [78], Au(111) [79, 80], and brass(111) [81]. The film on a Fe(110) [78] support was also studied by SXRD. The result is, however, different from that on Ag(111): It adopts a bulk-like Wurtzite structure. This is ascribed to the anisotropic charge redistribution within the ZnO film induced by the interfacial oxygen.

On Au(111), the ultrathin zinc oxide film exhibits similar STM appearance to that on Ag(111) [80]. To grow the film, zinc metal is deposited in oxygen pressure, followed by annealing at 550 K in vacuum. The stoichiometry of the film is ZnO, as determined by XPS. The authors claimed that, the submonolayer covered film shows a mixture of monolayer and bilayer islands, as shown in Figure 2-21a. All islands converted to bilayer after an hour-long annealing in UHV at 550 K, as shown in Figure 2-21b. DFT studies show that these structures adopt the h-BN like structure, as in the case of Ag(111) and Pd(111).
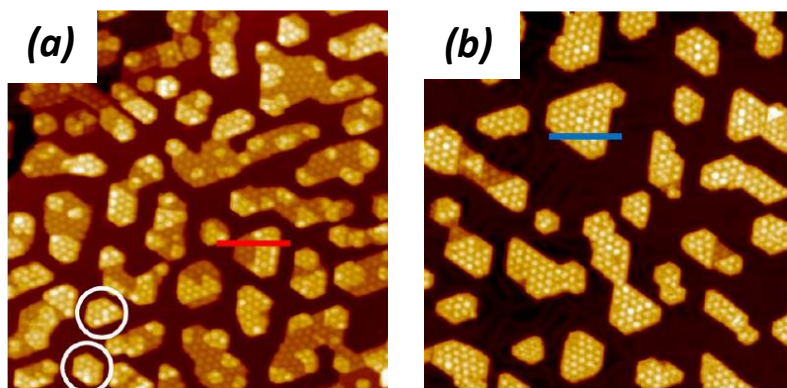
Figure 2-21. 2D zinc oxide islands on Au(111) support. (a) The island consists of two layers. (b) The higher layer grows in expense of the lower layer, resulting from hour-long annealing in 550 K. Reproduced with permission from Deng et al. [80].

On the (111) surface of brass, which consists of 90 % Cu and 10 % Zn, the growth of zinc oxide overlayer was reported [81]. Based on CO and pyridine adsorption experiments characterized by IRAS, the authors concluded that the distance between zinc sublayer and oxygen sublayer is smaller than that deduced from the bulk Wurtzite. Yet, the film is still buckled, which is different from the h-BN-like film grown on Ag(111). The conclusion was supported by DFT calculations, which modeled the zinc oxide overlayer on Cu(111) for simplicity.

Chapter 3 Materials and Methods

3.1 The setups

The experiments reported in this Thesis were carried out in two standard UHV setups. The first setup is a UHV chamber equipped with a scanning tunneling microscope (STM), a 4-grid low energy electron diffraction (LEED) that can be used for Auger electron spectroscopy (AES) experiments. Besides that, it is equipped with a quadruple mass spectrometer (QMS) for temperature programmed desorption (TPD) experiments. A directional gas doser is used to perform adsorption experiments. In addition, the chamber is connected to a "high-pressure" cell, as illustrated in Figure 3-1. It is connected with gas lines, to expose the sample up to 1 bar of selected gases. The inner wall of the cell is coated with gold for passivation. A halogen lamp, installed outside of the high-pressure cell, heats the sample through a quartz window. The sample position can be adjusted along the focal axis. The second UHV setup is equipped with a STM, LEED, an infrared reflection-absorption spectroscopy (IRAS) and X-ray photoelectron spectroscopy (XPS).

Halogen lamp

Quartz window

Copper pipe surrounding the wall to water-cool the compartment
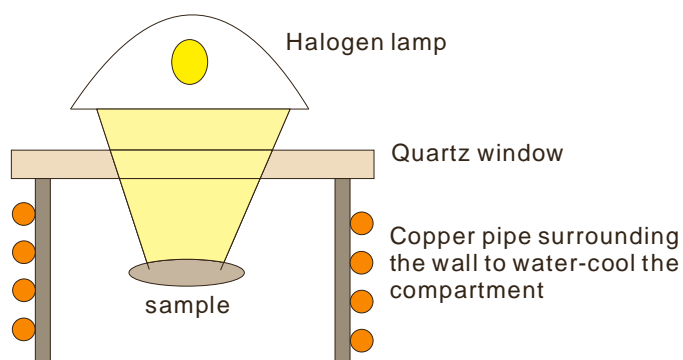
sample

Figure 3-1. The high pressure cell for exposing samples to a higher pressure and temperature.

Zinc evaporation is performed in a separated cell, connected to the main chamber via a gate valve. This is to prevent the possible contamination due to the high vapor pressure of zinc metal. Figure 3-2 shows the homemade zinc evaporator. A zinc rod of Ø 1.0 mm is wrapped with Ø 0.2mm tungsten wire. A K-type thermocouple (chromel – alumel) is spot welded to the zinc rod. The thermocouple wires are connected to a feedback unit to precisely control the temperature, and hence the zinc flux. The temperature read-out is connected to a feedback circuit, which controls the power supply that powers the tungsten wire heating the zinc rod

resistively. As shown in Figure 3-2b, the evaporator is covered with a shield made of tantalum foil with an Ø 5 mm orifice at the top.
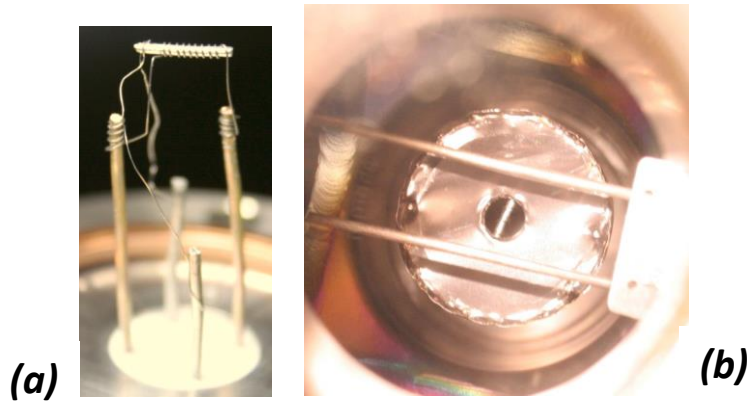
Figure 3-2. (a) The zinc evaporator. (b) The zinc evaporator covered with a metal shield.

3.2 Experimental techniques

3.2.1 Scanning tunneling microscopy (STM)

Scanning tunneling microscopy was invented in 1982 by Binnig and Rohrer [82, 83], who were awarded the Nobel prize in physics in 1986. It has been developed into an important tool in surface science [84].

Before the invention of STM, scattering and diffraction were common tools to characterize surface structures. It can be performed using atoms [85], electron [86] or x-ray photon [87]. On the other hand, the surface electronic properties can be probed by photon with a wavelength from x-ray to visible light [88], or by electron with the technique called electron energy loss spectroscopy [89]. All these methods are spatially averaging techniques; the local properties are buried in the average. STM is complementary to the above mentioned techniques. It obtains structural information in real space on a micrometer scale as well as on an atomic scale. The structure it investigates is not limited to long range ordering, rather local features such as defects and low-coordinated atoms, could be explored. In many cases, these features have a large impact on the properties of oxide materials [90].

The principle of STM is based on the tunnel effect. Tunneling phenomenon was already exploited in (MIM) junctions decades before the invention of STM. The most well-accepted

model to understand a MIM junction is Bardeen's model [91]. Using Fermi's golden rule, the elastic tunneling current of a MIM junction is calculated based on the overlap of the wave functions in the two electrodes. In case of a tip-sample junction, the tunneling current is expressed as:

$$I = \frac{4\pi e}{\hbar} \int\limits_{-\infty}^{+\infty} [f(E_F - eV + E) - f(E_F + E)]\rho_T(E_F - eV + E)\rho_S(E_F + E)|M_{TS}|^2 dE$$

$$f(E): the\ Fermi - Dirac\ distribution$$

$$\rho_T(E): local\ density\ of\ state\ of\ the\ tip$$

$$\rho_S(E): local\ density\ of\ state\ of\ the\ sample$$

Where M_{TS} is the tunneling matrix, which is defined as

$$M_{TS} = \frac{\hbar}{2m}\int_S (\Psi_T^* \nabla \Psi_S - \Psi_S \nabla \Psi_T^*)dS$$

S: an arbitrary surface in the junction between the tip and the sample that covers the region of significant overlap of the wave functions.

The tunneling process can be visualized by the illustration in Figure 3-3.
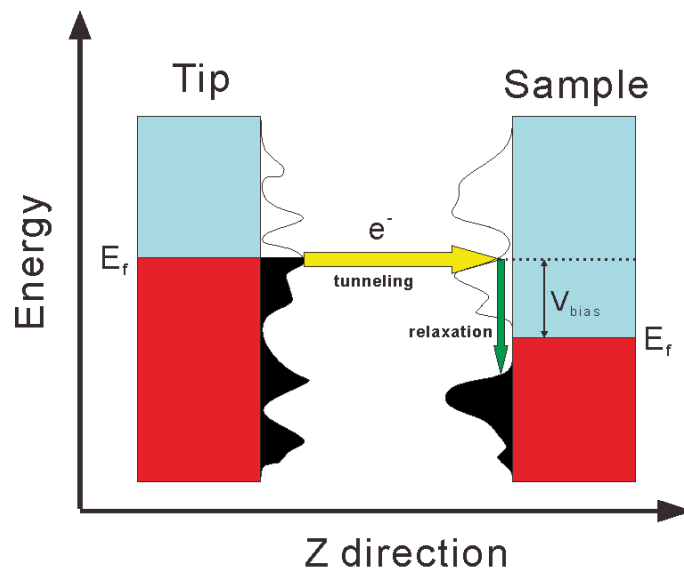
Figure 3-3. Illustration of tunneling process.

To obtain accurate values of the M_{TS}, a good description of tip and sample wave functions is a requisite. However, due to the lack of knowledge of the tip apex structure, modeling of STM image is difficult using this approach. To circumvent this problem, Tersoff and Hamann modeled the tip as a spherical potential well [92, 93]. It is assumed that the resulting eigenfunction is an s-like wave function at the center of the tip apex curvature. With this assumption, the shape of the tip does not affect the tunneling current. When the bias is low, the tunneling current is proportional to the LDOS at the Fermi level (E_F) of the sample, at the position where the tip curvature center is located. This conclusion can be express as:

$$I \propto V_{bias} \bullet \rho_S(r_0, E_F)$$

$$r_0: position\ of\ the\ center\ of\ tip\ curvature$$

$$V_{bias}: electric\ potential\ between\ tip\ and\ sample$$

This simplification provides an easy way to interpret STM images, which represent the potential energy surface at the energy level that is V_{bias} different from the surface Fermi level.

Despite its successful application in many cases, the Tersoff and Hamann's model fails in predicting the high corrugation amplitude in STM images of close packed metal surfaces. Chen ascribes this issue to the simplificative assumption of s-like tip wave function [94]. Using localized tip orbitals, such as a d orbital, which orient towards the sample, the description is improved. With this approach, experimental results can be reproduced, by choosing an appropriate tip orbital and generate a suitable model.

An alternative approach to model tunneling process in the junctions is to apply the WKB (Wentzel-Kramers-Brillouin) semiclassical approximation. In this approach, the tunneling current is expressed by transmission probability T(E, eV, D) between two electrodes at temperature close to 0 K and bias voltage lower than the work function of both electrodes [95]. The process is expressed as follow:

$$I \propto \int_{-\infty}^{+\infty} \rho_T(r, E_F - eV + E) \bullet \rho_S(r, E_F + E) \bullet T(E, eV, D) \bullet dE$$

$$Where\ \ T(E, eV, D) = exp\left(-\frac{2D\sqrt{2m}}{\hbar} \bullet \sqrt{\frac{\Phi_S + \Phi_T}{2} + \frac{eV}{2} - E}\right)$$

D: tunneling distance

Φ_s, Φ_T: work function of the sample and tip, respectively

Since the tunneling probability decays exponentially with respect to the tip-sample distance, the tunneling current is very sensitive to the tip-sample distance. This makes STM an effective tool to investigate topography of a surface. In the constant current mode, the tunneling current is kept constant. The tip's vertical position, which is read out by an external circuit, represents the contour of local density of state of selected energy level. An alternative way is the constant height mode, in which the vertical position of the tip is fixed during measurements. This mode can only be applied on atomically flat surfaces, in return for a significantly higher scan rate. Noteworthily, the topographical information obtained from the STM is always convoluted with the electronic structure. This should be taken into account when interpreting data.

Besides imaging the topology of a surface, this setup can measure local electronic features by measuring the I-V dependency, an experiment referred to as scanning tunneling spectroscopy [96] (STS). The derivative of the tunneling current over the voltage, dI/dV, represents the density of state of a local feature.

The core of the apparatus is illustrated in Figure 3-4. It consists of an atomically sharp tip, which acts as an electrode and is brought very close to a conductive surface, such that the electrons can tunnel through the vacuum barrier upon applying a potential, typically within ±10 V. The electric field in the vacuum is up to hundreds of V/μm. The tip is usually made of tungsten or platinum-iridium alloy. It is prepared from a cut wire, which is then etched electrochemically [97]. To obtain a better spatial resolution, the tip should be treated in-situ by, for example, applying high voltage pulses, or by gently touching the surface. These tip treating procedures are more like an art than a science; it varies among different experiment performer. All STM experiments are conducted using a vibration isolation system, for the sake of isolating the experiment from environmental vibrations.
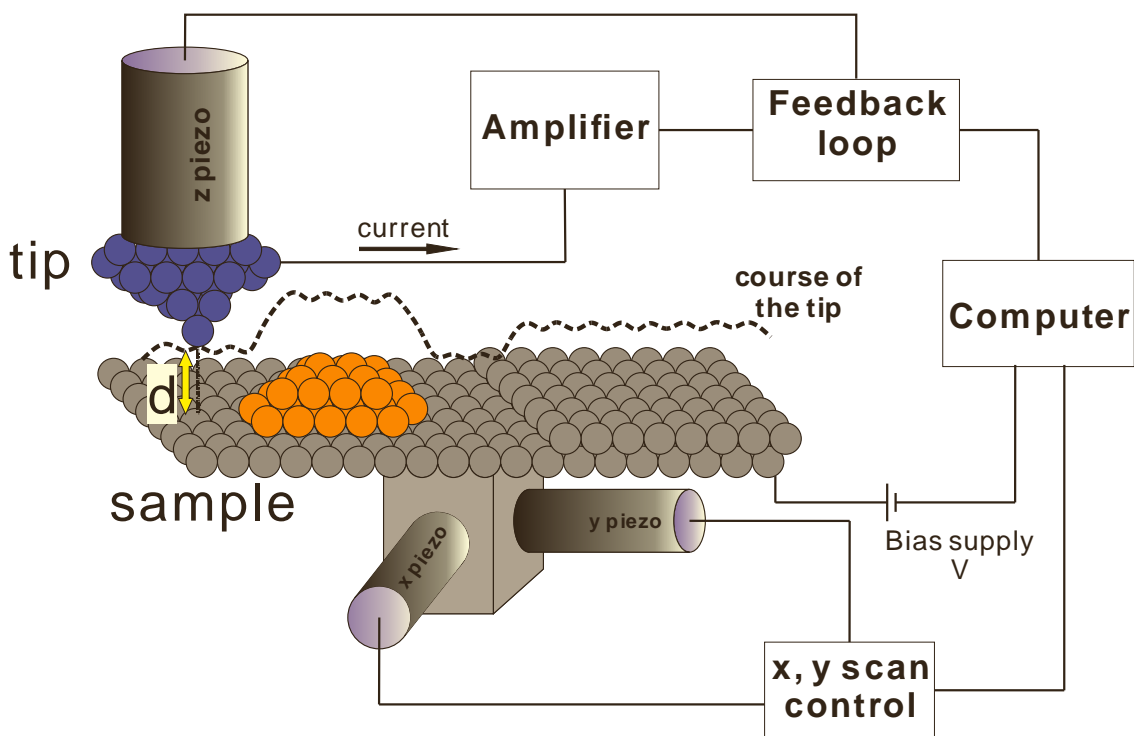
Figure 3-4. Schematic representation of an STM setup

The application of STM goes beyond measuring electronic structure of surfaces. In the techniques called inelastic electron tunneling spectroscopy (IETS) [98, 99], the vibrational modes of surface adsorbate can be probed. This is based on the so-called inelastic tunneling process [100]. In this tunneling process, energy is exchanged between the tip and local surface states of the sample. Energy losses of tunneling electrons can excite, for example, vibrational modes of individual adsorbed molecules. The inelastic tunneling channel results in an increase of the total conductance, as elastic and inelastic transport contributions add up. Since changes in the differential conductance are tiny, the second derivative of the tunnel current (d^2I/dV^2) is usually measured instead of the dI/dV signal.

In addition to the abovementioned techniques, STM can also be used to measure optical properties by Photon emission STM (PSTM) [101] and magnetic properties by spin-polarized STM [102, 103] (SP-STM). Recently, Raman spectra of single molecules on surface were recorded by Tip-Enhanced Raman Spectroscopy [104, 105] (TERS), which combines a laser source with an

STM. All these developments enable the physical and chemical properties of local surface features be investigated in various aspects.

3.2.2 Infrared reflection-absorption spectroscopy (IRAS)

Infrared photons are effective probes for exploring molecular structure [106, 107], since their energy overlap with the energy of molecular vibrations. In a molecule, all atoms oscillate in coordinated ways, called normal modes. The more atoms a molecule contains, the more normal mode it has. For a nonlinear molecule, the number of normal mode is 3N-6, where N is the number of atoms; for a linear molecule, the number of normal mode is equal to 3N-5. Examples are given in the Figure 3-5 and Figure 3-6.
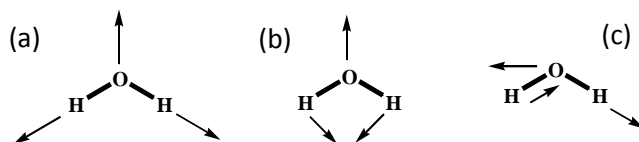
Figure 3-5. Vibrational modes of water molecules. (a) Symmetric stretch. (b) Bending. (c) Asymmetric stretch
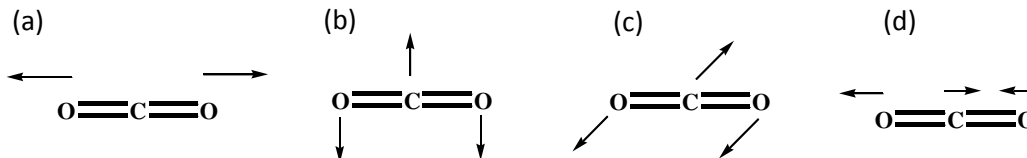
Figure 3-6. Vibrational modes of carbon dioxide molecule. (a) Symmetric stretch. (b, c) Bend. (d) Asymmetry stretch

Not all normal modes appear in infrared spectra. A normal mode only absorbs the incident infrared photon when its frequency matches that of the photon; in addition, it should induce a dipole moment change of the molecule. Take carbon dioxide as an example, the asymmetric stretch mode and the bending modes change the dipole moment of the molecule. These modes resonant with incident infrared photon, and are called infrared active. On the contrary, the symmetry stretching mode doesn't induce a net dipole moment change in the molecule, therefore is infrared inactive.

Infrared spectra of species on conductive surfaces obey an additional restriction, called "metal selection" rule [108]: Only the dipole moment changes perpendicular to the metal surface can be detected. As illustrated in Figure 3-7, when a dipolar molecule is adsorbed on a

metal surface, an image dipole is induced. The perpendicular component of the molecular dipole moment induces an image dipole moment that has the same orientation. The two dipole moments add up, resulting in a larger total dipole moment. On the contrary, the parallel component of the molecular dipole moment is cancelled by the induced dipole moment. As a consequence, only the molecular vibrational modes that give rise to a change of dipole moment that is perpendicular to the surface can be observed in infrared spectroscopy.
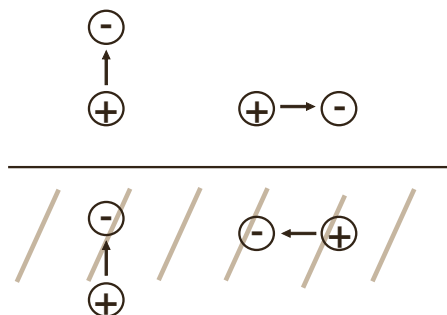
Figure 3-7. Dipole selection rule on metal surfaces. The dipole perpendicular to the surface is reinforced by the surface image dipole; that parallel to the surface is cancelled.

To conduct infrared absorption spectroscopic experiments on a surface, a reflective geometry is often applied [109-112]. Accordingly, the method is named as infrared reflection absorption spectroscopy (IRAS). According to the work of Francis and Ellison [113], reflection of infrared light from a clean metal surface can be described by using Fresnel's equation. The refraction index of the metal is expressed as: $\tilde{n} = n + ik$. As shown in Figure 3-8, assuming that $n^2 + k^2 \gg 1$, which is valid in the infrared region, the intensity of reflected light from a clean metal surface with an angle ɸ can be expressed as:

$$R_s = \left.\left(n - sec\ \Phi\right)^2 + k^2 \middle/ (n + sec\ \Phi)^2 + k^2\right.$$

$$R_p = \left.(n - cos\ \Phi)^2 + k^2 \middle/ (n + cos\ \Phi)^2 + k^2\right.$$

Where s and p are denoted the perpendicular and parallel component of the light with respect to the plane of the incident light, respectively.
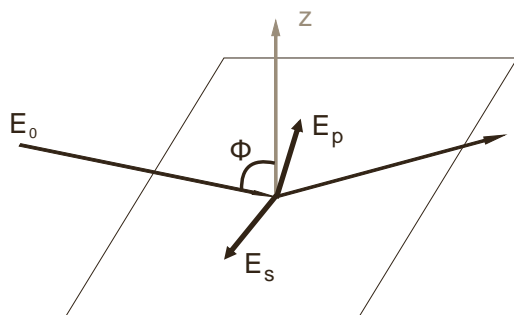
Upon reflection, the phase of the incident irradiation changes. The Phase of the s-component is inverted at all incident angles; in other words, it has a phase shift of π. The physical picture of this can be understood by illustration in Figure 3-7, in which the dipole caused by an electric field that is parallel to the surface induces an image dipole which has an opposite phase. This image dipole emits electric field, which is the reflective light, with a phase shift of π. As a consequence, the s-component gives a vanishing electric field at the surface due to destructive interference. This is an additional reason for the validity of a selection rule for the dipole excitation of vibrational modes by infrared light on metal surfaces: There is no electric field that is parallel to the surface to excite vibrational modes parallel to the surface. On the other hand, the phase shift of one p-component is strongly dependent on the angle of incident. As can be shown in the following formula:

$$tan\left(d_p - d_s\right) = \frac{2 * k * tan\phi * sin\phi}{tan^2\phi - (n^2 - k^2)}$$

Where d_s is the phase shift of the s-component, which can be taken as π, and d_p is the phase shift of the p-component. In Figure 3-9a, d_p is evaluated, and plotted with respect to φ. At grazing incidence, a large resultant field E_p is established. As an example, the angular dependency of E_p and E_p/E_0 on a copper surface with incident photon frequency 2000 cm^{-1} is shown in Figure 3-9b. Note that the angle of maximum reflectivity depends on sample and wavelength of incident photon. For the current example, the maximum of E_p/E_0 is at around 80°.
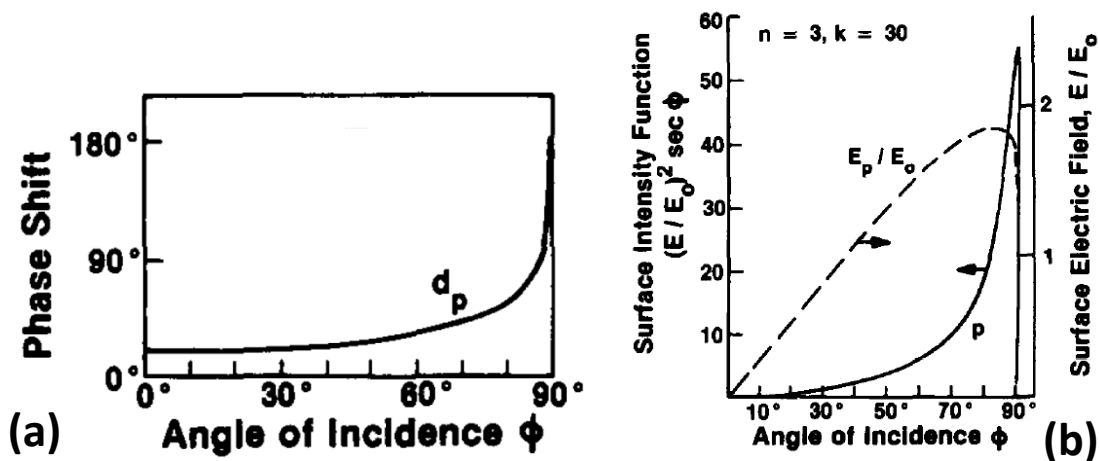
Figure 3-9. Reflection of IR light at a clean metal surface. (a) Phase shifts d_s and d_p with respect to angle of incidence ϕ. (b) Electric field and intensity of p-light versus angle of incidence ϕ. Reproduced and adapted with permission from Hoffmann [112].

Modern infrared absorption spectrometers are usually coupled with a Fourier transform (FT) spectrometer, as illustrated in Figure 3-10. It consists of a light source, a detector and an interferometer. Compared to traditional scanning (dispersive) spectrometer, the main advantage of a Fourier transform spectrometer is a shorter measurement time with a better signal to noise ratio.
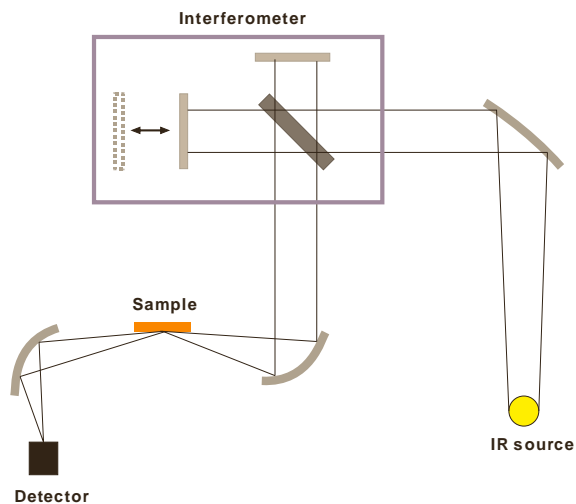
Figure 3-10. Illustration of infrared reflection absorption spectroscopy (IRAS), the FT-IR setup for detecting surface absorption.

The light source used in the FT spectroscopy should be broad band. The light source of the Infrared spectrometer used in this study is a Globar. It is a silicon carbide rod of 5 to 10 mm

diameter and 20 to 50 mm length which is electrically heated up to 1000 to 1650 ^{O}C. It is a common mid-IR photon source of infrared spectrometer.

Modern infrared spectrometers replace the traditional monochromator with an interferometer. The configuration is illustrated in Figure 3-11. It consists of a beam splitter and two mirrors. The beam splitter splits the source light into two arms. One of the two mirrors is fixed and the other is moving back and forth during measurement along the path of the incident beam. The two beams reflected from the two mirrors interfere with each other. This is due to the path length difference of two beams. As the position of the movable mirror changes, the travelling distance of the according light varies. Frequency composition of the light that shines on the sample varies with respect to the mirror position. As a result, the sample is irradiated by light with an oscillating frequency composition. A so-called single channel spectrum, which shows the absorption peaks at each wavelength as well as the spectrometer function, is obtained by Fourier transformation of the recorded signal.
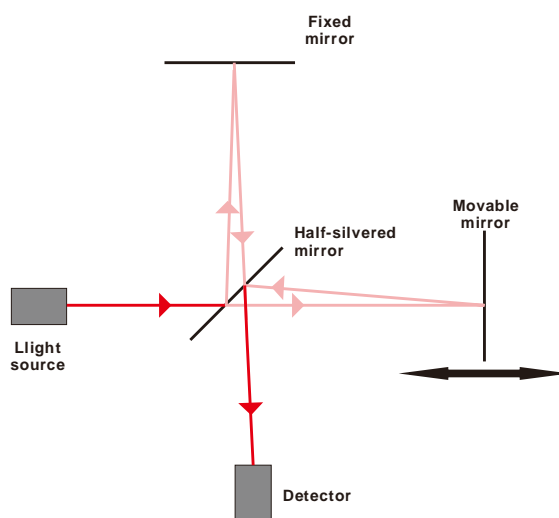
Figure 3-11. The Michelson interferometer.

Since the measurement of absorption change is around 0.1%, the choice of the detector is crucial. The detector used in this study is the mercury cadmium telluride (MCT) detector, a photoconductive detector. Compared to the traditional deuterated L-alanine doped triglycine sulfate (DLaTGS) detector, it has a higher sensitivity and allows for a higher scan speed. To reduce thermal noise, it needs to be cooled to liquid nitrogen temperature during operation.

3.2.3 Low energy electron diffraction (LEED)

Low energy electron diffraction (LEED) [114] is a surface science tool that can be used to determine two dimensional periodic structures. The LEED method was first established by Davisson and Germer in 1927 [115, 116], as a nice demonstration of the wave particle dualism of electrons, proposed by de Broglie. It became a widely adopted technique since the 1960's. In the experiment, a monochromatic low energy electron beam (20-200 eV) is focused onto the surface. The elastically back-scattered electrons produce a diffraction pattern that is visualized by a fluorescent screen. The electrons of this energy range have a de Broglie wavelength of around 1 Å, which makes them suitable to probe interatomic distances. In solid materials, the mean free path of the electron of this energy is low, as shown in Figure 3-12. This ensures that the scattered electrons originate exclusively from the surface. This results in a high surface sensitivity of the LEED technique. The data interpretation is relatively straight forward, as compared to high energy electron diffraction (RHEED) [117], which operates at 10-30 keV electron in grazing incident geometry.
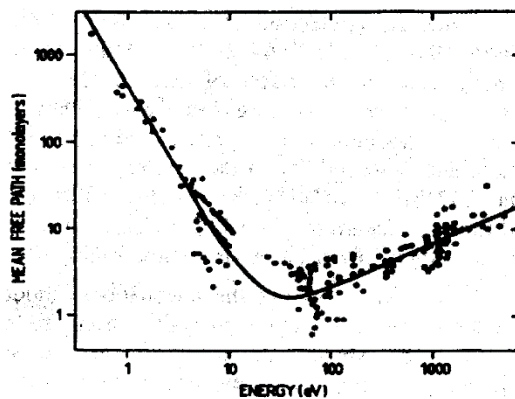
Figure 3-12. Mean free paths of electron in solids as a function of their energy. Reproduced with permission from Lüth [118].

Electrons scattered from a periodic crystal lattice are diffracted due to wave nature of electrons. The diffraction phenomenon can be described by a two-dimensional version of Laue formalism, as describe in the following. If S and S_0 denote the unit vectors for the directions of the scattered and incident beams, respectively, then the interference conditions on a two-dimensional lattice can be described by the so-called Laue equation:

$$\begin{cases} \boldsymbol{a_1}(\mathbf{s} - \mathbf{s_0}) = h\lambda \\ \boldsymbol{a_2}(\mathbf{s} - \mathbf{s_0}) = k\lambda \end{cases}$$

$\mathbf{s_0}$: unit vector for the direction of the incident beam

$\mathbf{s}$: unit vector for the direction of the scattered beam

$\boldsymbol{a_1}$: lattice unit vector in h-direction

$\boldsymbol{a_2}$: lattice unit vector in k-direction

λ: wavelength of incident and scattered electron

Solving the above equations simultaneously gives:

$$\frac{\mathbf{s} - \mathbf{s_0}}{\lambda} = h\boldsymbol{a_1^*} + k\boldsymbol{a_2^*} = \boldsymbol{g},$$

$\boldsymbol{a_1^*}, \boldsymbol{a_2^*}$: the unit mesh vectors of the reciprocal lattice

$\boldsymbol{g}$: the translation vector of the reciprocal lattice

The $\boldsymbol{a_1^*}$ is always perpendicular to $\boldsymbol{a_2}$ with the length $|\boldsymbol{a_1^*}| = \frac{1}{|a_1|\sin\alpha}$, where α denotes the angle between the real space lattice vector $\boldsymbol{a_1}$ and $\boldsymbol{a_2}$; likewise, $\boldsymbol{a_2^*}$ is always perpendicular to $\boldsymbol{a_1}$ and with the length $|\boldsymbol{a_2^*}| = \frac{1}{|a_2|\sin\alpha}$.

These relations can be used to construct the reciprocal lattice from a real space lattice and vice versa. As an example, Figure 3-13 demonstrates the transformation of the real space lattice vectors to the reciprocal space lattice vectors of a fcc(111) surface.
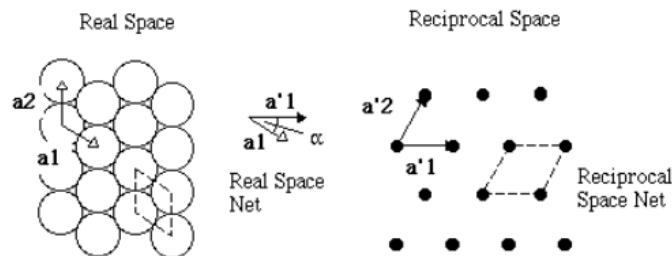
Figure 3-13. An example of surface lattice vector transformation: fcc(111). Reproduced with permission from Garrett [119].

The setup of a typical LEED apparatus is illustrated in Figure 3-14. Electrons are emitted from a filament, with a negative potential of 10-600 V with respect to the sample. The electron beam is focused down to 0.1 - 0.5 mm in width by a series of lenses starting with an electron lens called Wehnelt cylinder. The electron reflected from the surface is collected by a fluorescent screen, whose electric potential is floated up to 3-7 kV to energize the electron, such that it is strong enough to excite the fluorescent screen. Before reaching the screen, the electron goes through four electrodes. The two in the middle are suppressors, whose potential is kept slightly lower than the primary electron in order to cut-off the inelastically scattered electrons that carry no structural information; on the other hand, the two grids placed outside are grounded. The diffraction pattern displayed on the fluorescent screen is recorded by a camera, which is installed outside of the UHV chamber.
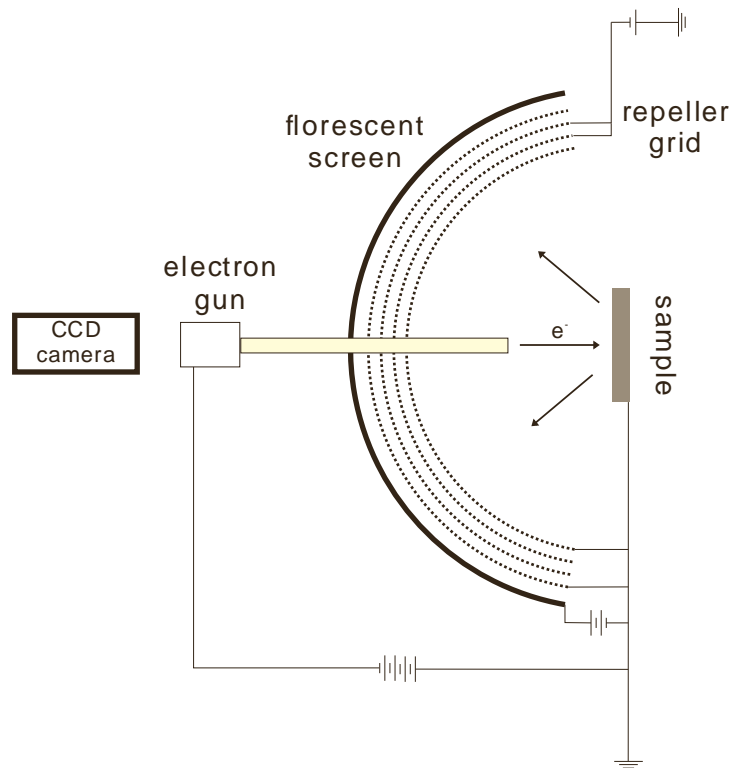
Figure 3-14. A typical LEED set-up.

3.2.4 Auger electron spectroscopy (AES)

Auger electron spectroscopy [120], which is based on the so-called Auger process, is used to determine the chemical compositions of a surface. The name came after Pierre Auger, who discovered this process in 1925 [121].

The Auger process is one of two relaxation processes of an electron hole created by a photoionization process. If a solid is irradiated, e.g. with a beam of electrons of medium or higher energy (1 keV - 10 keV), outer and inner electronic shells of the atoms become ionized. The relaxation can occur in two different ways, as illustrated in Figure 3-15. The first pathway results in x-ray emission. In this process, the core hole is filled by an electron with higher energy of the same atom, and the excess energy is emitted as electromagnetic radiation, which is usually in the x-ray range. The second pathway causes the emission of electrons, which are referred to as Auger electrons. In this process, the core hole is filled by an outer electron, but the energy is, in a radiationless manner, transferred to a second electron of the atom which is ejected from the atom with a characteristic kinetic energy E_{kin}.

$$E_{kin} = E_1 - E_2 - E_3$$

E_1: the binding energy of the initial core electron prior to ionization

E_2: the binding energy of the electron that fills the core hole

E_3: the binding energy of the ejected electron
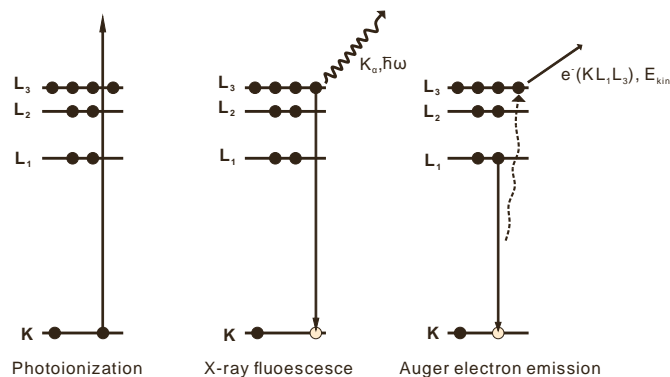
Figure 3-15. Photoelectric process and the following de-excitation mechanisms. Adapted from Garin [122].

The fact that the energy of the core levels that determine the kinetic energy of Auger electrons are element specific, makes this spectroscopy an useful tool for surface-chemical

composition analysis. In addition, the peak intensity shows abundance of the element in the sample.

The excitation probability of the Auger electron could be described phenomenologically by a parameter called Auger yield, which reads $Y_A = \frac{1}{1+\beta Z^4}$, where Z is the atomic number, and β comes from fitting of experimental data. The rest of the holes are quenched by fluorescent emission processes, with the so-called x-ray emission yield: $Y_x = \frac{\beta Z^4}{1+\beta Z^4}$. The two yields are in competition, as shown in Figure 3-16. As can be seen in the plot, for the elements up to Z=20, 90% of the energy relax through the Auger process. This enables the Auger electron to be used as an effective probe to monitor non-metallic impurities, such as carbon or sulfur.
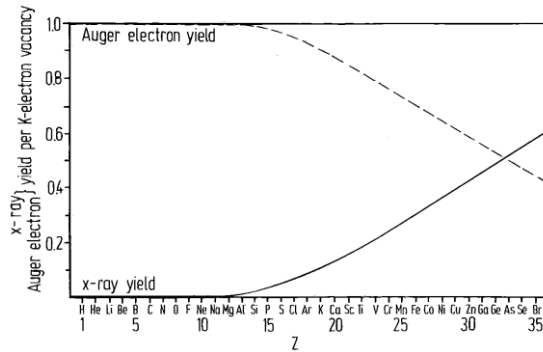
Figure 3-16. Competition between Auger electron and x-ray yields per K-shell vacancy with respect to atomic number. Reproduced with permission from Siegbahn [123].

Another important factor that affects the Auger emission cross section is the primary energy of the incident electron beam. It was shown theoretically [124] that this cross section increases rapidly with incident electron energy, until it reaches three times of the core level energy. Above this threshold energy the cross section increases only marginally with the incident beam energy. Because most of the analytically relevant Auger lines appear between 50 eV and 1 keV, the energy of the incident electron beam for most setups is between 3 keV and 5 keV. According to Figure 3-12, electrons of such kinetic energy can penetrate down to about 1-3 μm under the surface; however, only the Auger electrons that emitted from approximately the top 5 Å, or three atomic layers, are visible in the final spectra.

The setup for AES used in this work is same as that used for LEED experiments, as described in section 2.2.3, and illustrated in Figure 3-14. The 4-grid LEED optic is called a

retarding field analyzer, when the electrodes are applied to a different set of voltage to serve as an electron energy analyzer to Auger electrons. The fluorescent screen for signal readout is operated as an electrode that collects the current information and discarded the spatial information. To enhance the signal to noise ratio, a lock-in amplifier is integrated in the instrument.

3.3 Growth of thin films: General considerations

Well-ordered thin films can be prepared by evaporating the substance onto the surface. The method used in this thesis is called physical vapor deposition (PVD) and is based on the thermal evaporation of the metal. Alternative deposition methods such as molecular beam epitaxy (MBE) [125], cathodic arc deposition [126], pulsed laser deposition [127] and sputter deposition [128] are also well documented.

Another principle of preparing well-ordered thin films is chemical vapor deposition [129] (CVD), in which chemical reactions are involved. In CVD, epitaxial overlayers are grown through chemical processes, in which volatile precursors are involved. Atomic layer deposition (ALD) [130] is a special type of CVD. The difference is that the precursors are injected to the reaction vessel in a sequential and non-overlapping manner. This makes it a more controllable way to prepare films with atomically specified thickness. In addition, the growth of different multilayer structures is straightforward. The main disadvantage of ALD is that it is highly specialized on specific film; in addition, excess precursors and by-products should be removed for not contaminating the final product.

Film growth processes can be described in a phenomenological way. In general, three different modes of film growth can be distinguished, as shown in Figure 3-17.
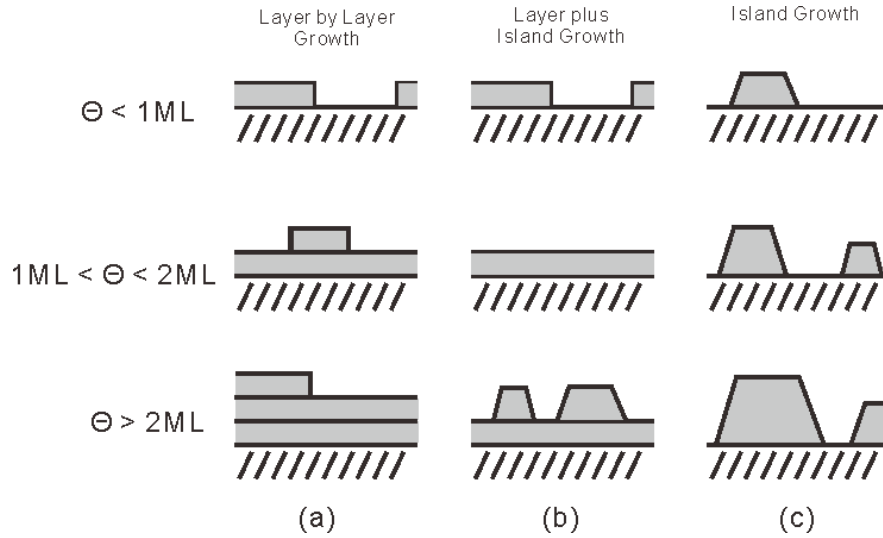
Figure 3-17. Illustration of the three growth modes of film for different coverage regimes. (a) Layer-by-layer growth (Frank-van der Merwe, FM). (b) Layer-plus-island growth (Stranski-Krastanov, SK). (c) Island growth (Vollmer-Weber, VW). Adapted from Lüth [118].

In the layer-by-layer growth mode, also named the *Frank-van der Merwe (FM) mode*, each new layer starts to grow only when the one before has been completed. This is because the interaction between the substrate and layer atoms is stronger than that between neighboring layer atoms.

In the island growth mode, or *Vollmer-Weber (VW) mode*, formation of 3D particles occurs before the whole substrate is covered with a film. The explanation is that the interaction between deposited atoms is stronger than the overlayer-substrate interaction.

The layer-plus-island growth mode, also called *Stranski-Krastanov (SK) mode*, is an intermediate case. After the formation of one or several complete layers, 3D islands start growing. The reason for the transition is deformation of the film caused by lattice mismatch between the film and the substrate, which occurs upon film growth.

From a thermodynamic point of view, the three growth modes are the consequence of a minimization of the total free energy. The free energy per unit area at constant temperature and pressure $\left(\frac{\partial G}{\partial A}\right)_{T,P}$ is denoted by γ. More specifically, γ_S, γ_F and $\gamma_{S/F}$ are the interfacial energies between substrate and vacuum, film and vacuum, and substrate and film, respectively. These interfacial energies are equivalent to the interfacial tension, since they have the same

unit; therefore, an alternative description of the minimization of total free energy can be equivalently made in terms of minimization of surface tension, which is expressed as:

$$\text{total surface tension} = \gamma_{S/F} + \gamma_F \cos\emptyset - \gamma_S ,$$

γ_S: the tension between the substrate-vacuum interface

γ_F: the tension between the film-vacuum interface

$\gamma_{S/F}$: the tension between the substrate-film interface

This is illustrated in Figure 3-18.
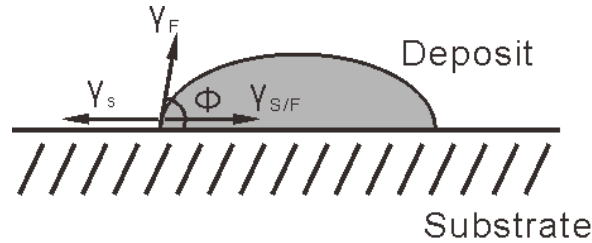
Figure 3-18. Simplified picture of an island of a deposited film; γ$_S$, γ$_F$ and γ$_{S/F}$ are the surface free energies between substrate and vacuum, between film and vacuum and between substrate and film, respectively. Adapted from Lüth [118].

Using this description, the layer-by-layer (FM) and island (VW) can be distinguished by the angle Φ, i.e.,

$(i)\ layer\ growth\ (FM): \ \emptyset \sim 0,\ \gamma_s \geq \gamma_F + \gamma_{S/F}$

$(ii)\ island\ growth\ (VW): \ \emptyset > 0,\ \gamma_s < \gamma_F + \gamma_{S/F}$

The thin film growth can be studied by using AES and X-ray photoemission spectroscopy (XPS). In a uniform thin film system, the electron emitted from the film and finally reaching the detector is described by the following equation:

$$\frac{I^F}{I^F_\infty} = 1 - e^{\left(-d/\lambda\right)},$$

where I^F: intensity of the photoelectron from the film

I^F_∞: intensity of the photoelectron from the film of infinite thickness

λ: mean free path of electrons in the film

d: thickness of the film

whereas the electron emitted from the substrate and reaching the detector is expressed as:

$$\frac{I^S}{I_0^S} = e^{\left(-d/\lambda\right)},$$

where I^S: intensity of the photoelectron from the support

I_0^S: intensity of the photoelectron from the clean support

Combining these two equations, the expression for film thickness based on the photoelectron intensity of film and substrate reads:

$$d = C * Ln\left(\frac{I^F/I^S}{I_\infty^F/I_0^S} + 1\right),$$

where C depends on the emission angle and kinetic energy of the emitting electron.

The plot of this equation looks seemingly like that in Figure 3-19a. At zero coverage, there is no signal from the deposit. As the layer starts growing, the signal from the deposit increases while that of the substrate decreases. This trend continues until the substrate signal disappears, and the overlayer signal reaches the saturation point. Notice that in the course of film growth, change of slopes happens when the nominal coverages reach the next integer. This quantized change of slope, which is not showed in the equation, is due to the perfect layer by layer growth mode, which assumes that a new layer does not start growing before the former layer growth is complete. The Layer plus island growth mode and island growth mode are more complicated to be described analytically; however, the trend of spectroscopic peak intensity with respect to the nominal thickness are shown qualitatively in Figure 3-19. Figure 3-19b shows the trend of island growth mode. Same as layer by layer growth mode, the substrate signal decreases and the deposit signal increases as the nominal thickness rises; however, with a slower rate. This is because the substrate is only partially covered with the overlayer; on the other hand, the incoming deposit accumulates on top of the existing overlayer, resulting in a marginal increase in the overlayer signal. When the amount of deposit increases extensively, the

substrate signal might disappear while the overlayer signal becomes saturated. Figure 3-19c shows the trend of spectroscopic signal with respect to the nominal thickness of the layer plus island growth. At coverage lower than one monolayer, it has the same trend as the layer by layer growth mode. While the nominal coverage becomes larger than one monolayer, the curves behave like that of island growth mode. Based on all these differences, AES and XPS can be used to study the structural growth of deposited material on a substrate.
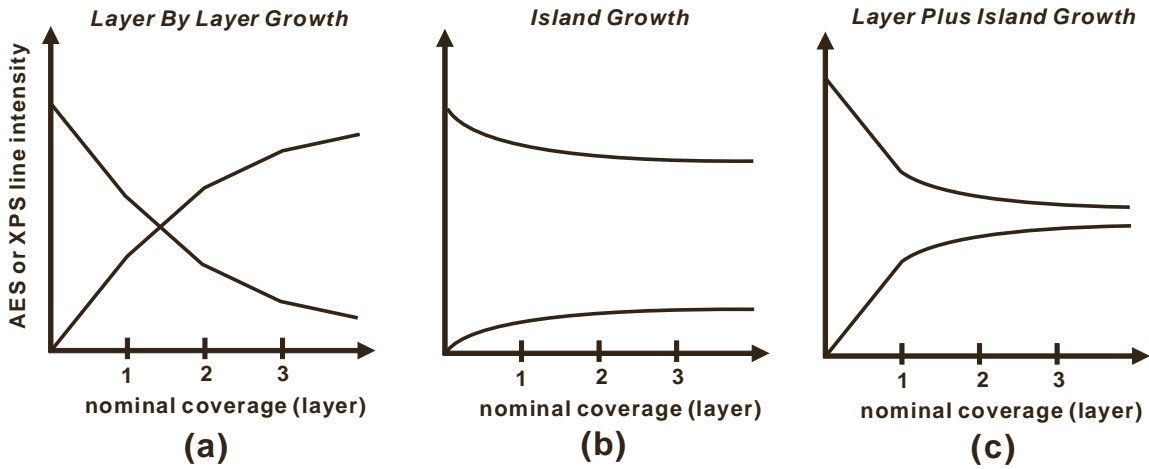

Figure 3-19. Schematic spectroscopic line intensities from deposit and substrate versus the nominal thickness for (a) layer by layer growth mode (FM); (b) island growth (VW) and (c) layer-plus-island growth (SK). Adapted from Lüth [118].

Chapter 4 Preparation of Well-ordered Zinc Oxide Films on Metals

4.1 Zinc oxide films on Pt(111)

Pt(111) is a commonly used substrate for the growth of thin oxide films, because it does not readily oxidize and is resistant towards alloying. Similar to well-documented preparations of e.g. iron oxide films on Pt(111), we started with zinc deposition in UHV and subsequent oxidation. Preparation was optimized for a well-ordered film using brightness of ZnO related diffraction spots observed by LEED as a measure for the long range order of the film. For this, the sample was stepwise annealed (oxidized) and monitored by LEED.

To prepare well-ordered zinc oxide films on Pt(111), zinc was deposited at room temperature in 10^{-7} mbar of O_2. After that, the sample was annealed at 600 K in $2x10^{-6}$ mbar O_2 for 10 min. Figure 4-1 shows STM images of zinc oxide films as a function of coverage. When the thickness is below 2 MLE, the films appear to be flat; in addition, the step height measurements show that the first layer is around 2.5 Å thick. This suggests that the islands are monolayer. Note that the step height in STM topography images is a convolution of the surface morphology and electronic structure; therefore one could not assign the absolute step height value to the film thickness. It can only be used as estimation. The second layer is obviously thicker, with step height of around 4.0 Å. The film grows seemingly in layer-by-layer mode, even though a small amount of bilayer islands appears before the whole surface is covered with the film. Film thickness beyond 1.1 MLE can be reach, by repeating zinc deposition and subsequent annealing in oxygen at the same conditions for several cycles. Figure 4-1e shows a fully covered surface. In this thickness regime, AES is used to investigate the film thickness, as described in detail in section 3.3. Based on this AES study, the film thickness is around 5 MLE. Notice that the surface is decorated with triangular islands. This is a characteristic of the single crystal surface Zn-ZnO(0001), as shown in Figure 2-3. Based on this similarity, one might speculate that the film is zinc terminated. Nevertheless, protrusions with the same periodicity as the coincident lattice of ZnO(0001) and Pt(111) can be seen. Figure 4-1f shows the thickest film in this study, with a thickness that is too thick to be determined by AES. Obviously, the surface becomes rough. The additional zinc oxide sits on the surface without long range order.

The LEED patterns of the same set of film are shown in Figure 4-2. For the films below one MLE, two sets of pattern appear. The larger reciprocal lattice is assigned to Pt(111); the smaller one is assigned to ZnO(0001). Since both sets of reciprocal lattice vectors have the same direction, it was concluded that the overlayer grows epitaxially. As the film grows thicker, the zinc oxide spots become brighter, whereas the Pt spots become weaker. In Figure 4-2d, it can be seen that the zinc oxide spots are surrounded by a set of six spots. This is assigned to a coincident lattice formed at the interface of zinc oxide and Pt(111). These spots are seemingly diffuse, indicating that the interfacial lattice is not well-ordered. This might be due to the flexibility of ultrathin films. The reciprocal lattice shows that the extent of lattice mismatch is around 17 %. This indicates that (5x5) ZnO units are grown on a (6x6) Pt(111) unit lattice, i.e., ZnO(5x5)/Pt(111)-(6x6). Henceforth, this structure is referred to as the $(6x6)_{cp}$ (cp: close-packed) structure in the following text. As the film gets thicker than 5 MLE, as shown in Figure 4-2e, the coincident lattice spots in the LEED pattern become much sharper. This phenomenon agrees with the above-mentioned speculation: the thicker film is less flexible, resulting in a more stable structure, which forms a better-defined coincident lattice with the Pt substrate. Finally, Figure 4-2f shows the LEED image of the thickest film. Neither substrate spots nor the coincident spots can be observed around the ZnO spots. This is because the electrons cannot penetrate the film to reach the interface and the substrate, as the mean free path is much shorter than the film thickness. In addition, the zinc oxide spots become more diffuse, probably due to the lower surface ordering that was seen in the corresponding STM image.

The Auger electron spectra in Figure 4-3 show the zinc peak at 994 eV, and an oxygen peak at 512 eV in addition to the platinum substrate peaks. This confirms the chemical composition of zinc oxide, although the exact stoichiometry cannot be established. An obvious trend can be observed: as the film get thicker, the oxygen peak and zinc peak grow, whereas the platinum peak decreases.
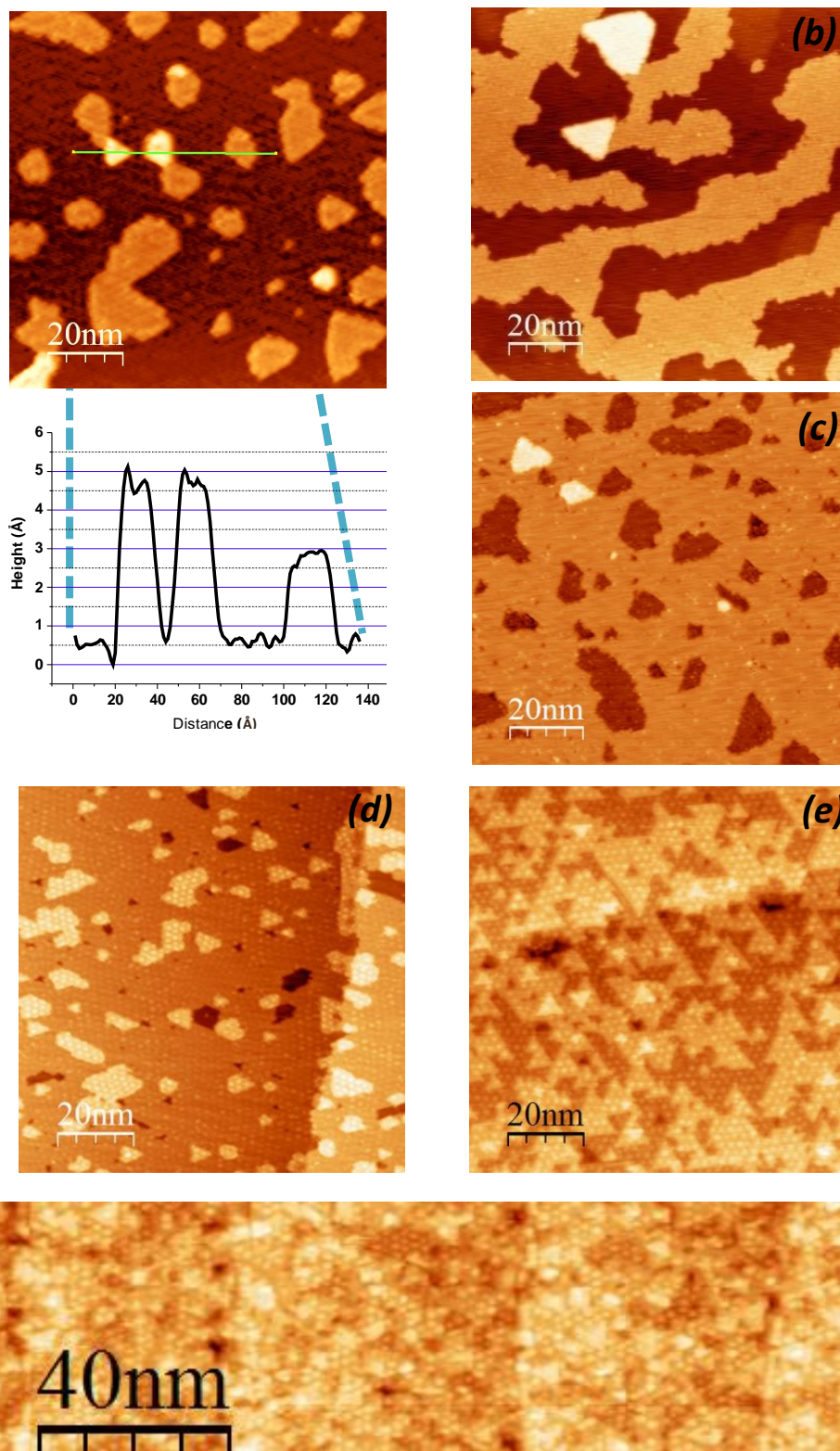
Figure 4-1. STM images of zinc oxide films on Pt(111) as a function of film thickness: (a) 0.25 MLE (2.0 V, 0.7 nA). (b) 0.55MLE (1.0 V, 1 nA). (c) 0.8 MLE (1.0 V, 0.3 nA). (d) 1.2 MLE (2.0 V, 1 nA). (e) >5MLE (1.5 V, 0.5 nA). (f) Thickness not able to be determined anymore due to the saturation in AES (2.0 V, 0.4 nA).
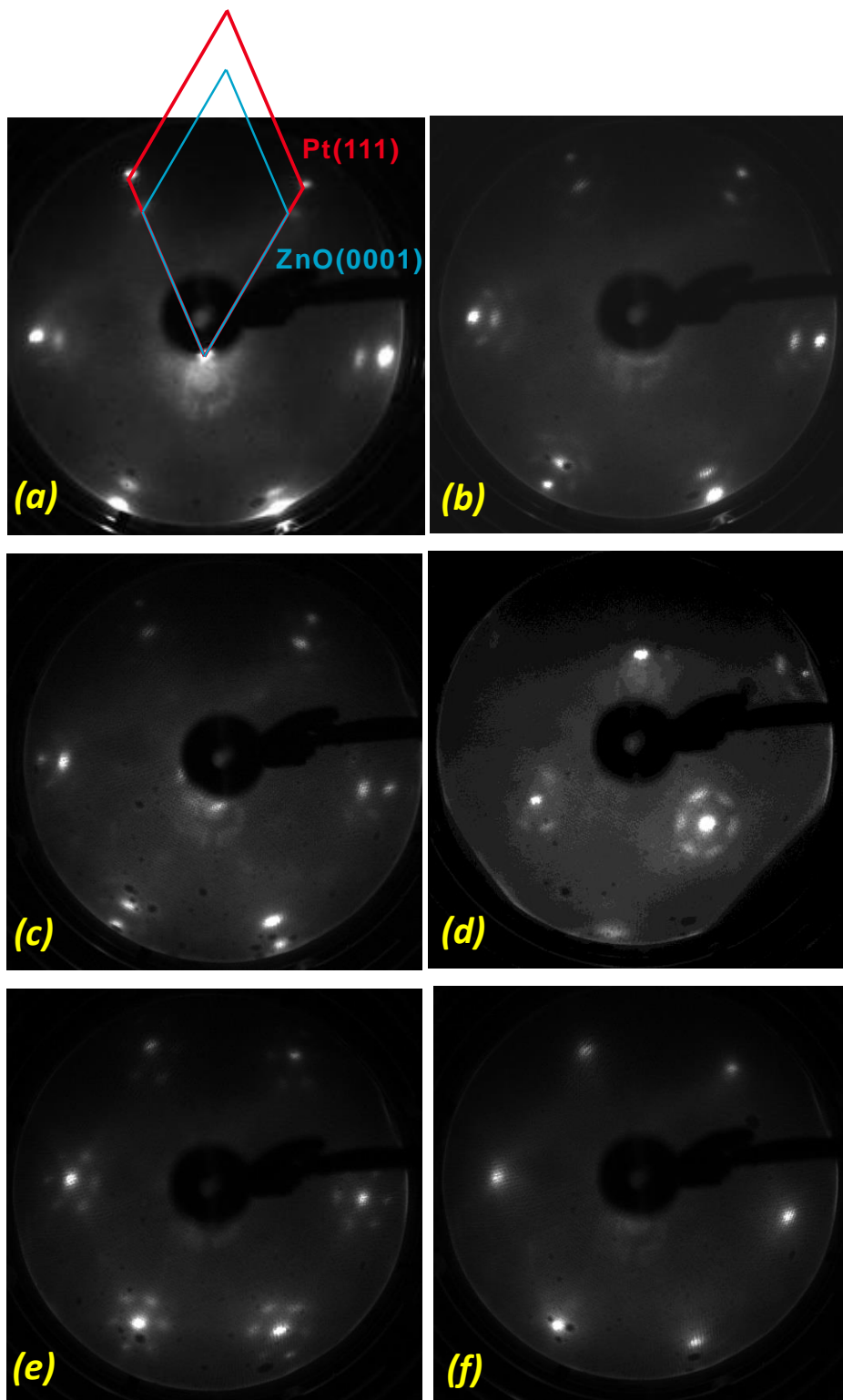
Figure 4-2. LEED patterns of the zinc oxide films on Pt(111) with thickness (a) 0.25 ML; (b) 0.55 ML; (c) 0.8 ML; (d) 1.2 ML; (e) >5 ML; (f) not able to be determined anymore due to the saturation in AES. All images are taken by 64 eV incident electron.
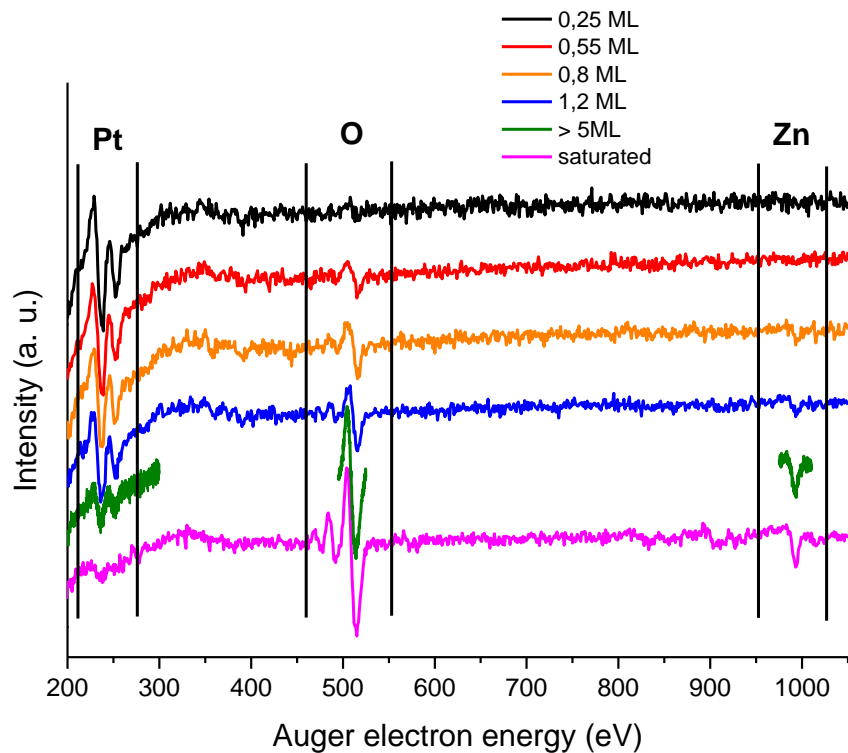
Figure 4-3. Auger electron spectra of zinc oxide films on Pt(111) with different thicknesses. P.s. the missing segment in the spectrum of the > 5 ML film is because the survey spectrum was not taken during that early experiment. The three segments are recorded in three consecutive sessions.

The plot in Figure 4-4 summarizes signal of Pt (236 eV) and Zn (994 eV) peaks of the AES, which were taken between the deposition cycles for growing a thick film. In course of the film growth, the zinc signal increases while that of platinum decrease. The zinc signal is saturated after the 4th cycle, after which the platinum signal almost disappears. The curves behave very similar to that shown in Figure 3-19a. This similarity indicates a layer-by-layer growth mode, which is in line with the conclusion drawn from the STM study.
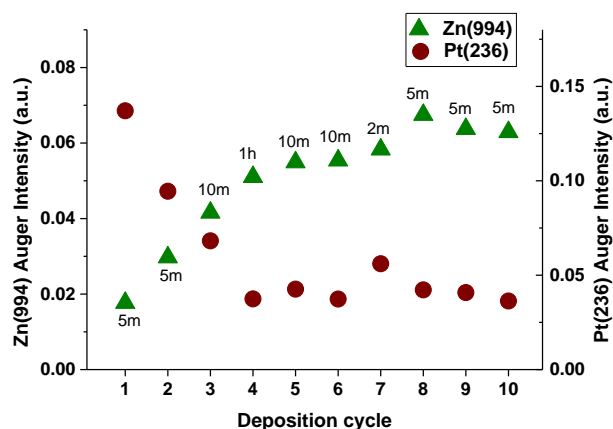
Figure 4-4. The plot of Auger electron intensities in course of a thick film growth procedure, which consists of repeating deposition-anneal cycles. The labels next to the green triangular spots indicate the time of deposition. m: minute; h: hour.

4.2 Zinc oxide films on Ag(111)

As mentioned in the introduction, first well-ordered zinc oxide films on Ag(111) were grown by pulsed laser deposition of zinc oxide followed by an UHV annealing. In our preparation, we used PVD of zinc. We first examined a preparation using Zn deposition in UHV and subsequent oxidation. The blue arrow in Figure 4-5 indicates the process of the film growth. At the starting point, the Ag(111) is clean with terraces as wide as hundreds of nanometers. After zinc metal is deposited onto the surface, corrugated fronts parallel to the silver terraces are observed. These new features are assigned to zinc metal. Looking in more detail, one can see that at the boundary of a zinc metal patch and Ag(111) terrace, there are bunches of parallel line features of around 50 nm in length. It looks like these features originate from zinc metal and cut into the Ag(111) terrace. As more zinc metal is deposited onto the Ag(111), these features become denser and more complicated. As shown in Figure 4-5c, these new features form a network. These observations may be explained in terms of zinc alloying with silver. After the oxidation, the zinc in the surface alloy is oxidized and separated from the alloy. In the STM image in Figure 4-5d, the patches with periodic spots are ascribed to zinc oxide. These spots seem to come from the Moiré-like structure between the zinc oxide and Ag(111). The appearance of the coincident structure shows that the zinc oxide overlayer has an epitaxial relation with the silver substrate.
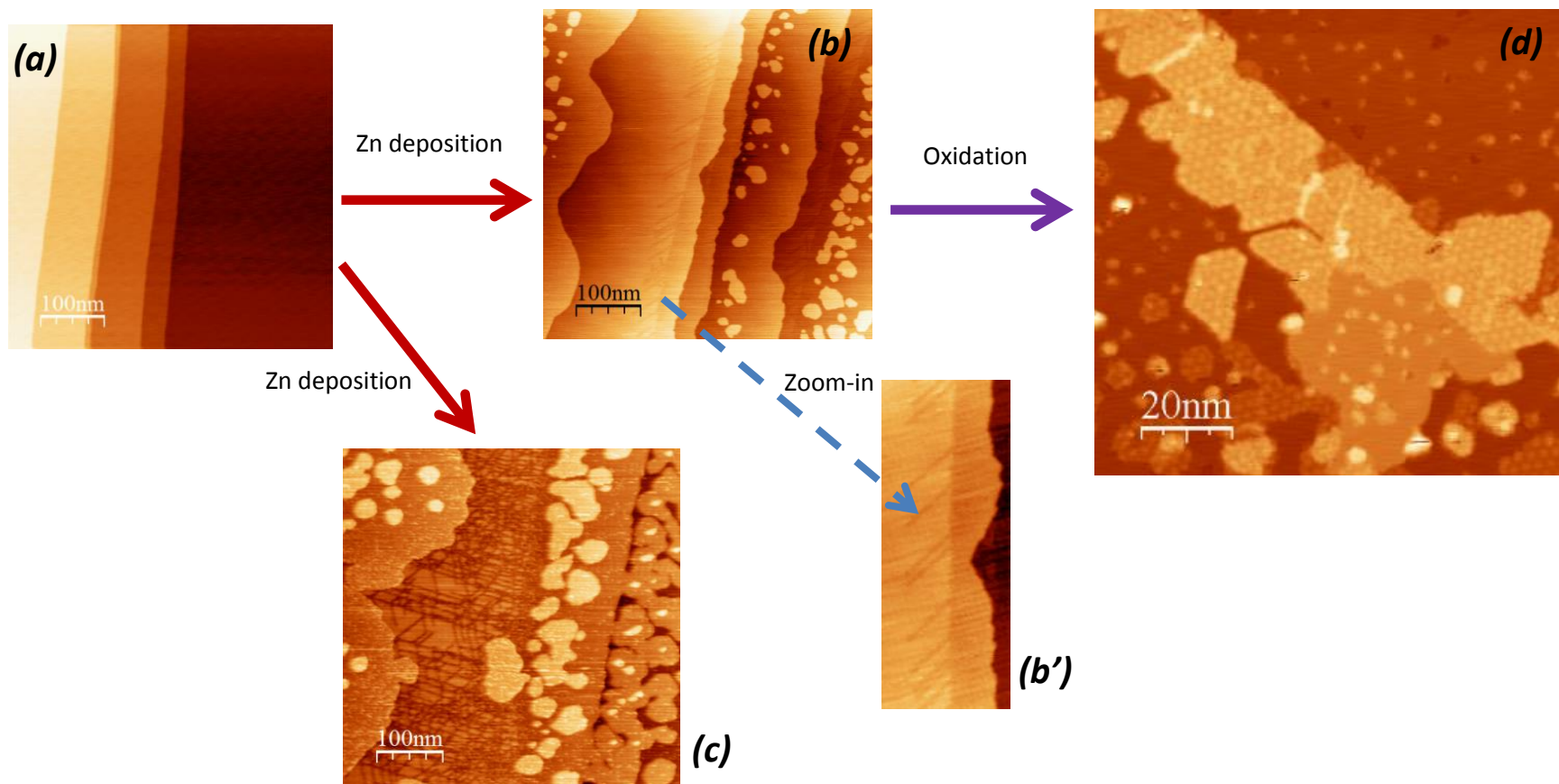
Figure 4-5. Forming of broken terraces by the zinc zinc deposition on Ag(111). The post-oxidation film growth process monitored by STM. (a) Ag(111), (0.05 V, 1 nA). (b) Zinc metal deposited at room temperature under UHV. (b') The zoom-in highlights the alloy structure at the terrace boundary. (c) 2.2 times more zinc metal deposited at the same condition. (d) Oxidized film of the sample with (b) under 1x10^{-6} mbar O$_2$ at 600 K.

Figure 4-6 shows AES and LEED data that correspond to the film shown in Figure 4-5d. In the Auger spectra, in addition to the substrate peaks between 250 eV and 400 eV, oxygen peaks at 512 eV and the tiny zinc peak at 994 eV (shown in inset) indicates that the surface contains zinc and oxygen. In the LEED pattern, two sets of reciprocal lattices were observed. The larger one was assigned to Ag(111), and the smaller one was assigned to ZnO. The same direction of the vectors indicates that the zinc oxide overlayer follows the registry of the substrate.
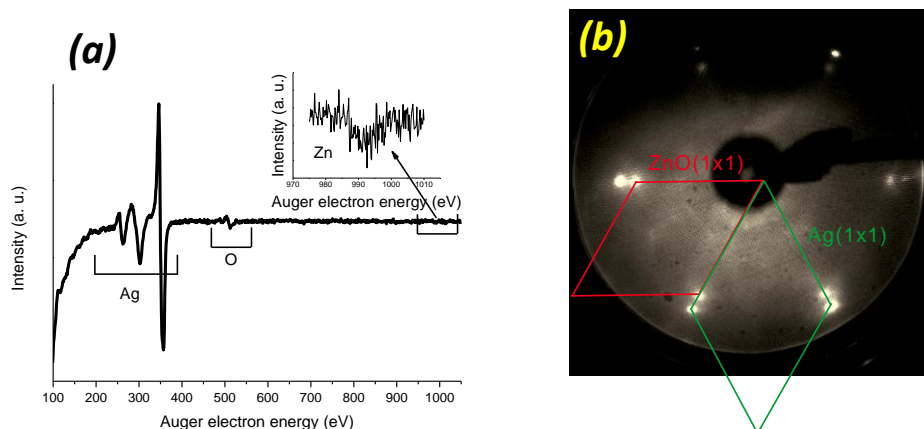
Figure 4-6. (a) LEED pattern, by 75 eV incident electron. (b) AES confirmed the chemical composition: oxygen at 512 eV and zinc at 994 eV. The inset shows the zinc signal with a close-up scan.

To avoid alloying, in the following experiments, zinc was deposited in oxygen. Figure 4-7 shows the sub-monolayer amount of zinc metal deposited onto silver under 1×10^{-5} mbar O_2 at room temperature, followed by annealing in UHV at stepwise increasing temperatures for 10 minutes each. The effect of annealing is obvious: The overlayer becomes better ordered and the Moiré structure appears, as shown in the STM images. Starting from 470 K, the LEED images show weak zinc oxide spots. They become sharper as the annealing temperature increases, as indicated by the white arrows. The optimum annealing temperature is 600 K. The film becomes de-wetted upon heating to higher temperature. Notice that in Figure 4-7a, the uncovered surface shows black pits-like features. The zoom-in image shows that there are linear indentations, which intersect with each other at 60 degrees. This presumably resembles the alloying feature observed on the zinc metal-covered Ag(111), shown in Figure 4-7c; yet the extent is less severe here. Following the same alloying hypothesis, it is suspected to result from the alloying of unoxidized zinc with silver. The reactive deposition in O_2 greatly reduces the alloying. However, the terrace could still be damaged by it to a certain extent. Nevertheless,

these features ultimately disappear upon UHV annealing at 600 K. The final zinc oxide film is closely packed, as shown in the atomic resolved STM image in Figure 4-8.
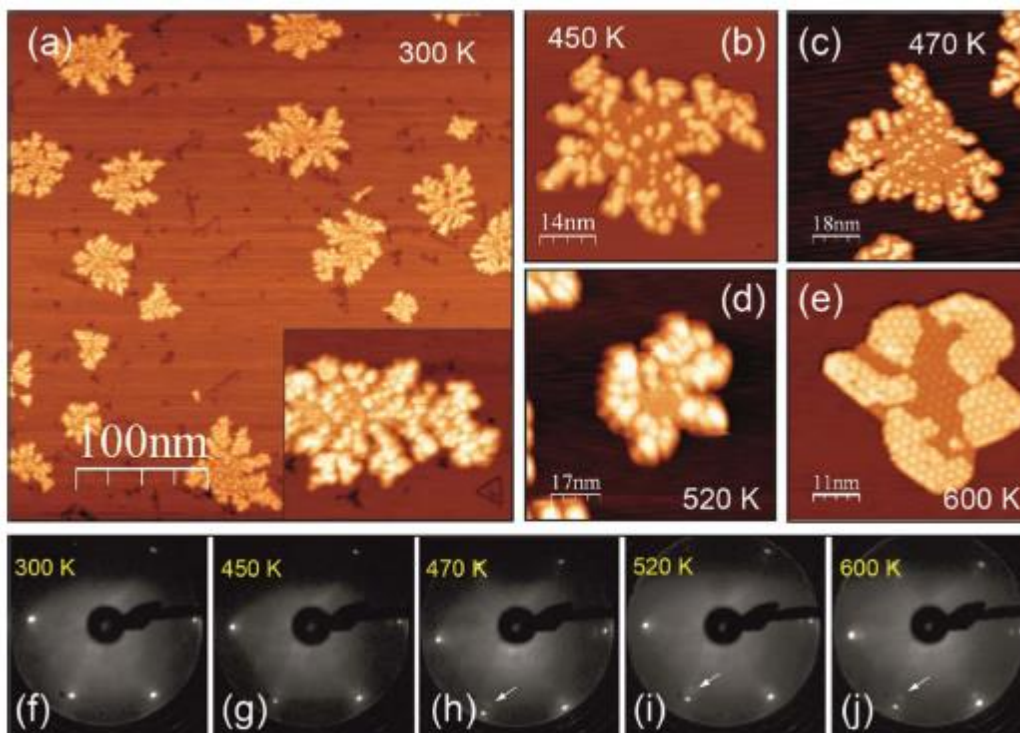
Figure 4-7. The effect of annealing monitored by STM and LEED. Scanning parameter: (a) 1.5 V, 1.2 nA; (b) 1.5 V, 0.3 nA; (c) 1.2 V, 0.2 nA; (d) 1.5 V, 0.6 nA; (e) 1.5 V, 0.6 nA; (f-j) incident electron energy for the LEED patterns are 64 eV. Lattice cells same as those in Figure 3-3b.
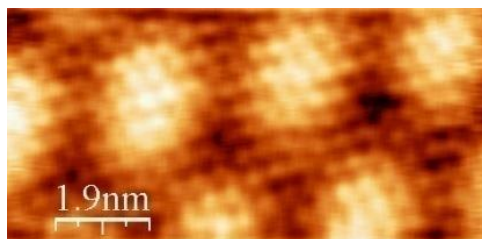
Figure 4-8. Atomic resolved STM image of the zinc oxide on Ag(111). (0.8V, 1.2nA)

Sub-monolayer coverage films were characterized in more detail to reveal the structure of the islands. As shown the STM image in Figure 4-9, the island consists of many domains. Most of the surface area shows a Moiré pattern. The non-Moiré patches are assigned to silver. In principle, three different models can be suggested for the islands, as illustrated in Figure 4-10. In

Figure 4-10a, all zinc oxide layers are either monolayer or bilayer; in Figure 4-10b, all zinc oxide layers are either bilayer or trilayer; in Figure 4-10c, all zinc oxide patches are monolayer.
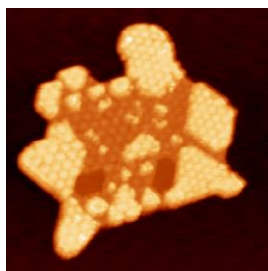
Figure 4-9. STM image of zinc oxide island on Ag(111). Image size: 65 x 65 nm; scanning parameter: 1.5 V, 0.2 nA
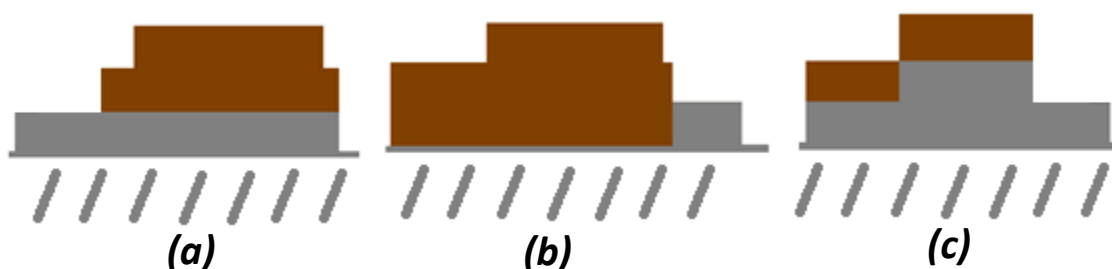
Figure 4-10. Three proposed layer structure of zinc oxide islands on Ag(111), to depict the island layer structure in Figure 4-9. Brown layers represent zinc oxide; gray layers represent silver. In model (a), the two zinc oxide layers exposed are 1st and 2nd, respectively; in model (b), the two zinc oxide layers exposed are 2nd and 3rd, respectively; In model (c), both the exposed zinc oxide layers are the top most layer.

Step heights can be measured with less statistical uncertainty, by image histogram analysis. In this analysis, the image pixels are sorted according to their brightness into a histogram. Since the brightness represents the recorded height, step height information between two patches can be obtained, by measuring the difference between the corresponding peak positions in the brightness axis, as shown in Figure 4-11c. Because in STM, topographical information is convoluted with electronic structure, different voltage bias is applied to reveal the origin of contrast. Figure 4-11 shows the histogram of the two images of the same island obtained at two different biases, e.g. 1 and 1.5 V. Notice that the third peak, which corresponds to the lower of the two zinc oxide layers, does not change its height value upon the change of bias voltage. By contrast, the fourth peak, which represents the height of the higher of the two zinc oxide layers, shifts upon the bias change. This indicates that the layer compositions underneath the two regions are different from each other. In other words, the model in Figure 4-10c, which shows that all zinc oxide patches are single-layer with silver metal underneath, could be excluded.
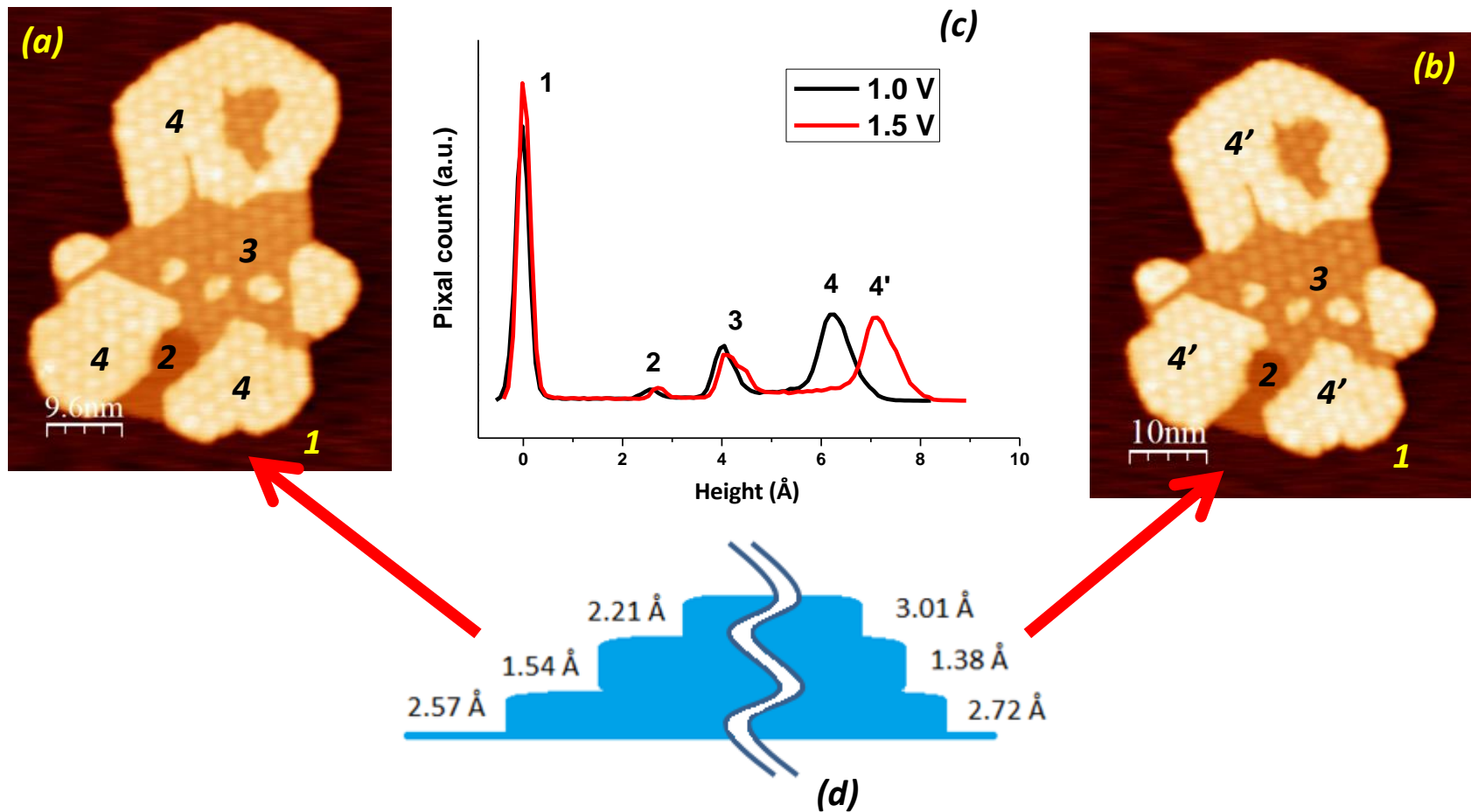
Figure 4-11. STM image of zinc oxide on Ag(111) with different biases. (a) 1.0 V, 0.6 nA. (b) 1.5 V, 0.6 nA. (c) Histogram of height statistics of the images' pixels. The labels on the peaks mark the corresponding patches on the STM images. (d) The illustrated step model representing the step height of the two images concluded from the histogram; those on the left represent step height of 1.0 V image, and those on the right represent that of 1.5 V image.

This conclusion is further supported by the detailed inspection of the Moiré feature. As shown in Figure 4-12, the Moiré spots across the step keep its periodicity without any phase shift. This indicates that both layers that form a coincident lattice remain continuous, which would be not the case in the model illustrated in Figure 4-10c, since the fault would create a discontinuity in the STM image.
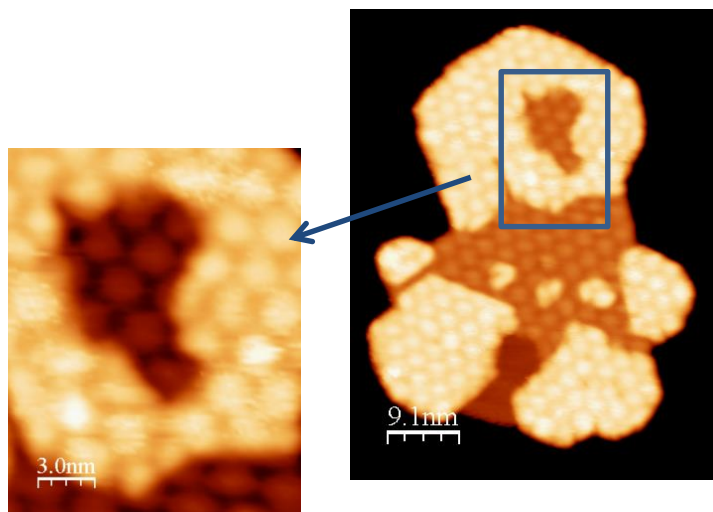
Figure 4-12. The STM image of zinc oxide on Ag(111), highlighting the continuous Moiré structure (1.5 V, 0.6 nA).

Figure 4-13 shows the extended well-ordered zinc oxide film on Ag(111). As in the case of low coverage films, the patches without Moiré superstructure and scatter within the overlayer are assigned to silver. By increasing the amount of zinc deposited, the whole surface could be fully covered by the zinc oxide film, as shown in Figure 4-13b. To determine the thickness of ZnO layer in the films, we performed AES analysis, using ZnO/Pt(111) as a benchmark, where monolayer and bilayer structure are clearly distinguished. AES in Figure 4-13c shows that the Zn LMM 994 eV peak of the film on Ag(111) is roughly twice as large as that on Pt(111) at the same monolayer-film coverage as measured by STM. This indicates that the zinc oxide film on Ag(111) is roughly twice as thick as that on Pt(111). Detailed calculation is presented in the Appendix. Therefore, we concluded that ZnO on Ag(111) grows as bilayer from the onset. Indeed, recent STM analysis suggest this conclusion [131].
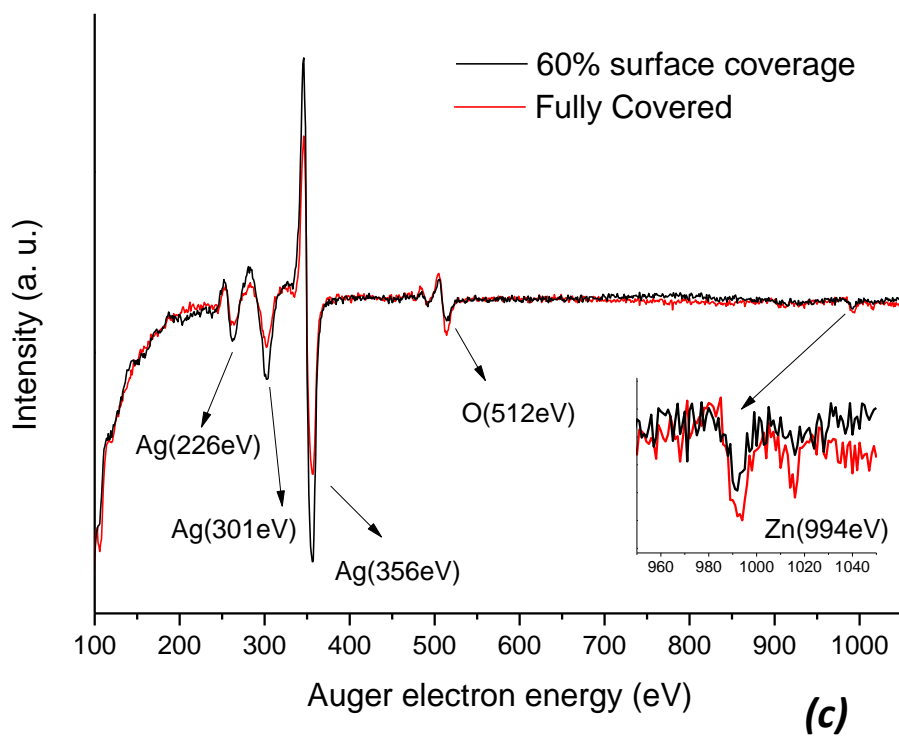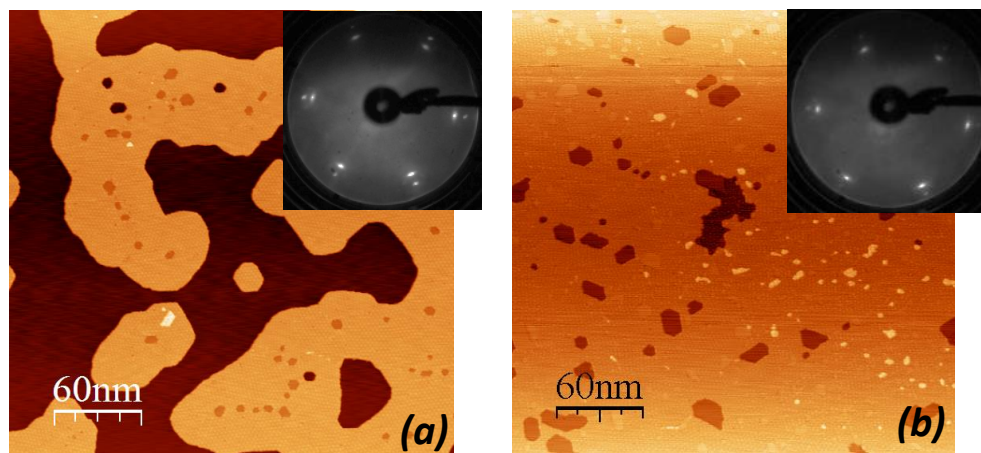
Figure 4-13. Extended zinc oxide overlayer on Ag(111). (a) 60% surface coverage (1.5V, 1.0nA). (b) Fully covered surface. (c) Auger spectra for both film. Both LEED images are taken by 64 eV incident electron, lattice cell is same as those on figure 4.3b.

In order to fabricate thicker films, more zinc was deposited on the surface. However, as shown in the plot in Figure 4-14, in spite of the increase of deposition time (same flux), the amount of zinc on the surface does not increase. Increasing the deposition flux did not help,

either. Another attempt was to repeat the deposition-annealing cycle three times. Still, the increase of zinc is marginal, as shown in Figure 4-15. It, therefore, appears that ZnO on Ag(111) exhibits a "self-limiting" growth.
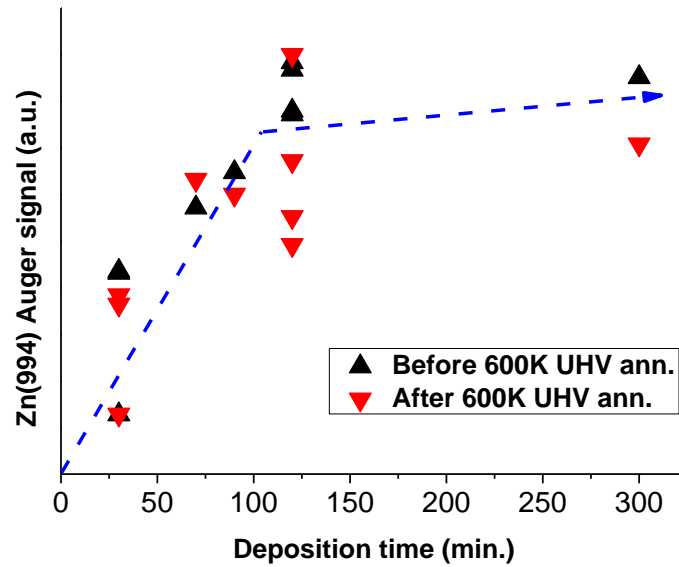
Figure 4-14. The zinc Auger signal from the zinc oxide films on Ag(111) as a function of the deposition time, with all other parameters unchanged. The dash line is to guide the eye.
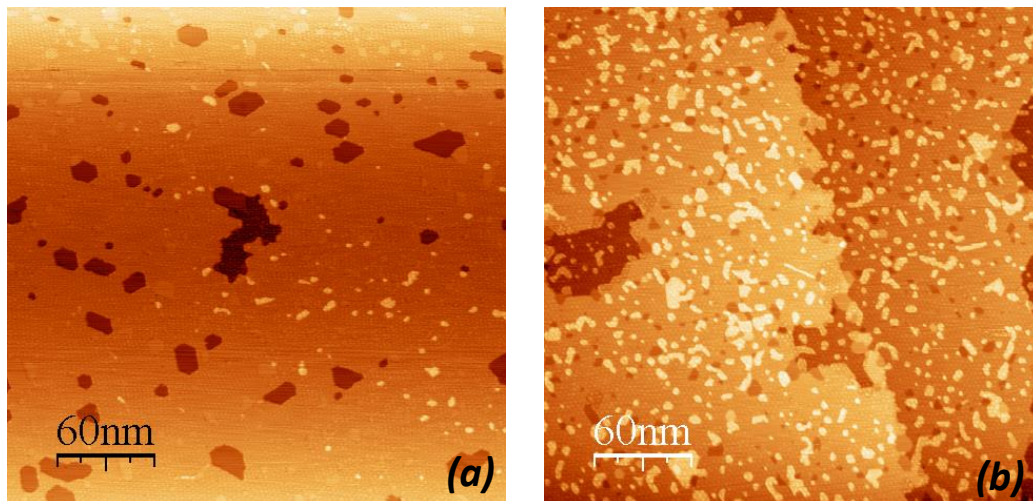
Figure 4-15. The "self-limiting growth" of the zinc oxide film on Ag(111) depicted by STM and AES. (a) 60 minute deposition, Zn(994)/Ag(356) = 3.3 %. (b) Another 60 minute deposition on the same film, Zn(994)/Ag(356) = 4.3 %.

Notice, that the self-limiting growth is only observed when the zinc is deposited in oxygen. Metallic zinc could be deposited on the silver surface without limitation. However, the alloying prevents the preparation of a well-ordered film on intact terraces. The oxygen pressure applied during the deposition also has an influence on the final film structure. Reducing the oxygen pressure during zinc deposition from 1×10^{-5} mbar to 5×10^{-6} mbar, results in a film containing more structural variety, as shown in Figure 4-16. The zinc oxide layer in the area (circled in green) at the center of the image has the same Moiré structure as the "normal" layer. The red circle highlights the zinc oxide patch with smaller Moiré periodicity with respect to Ag(111). This is probably due to the relative rotation of the zinc oxide overlayer to the substrate. The blue circle indicates the region with higher contrast of Moiré structure, while the periodicity remains the same as that circled in green area.
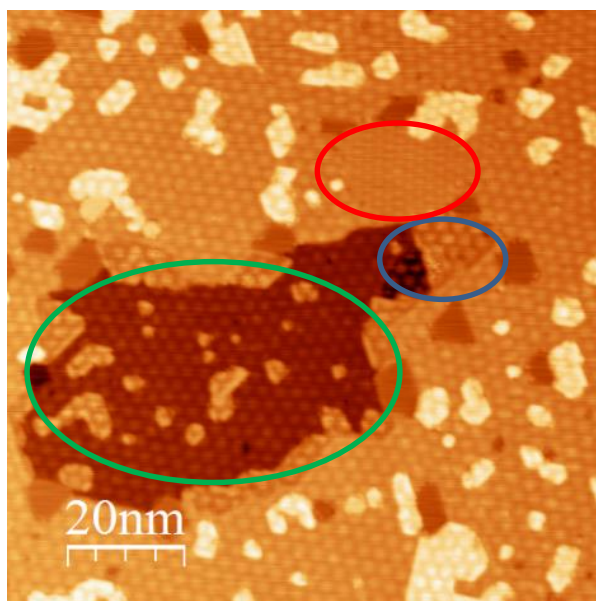
Figure 4-16. Zinc oxide film on Ag(111). The reactive deposition is conducted with half of the normal oxygen pressure, namely, 5×10^{-6} mbar. STM scanning parameter: 0.9 V, 0.8 nA.

4.3 Zinc oxide films on Cu(111)

Cu(111) was chosen because the zinc oxide and copper combination is the active catalyst for methanol synthesis reaction. The first recipe tested is metallic deposition followed by an oxidation in elevated temperature. Unlike in the case of Ag(111), there is no indication of the alloying of zinc with copper at room temperature. Zinc forms islands on Cu(111), as shown in

Figure 4-17a. Subsequent oxidation treatments, however, could not turn the metallic zinc into a well-ordered zinc oxide layer. As shown in Figure 4-17b, the edge of the zinc islands transferred into irregular structures upon exposure to 1×10^{-6} mbar O_2 at 300 K. The area of this irregular structure grows larger as the sample temperature increases while being exposed to the same oxygen pressure. The rise of the oxygen signal in the AES, as summarized in Figure 4-17h, shares the same trend with the growth of the irregular edge features in STM images. It can therefore be concluded that the new feature is zinc oxide. After being annealed to 500 K, the zinc transfers to zinc oxide completely, in a worm-like structure with 10-12Å in height, which corresponds to roughly four to five atomic layers of ZnO.
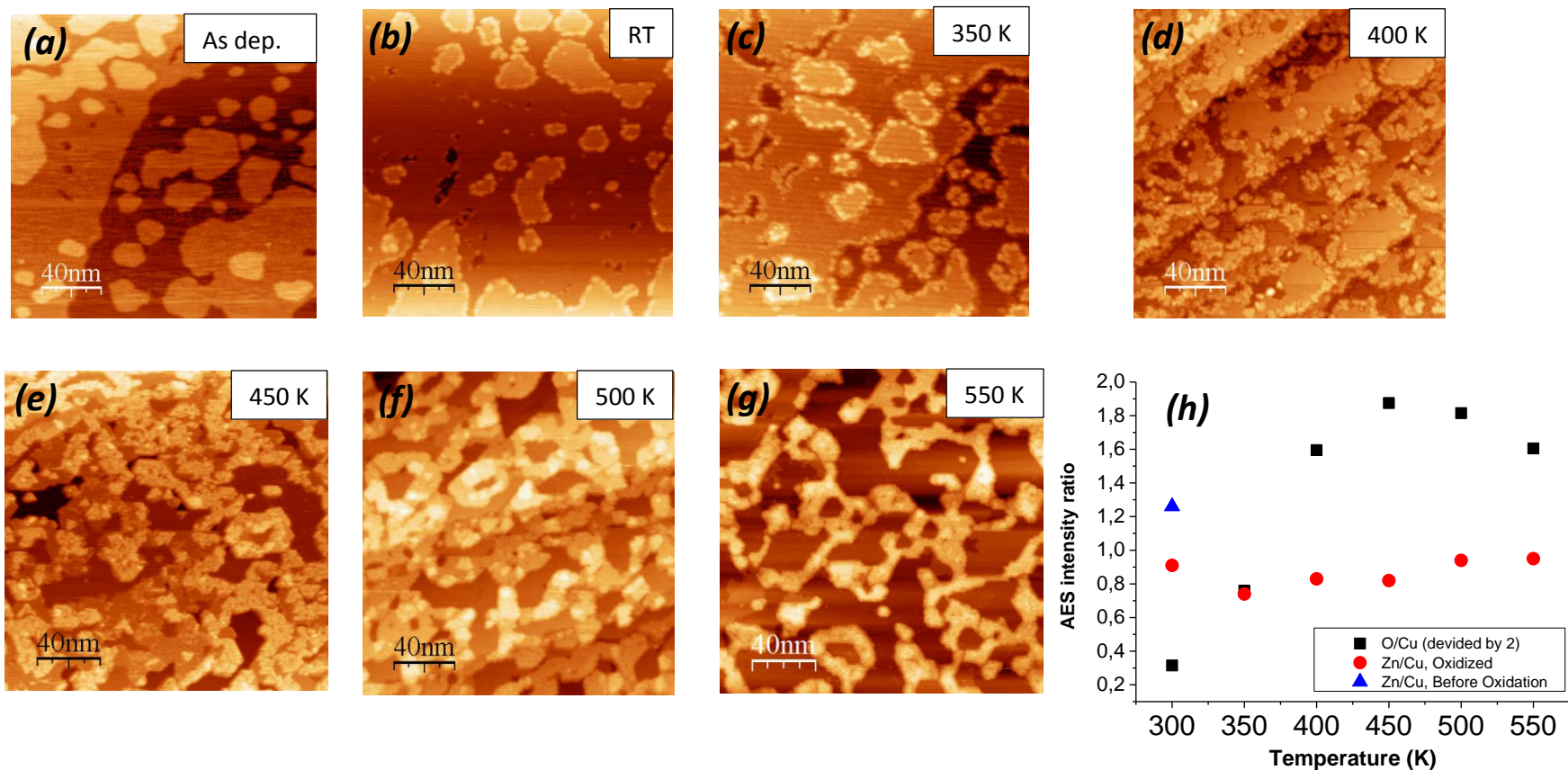
Figure 4-17. Zinc oxide on Cu(111) by metallic zinc deposition followed by oxidation with 1x10⁻⁶ mbar, at the different temperatures indicated. The AES signals of zinc and oxygen divided by Cu are plotted in (h). STM scanning parameters: (a) 1.0 V, 1.0 nA; (b) 2.0 V, 0.7 nA; (c) 1.0 V, 0.7 nA; (d) 1.5 V, 0.7 nA; (e) 2.0 V, 0.7 nA; (f) 1.7 V, 0.7 nA; (g) 1.5 V, 0.7 nA

In the next set of experiments, reactive deposition was tested as a way to make a well-ordered zinc oxide film on Cu(111). The zinc is deposited onto the surface at room temperature under $1x10^{-5}$ mbar O_2. After that, the sample was annealed in UHV. The samples are characterized after heating to different temperatures to find the optimum annealing temperature. In Figure 4-18, AES confirmed the existence of zinc and oxygen on the surface; LEED and STM show that the zinc oxide gradually becomes ordered and form an epitaxial relation to the Cu(111) substrate as the annealing temperature increases. It finally turns into a well-ordered film at 500 K, but eventually becomes dewetted at 600 K. The fully covered film shows smaller domains than those observed on Ag(111), presumably due to the larger lattice mismatch between ZnO(0001) and Cu(111), as compared to ZnO/Ag(111) (27.5 % and 12.5 %, respectively). As on Ag(111), all attempts to grow a thicker film were not successful.
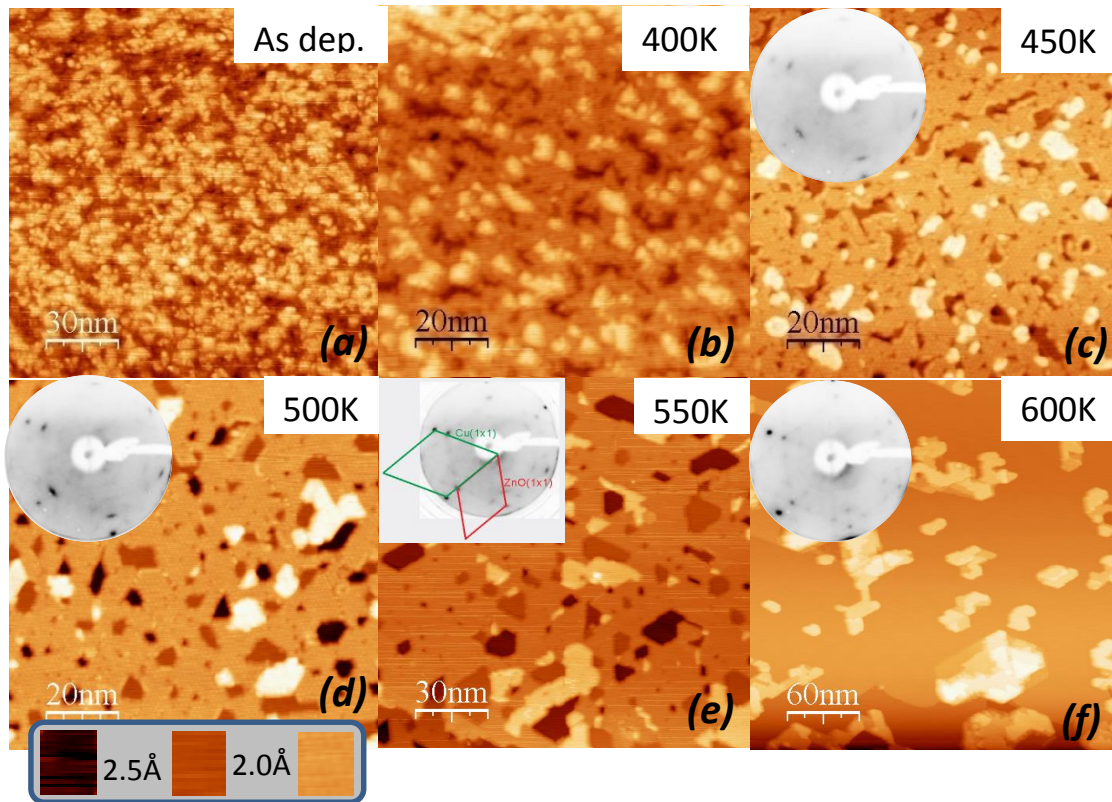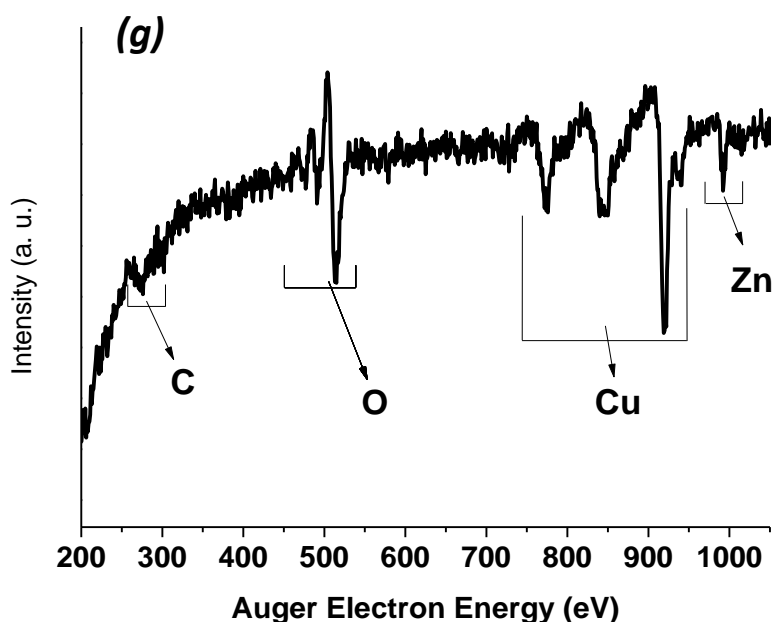
Figure 4-18. Zinc oxide grown on Cu(111). (a-f) STM and LEED pattern of the sample annealed at the indicated temperature in UHV for five minutes. (g) The AES of the sample corresponding to 500 K annealing, which is the optimum temperature. The step height information of the film of optimal ordering is illustrated in the box under (d). Incident electron energy for all LEED patterns is 64 eV; STM parameters: (a) 1.5 V, 0.6 nA; (b) 2.0 V, 0.6 nA; (c) 1.5 V, 0.8 nA; (d) 1.2 V, 0.6 nA; (e) 1.2 V,0.4 nA; (f) 1.2 V, 0.6 nA. Reciprocal lattice of LEED pattern shown in (e).

Numerous preparations of zinc oxide films on Cu(111) revealed that the resulting surface structure is more complex as compared to zinc oxide on Pt(111) and Ag(111), since copper is prone to be oxidized at 10^{-5} mbar O_2. Therefore, additional methods/techniques need to be employed to investigate this system, to see whether it adequately represents the catalyst for methanol synthesis.

4.4 Summary and conclusions

In this chapter, it was described in detail the preparation of well-ordered ultrathin zinc oxide films on three metal supports using Zn physical vapor deposition and oxidation, and their combination. On all substrates, the film grows in (0001) orientation. On Pt(111), the film grows in a layer-by-layer mode, starting from a monolayer, ultimately reaching surface structures characteristic of Zn-ZnO(0001) single-crystal surfaces. On Ag(111), the alloying of zinc and silver

made it necessary to deposit Zn in relatively high O_2 pressures. The resulted films form bilayer structures (i.e., two ZnO sheets) from the onset. Further growth to obtain multilayer films turned out to be very difficult, indicating some sort of "self-limiting" growth. The latter behavior is observed on the Cu(111) substrate, which is a less well-defined system, due to the simultaneous formation of CuO_x layer(s) and its intermixing with ZnO.

Chapter 5 Polar Stability of Zinc Oxide Films on Metals: Reconstruction vs Hydroxylation

5.1 Substrate effects: Reconstruction vs hydroxylation

Figure 5-1a shows the STM image of the as-prepared zinc oxide film on Pt(111). It is about 5 monolayer equivalent (MLE) thick, as determined by XPS and AES. The film grows in [0001] orientation as judged by LEED.
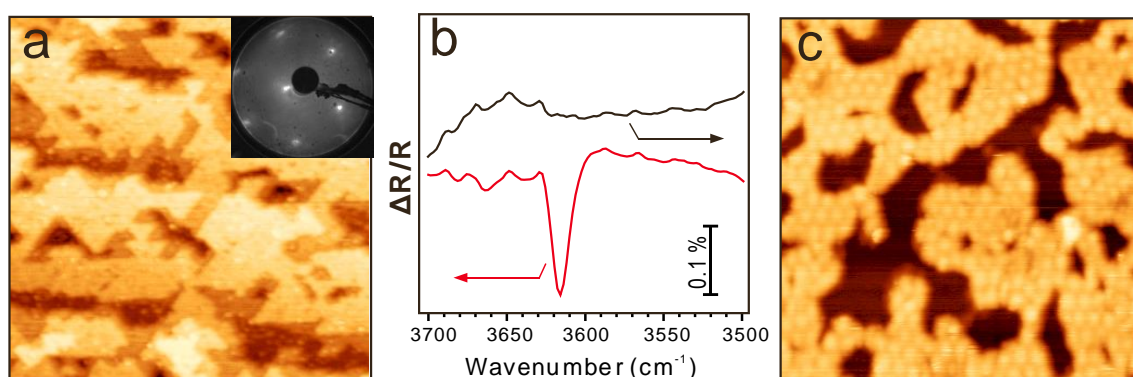
Figure 5-1. As-prepared zinc oxide films on (a) Pt(111), LEED incident energy 55 eV, STM tunneling condition (1 V, 0.02 nA), and on (c) Ag(111), STM tunneling condition (1.0 V, 0.06 nA). The corresponding IRA spectra in the OH stretching region are shown in (b).

This 5 ML-thick film shows many triangular pits and islands. This is very similar to the Zn-terminated ZnO(0001) single crystal surface. Based on this similarity, it could be speculated that the film is Zn-terminated. This speculation seems counterintuitive, however, since the clean ZnO(0001)-Zn surface is usually prepared by annealing in UHV at 900 K, whereas the preparation of thick films involves oxidation in 10^{-6} mbar O_2 at 600 K. Thus, it should favor an O-terminated surfaces.

The surface termination of the thick film is further investigated by IRAS. In the spectrum shown in Figure 5-1b, the sharp and intense peak at 3620 cm^{-1}, which corresponds to an OH stretching, indicates the existence of a considerable amount of hydroxyl group on the film. The OH coverage is estimated to be 15 %, using the OH-covered silicate film [132] that is grown in the same UHV chamber for calibration. The observed frequency is exactly the same as the OH stretching frequency measured by HREELS on the OH-covered ZnO(0001)-O single crystal surface,

prepared by water adsorption on the (1x3)-reconstructed surface [48]. (Note, however, that early IRAS studies of the same group on the H(1x1)-ZnO(0001) surface, although carried out in another UHV setup, showed a vibrational band at 3572 cm^{-1} [133].) The presence of OH species on the "as grown" films is a bit surprising as the films were prepared in the H-free atmosphere and even cooled down to room temperature in oxygen ambient. On the other hand, this finding supports a previously sound view [28, 134](although argued in ref [135]) that a defect-free, pure O-terminated ZnO(0001) surface can hardly be observed in experiment. A plausible model for this as-prepared zinc oxide film is that the top layers resemble the hydroxylated oxygen terminated ZnO(0001)-O single crystal surface. A question then follows: where does the hydrogen come from?

Two possible scenarios are proposed here. The first is the reaction of the film with hydrogen-containing residual gas in the chamber, such as H_2 and H_2O. This possibility was technically difficult to evaluate, since the film is already hydroxylated as prepared in oxygen ambient. The second scenario was that the film react with the H atom provided by residual H_2, which is dissociated on the Pt(111) surface. To evaluate this hypothesis, the zinc oxide film grown on Ag(111) substrate, which does not dissociate H_2, was further studied by IRAS. The morphology of the film is shown in the STM image in Figure 5-1c. The film does not cover the whole surface, in order to better see the effect of the substrate. The IRA spectrum in Figure 5-1b indicates that the as prepared film on Ag(111) shows no signature of hydroxyl. It seems that the substrate plays a crucial role on the film hydroxylation. To further verify this conclusion, ~20 L of H_2 or D_2O was dosed onto Ag(111) supported zinc oxide at room temperature. However, no hydroxyl groups were observed in the IRA spectra.

The observation that the zinc oxide film on Ag(111) is not hydroxylated agrees with the studies, which are based on surface X-ray diffraction study and DFT calculation, and concluded that the zinc oxide film on Ag(111) adopts the h-BN-like structure. It seems very unlikely, if not impossible, that a non-polar film could stabilize a highly polar-inducing adsorbate like hydroxyl. Based on the abovementioned experiments and argument, one could conclude that in the case of zinc oxide thin film on a Ag(111) support, the depolarization mechanism via interlayer relaxation prevails over hydroxylation.

One might argue that the zinc oxide film as thick as 5 MLE on Pt(111) substrate has already transformed into the bulk-like Wurtzite structure, as predicted by DFT [77]. It is questionable to compare the film with different thickness and attribute their different behavior to the effect of the substrate. To eliminate this doubt, the monolayer and bilayer zinc oxide film on Pt(111) substrate were grown and characterized by IRAS.

5.2 Thermal stability of OH-terminated zinc oxide films on Pt(111)

Figure 5-2 shows the IRA spectra of monolayer, bilayer and the ~ 5 MLE film on Pt(111). Both the bilayer and monolayer films show significant peaks attributed to hydroxyls. Compared to the 5 MLE film, the bilayer film shows essentially the same frequency and density of OH species. On the other hand, the peak from the monolayer is much weaker, with a frequency of roughly 3580 cm^{-1}, which is red-shifted by around 40 cm^{-1}, as compared to other two cases.
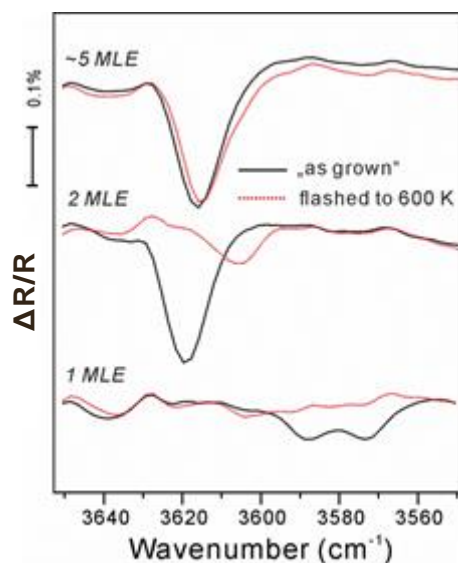
Figure 5-2. IRA spectra of different thickness zinc oxide films on Pt(111) support. Black curve: as grown; red curve: flashed to 600 K.

Thermal stabilities of these OH groups were tested. The films were flashed to 600 K in UHV. The temperature was chosen to avoid the film decomposition which occurs at a higher temperature. The result of IRAS measurement is shown in Figure 5-2. The black curves and red curves represent the IRA spectra of the film before and after the thermal flash, respectively.

Apparently, the stabilities of the OH groups are thickness-dependent. The OH on the thick film is not affected by the thermal flashing; that on the bilayer film remains 20% of the signal before the flash, with a significant red shift, indicating lower OH density. The OH on the monolayer film is completely removed after the flash. It could therefore be concluded that the thicker the films are, the more thermally stable their OH is.

This thickness dependence could, in principle, be rationalized by a so-called "capacitor" model [68], which is described as follows. In a plate capacitor, the energy stored inside is formulated as:

$$E = \frac{1}{2}\varepsilon A d U_d^2,$$

ε: permittivity

A: plate area

d: distance between two plates

U_d: dielectric strength

Assuming that all the other parameters are unchanged, the energy is proportional to the distance between the two plates. The extended layer structure of the zinc oxide films grown in the [0001] direction consists of alternating Zn^{2+} and O^{2-} layers. This could be viewed as a stacking of plates containing alternative positive and negative charges. The layers in between do not contribute to the energy of the whole system, since they cancel out. The energy is solely determined by the two outer most layers. Therefore, the thicker the film is, the farther away the two outermost layers are, which creates a larger dipole moment. Since the hydroxylation of the polar thin film systems is driven by the dipole moment it contains, higher stability of the OH group on thicker film could be reasonably assumed.

To know more about the thermal stability of OH groups on different layers, a series of IRA spectra was collected upon stepwise heating, on a monolayer film that is decorated with bilayer islands. As shown in Figure 5-3a, the film consists of a ~90 % surface coverage, in which ~17 % are bilayer islands. It seems reasonable to expect that the OH of the monolayer film and bilayer film could be observed simultaneously.
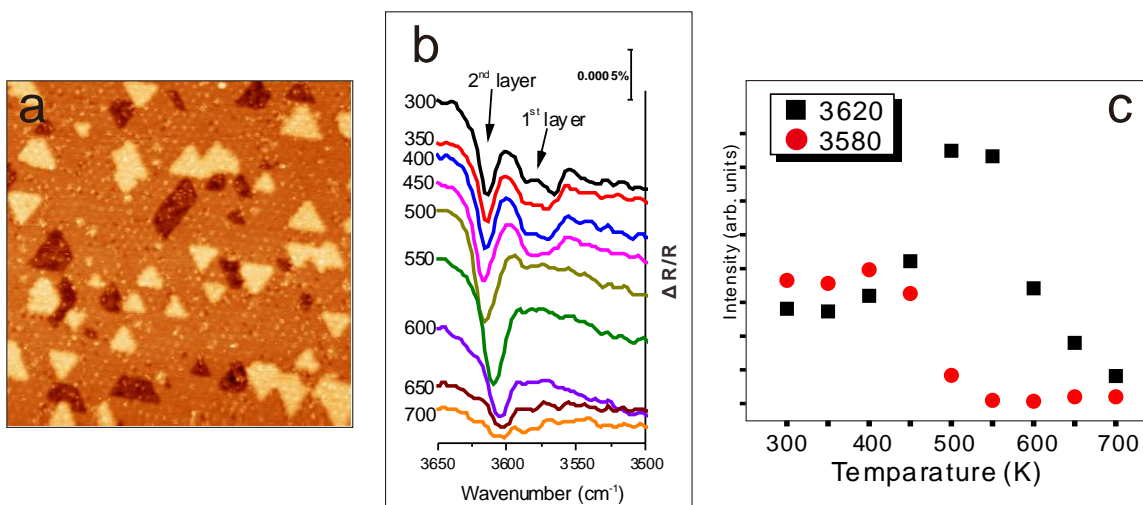
Figure 5-3. (a) 1.1 MLE zinc oxide film on Pt(111). STM tunneling condition: (1 V, 0.1 nA); (b) TP-IRA spectra; (c) peak area plot of OH on monolayer and bilayer.

The IRA spectrum of the 1.1 MLE zinc oxide film on Pt(111) is shown in Figure 5-3b. The OH on both monolayer and bilayer are observed: the sharp 3620 cm^{-1} peak representing that on the second layer, and the weak broad peak at 3580 cm^{-1} representing that on the first layer. The bilayer peak is stable up to 700 K, while the monolayer peak disappears after 500 K. This agrees well with previous experiments. It is noteworthy that, starting from 450 K, the OH signal on the second layer increases, at the same time that on the first layer decreases. This can be seen more obviously when the relative peak area is plotted in Figure 5-3c. This growth and decline of the OH group signal indicates mass transfer: Either the OH group spills from the first onto the second layer, or the ratio of the first and second layers' zinc oxide layer changes on heating. As a benchmark, the same experiment was conducted on the film covered preferentially by bilayer islands, as shown in Figure 5-4. Only the peak corresponding to the OH on the bilayer is observed. In addition, as plotted in Figure 5-4c, no OH intensity increase is observed.

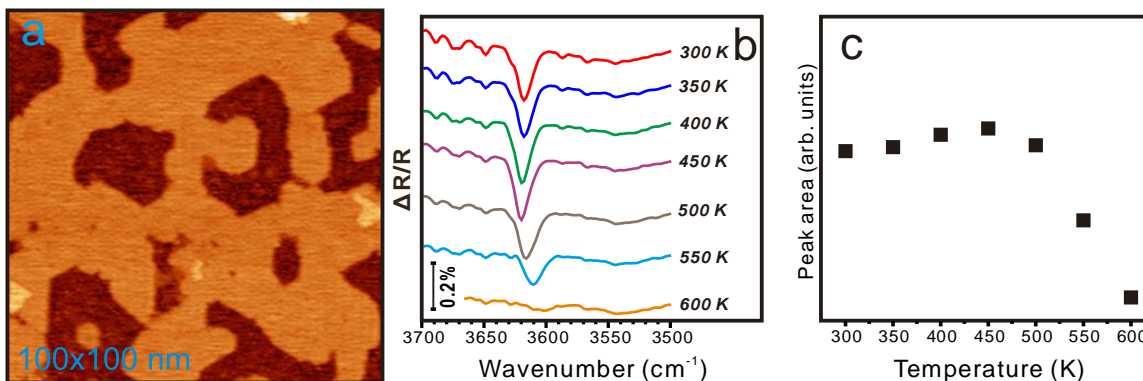**Figure 5-4. (a) 60 % surface coverage of bilayer zinc oxide film on Pt(111), STM tunneling condition: (2.0 V, 0.5 nA). (b) TP-IRA spectra. (c) Peak area plot of OH on bilayer.**

The morphological change observed by STM suggests a possible explanation for the IRAS observations. Figure 5-5 shows the morphology before the surface were flashed to 600 K in front of QMS to record a TPD spectrum. As seen in the water TPD spectrum in the inset of Figure 5-5a, water desorbs from the film at ~350 K and ~520 K, most likely via recombination of two hydroxyls. Additional STM and LEED characterization showed that the loss of water that corresponds to the peak at 350 K has no influence on the morphology. On the other hand, the water loss at 520 K causes a significant change in the morphology, as shown in Figure 5-5b. Two main observations of morphological changes should be pointed out. First, the surface coverage of the bilayer island increases, at the expense of the first layer. This is indicative for a partial dewetting of the film, with the bilayer islands growing at the expense of monolayer structures. This agrees well with the IRAS experiments shown in Figure 5-3c, which implies that the hydroxylated zinc oxide from the first layer migrates to form a second layer. Secondly, the first layer shows a honeycomb-like structure. The periodicity of the holes is the same as that of the Moiré structure of the $(6\times6)_{cp}$, and therefore named as $(6\times6)_{hc}$, where the hc stands for honeycomb. Interestingly, it is similar to the (5×5) honeycomb structure observed on the annealed HO-ZnO(000$\bar{1}$) single crystal surface (see Figure 2-9b). In the inset of Figure 5-5b, the high-resolution STM image shows the atomic arrangement. Unfortunately, solely based on STM it is not possible to know whether the protrusion originates from zinc or oxygen. A DFT study of ultrathin zinc oxide film on Pd(111) [77] suggested that the contrast in the STM image comes from oxygen. Based on the fact that the ZnO structures are similar on Pd(111) and Pt(111), it seems plausible that on Pt(111) the STM image of a zinc oxide film is defined by oxygen as well. Based on this assumption, these periodic holes are caused by the loss of lattice oxygen.

However, the AES spectra before and after heating do not reveal sufficient differences to draw a firm conclusion about compositional changes of the film.
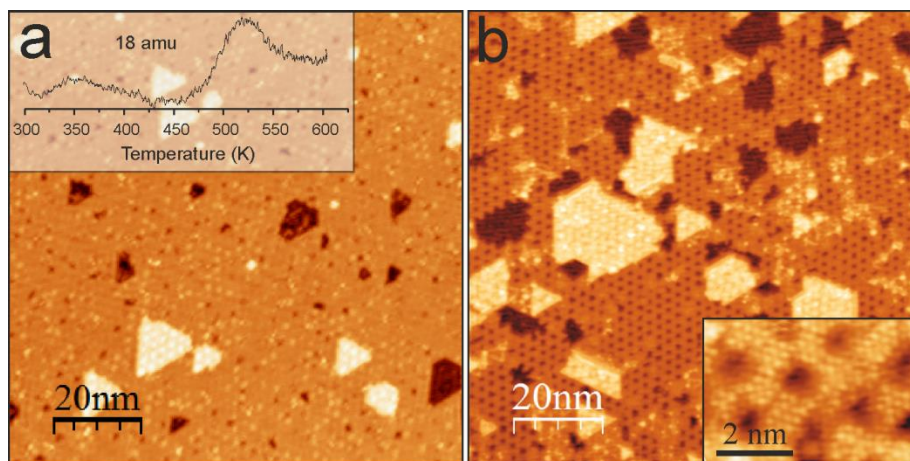
Figure 5-5. (a) 1.1 MLE of monolayer zinc oxide film on Pt(111), STM tunneling condition: (2.0 V, 0.6 nA), (inset): TPS of m/z=18 amu from RT to 600 K. Two peaks appear at 360 K and 526 K, respectively. (b) Flashed to 600 K in UHV, STM tunneling condition: (1.5 V, 0.6 nA), (inset) atomic resolved zoom-in image, STM tunneling condition: (0.065 V, 0.5 nA).

The films prepared on Pt(111) are all annealed to 600 K and cooled down in O_2. The samples were all cooled down in oxygen to prevent potential reduction, since annealing in UHV was shown to result in morphological changes of the monolayer film and the loss of hydroxyls in monolayer and bilayer films. Since the UHV-annealed monolayer films showed considerable morphological changes, we also examined a monolayer film prepared at 600 K, with oxygen pumped out simultaneously with cooling. As shown in Figure 5-6a, the STM image reveals the structure which is named as "donut" structure. The protruding spots arranged with a periodicity like the Moiré spots exhibit a few missing protrusions in the center. The atomic protrusions display a ~3.4 Å periodicity, similar to that derived from the lattice constant of a ZnO single crystal. Based on DFT calculations of the zinc oxide film on Pd(111), the missing protrusions are tentatively assigned to O vacancies which are formed in vacuum at the beginning of cooling while the sample was still at relatively high temperatures. Obviously, the final structures, shown in Figure 5-5b and Figure 5-6a and b, must not necessarily be the same, as they may depend on the "initial" state and also be kinetically limited, thus depending on the cooling (heating) rate. Nonetheless, the mechanism for oxygen vacancies formation on ZnO monolayer in both preparations seems to be similar, since both structures are exposed to high temperature in high

vacuum. Note again that, for both surfaces, the missing protrusions in STM images are distributed not randomly, but at the specific sites within the Moiré unit cell. It, therefore, appears that the oxygen vacancy formation depends on the registry between the zinc oxide monolayer and the Pt(111) surface. The donut structure is a partially dehydroxylated state between the $(6x6)_{cp}$ and the dehydroxylated, honeycomb-like $(6x6)_{hc}$ structure.
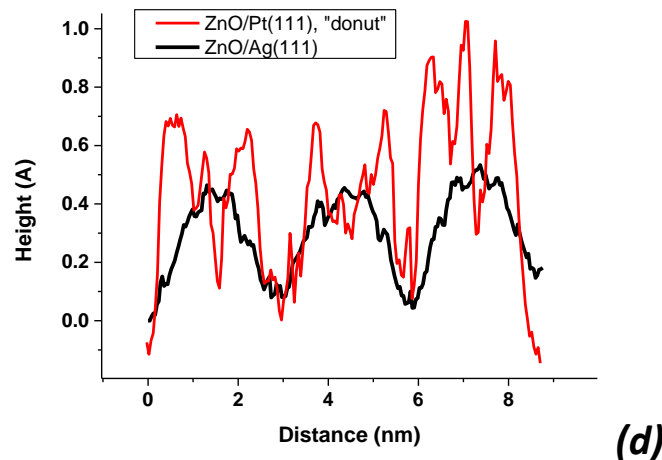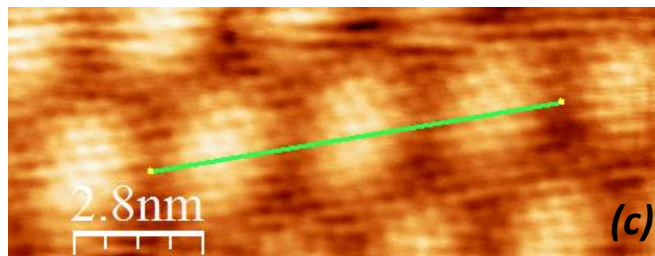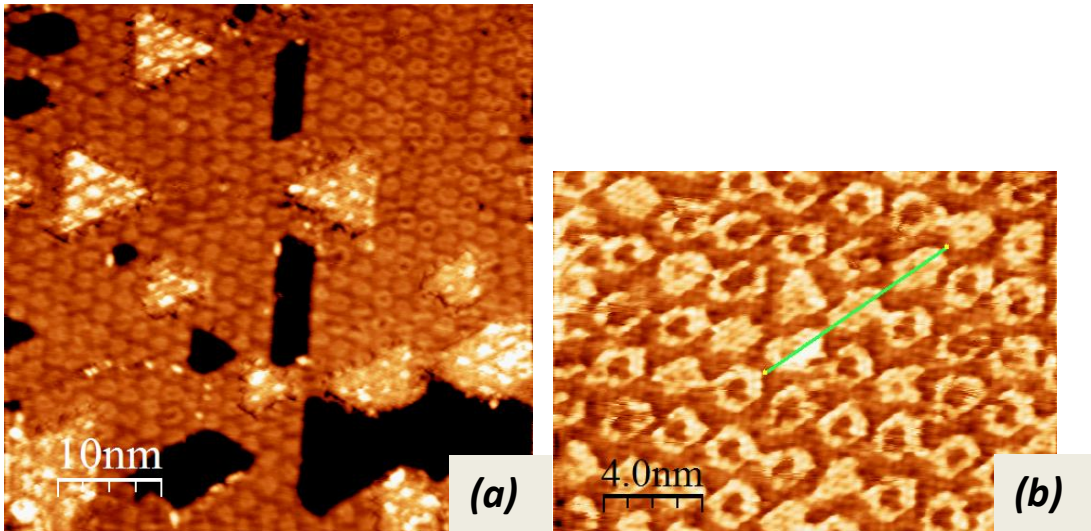
One observation relating to the substrate-induced difference in the film is worth to be pointed out before ending this chapter. Looking at the line profile of the donut structures in Figure 5-6d, the features have sharp edges. These are somewhat similar to those on the monolayer zinc oxide on Pd(111) [77]. This sharp-edged corrugation seems more likely to come from a site specific-adsorbate. This is speculated to be hydroxyls based on the IRAS study on the fully covered monolayer film, which is similar to the donut film in terms of the preparation procedure, film thickness and the periodicity of coincident lattice formed with Pt(111). The films grown on Ag(111) as well as on Au(111)[79, 80], on the other hand, display the Moiré structure with a wavelike modulation, as also shown in Figure 5-6d. This seems more like a continuous corrugation caused by the extent of special overlap between the overlayer and the substrate.

5.3 Summary and conclusions

In this chapter, we addressed the terminations of zinc oxide films; In particular, we focused on whether the prepared films are hydroxylated. Using IRAS, we found that the films grown on Ag(111) are OH-free. In principle, this agrees well with the conclusions previously reported in the literature that ultrathin zinc oxide films are co-planar, like in boron nitride. In contrast, the "as-prepared" films on Pt(111) all expose substantial amounts of hydroxyls. It therefore appears that surface restructuring of otherwise polar, unstable ZnO(0001) surfaces may proceed more efficiently through hydroxylation than relaxation, provided that hydrogen is available in the system. Apparently, Pt readily dissociates H_2, which may provide H atoms to form surface hydroxyls.

The thermal stability of OH species on ZnO/Pt depends on the film thickness: the thicker the film, the more strongly OH is bound. Thermal dehydroxylation of the monolayer film is

accompanied by a certain mass transfer, through which partial film dewetting occurs with concomitant OH spillover onto bilayer islands.

Chapter 6 Structural Diversity of Zinc Oxide Films on Pt(111)

6.1 Transformation of sub-monolayer zinc oxide films

Figure 6-1 shows LEED and STM result of an as-prepared sub-monolayer coverage single layer zinc oxide film on Pt(111) in the (6x6) structure. Very often this film transforms into a honeycomb-like structure, shown in Figure 6-2 after several hours in UHV. According to the LEED analysis, the honeycomb has a (4x4) periodicity with respect to the Pt(111), hence, is noted as the (4x4)$_{hc}$ structure. At first glance, this structure looks very similar to that reported by Weirum et al. [77] on a Pd(111) support, shown in Figure 2-19.
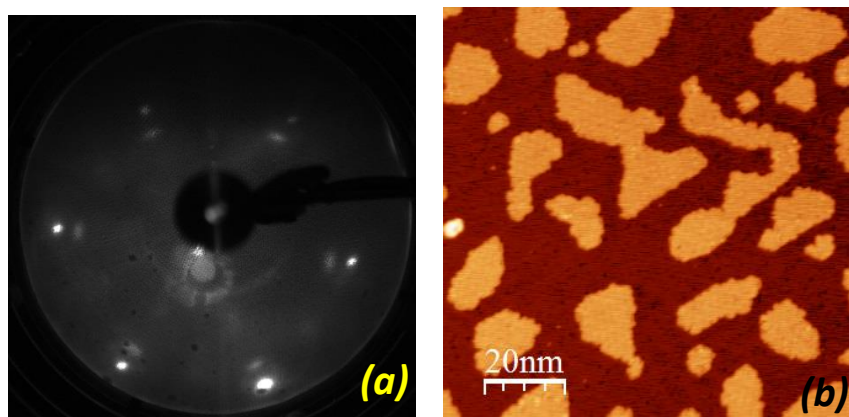
Figure 6-1. Single-layer zinc oxide on Pt(111), the "6x6" structure, at submonolayer coverage. (a) LEED pattern recorded with electron incident energy of 90 eV. (b) STM image, 100 x 100 nm, 1.5 V, 0.7 nA.
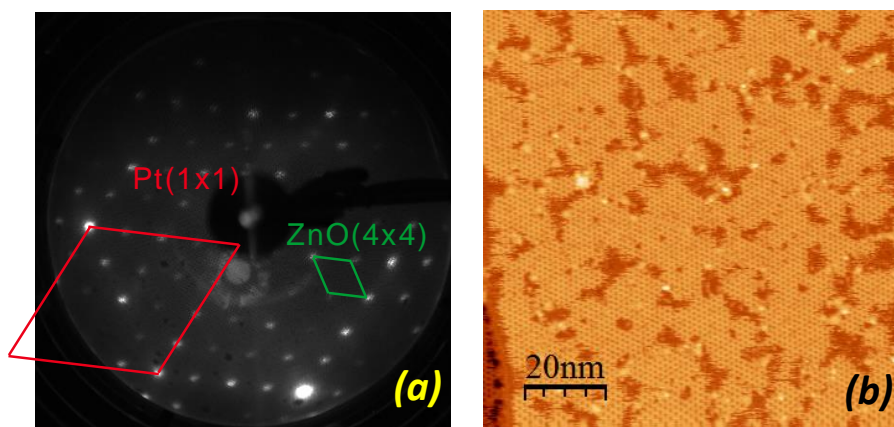
Figure 6-2. The "4x4" honeycomb structure (a) LEED pattern with incident electron energy 90 eV. (b) STM image, 100 x 100 nm, 1.0 V, 1.0 nA

Figure 6-3 collects a series of consecutive STM images that document the $(6x6)_{cp}$ to $(4x4)_{hc}$ transformation. We first note that the surface reconstruction is accompanied by considerable tip instabilities, resulting in streaky images (compare Figure 6-3a to Figure 6-3b). In the initial stage, new features (e.g. marked by black circles in Figure 6-3b) are observed to form preferentially at the island rims, eventually linking adjacent islands. Those features grow in size, and form well-ordered structures with the same periodicity as the 6x6 structure, as shown in the zoomed-in inset Figure 6-3c. (Note again that similar structures were reported for ZnO/Pd(111), which have been attributed to oxygen vacancy ordering within the regular (6x6) structure, thus resulting in a formal stoichiometry of $Zn_{26}O_{25}$). It further expand at the expense of the originally $(6x6)_{cp}$ islands, as shown in Figure 6-3d and e. Concomitantly, small $(4x4)_{hc}$-Pt(111) domains exhibiting an apparent height of $\sim$1.8 Å appear between the islands. The domains coalesce into large areas with enhanced image contrast, as shown in Figure 6-3f, whereas the patches with intermediate structure disappear until nearly the entire surface transforms into the $(4x4)_{hc}$ structure.
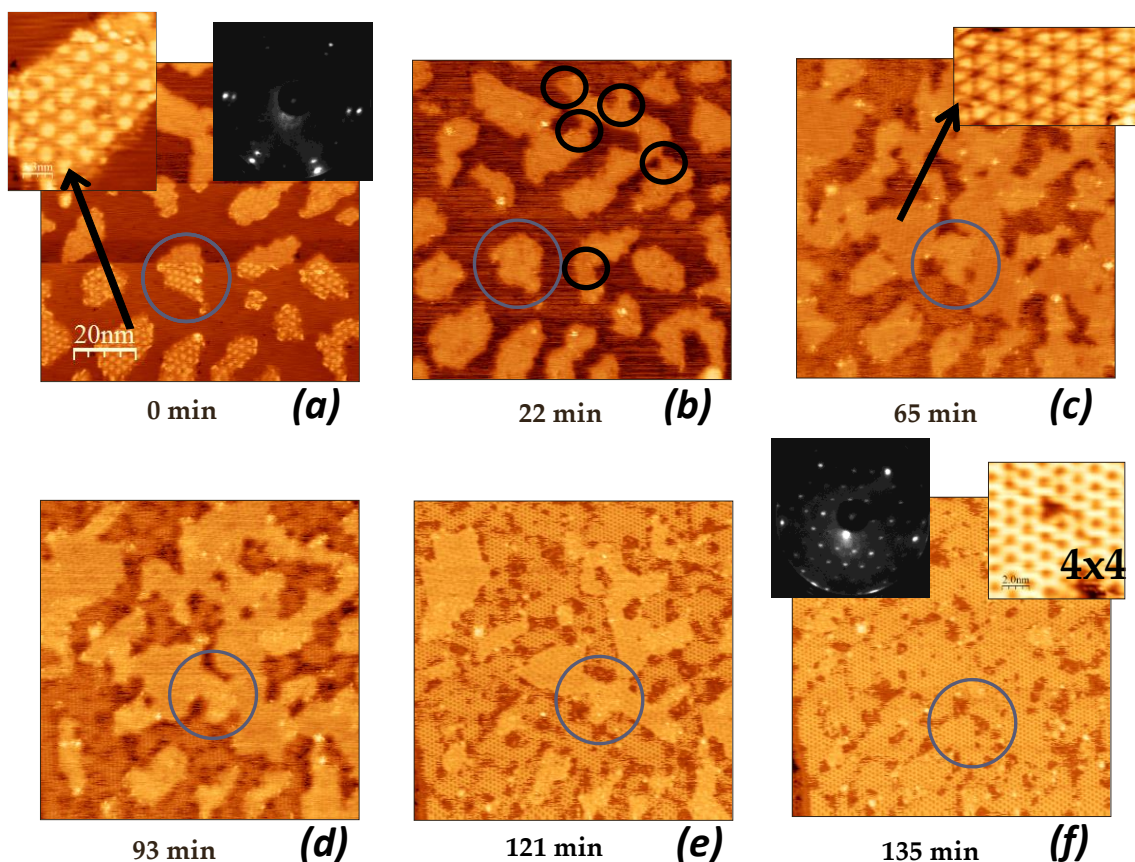
Figure 6-3. The 6x6 to 4x4 honeycomb transformation under the experimental UHV condition. The relative time is indicated under each image. The whole transformation took around two hours, which varies from sample to sample. Due to the thermal drift, the blue circle is placed to mark the same region. Scanning parameter: 100 x 100 nm, 1.0 V, 1.0 nA; 2.84 minutes per frame (scan rate 300 nm/s, 512 line profiles per image). The details are described in the text.

Corresponding Auger spectra did not reveal any considerable (i.e., >10%) differences between the $(6x6)_{cp}$ and $(4x4)_{hc}$ structures, thus indicating that the surface restructuring is not accompanied by substantial compositional changes. Note also that the structural transformation is observed here at room temperature, which is too low for the chemical reduction and/or sublimation of the oxide film in UHV.

Interestingly, the overlayer did not stop changing after the transformation to the $(4x4)_{hc}$ completes. The two STM images in Figure 6-4 are consecutive frames which are separated by about 14 minutes. As highlighted in the red circle, the crack that was observed in Figure 6-4a disappears in Figure 6-4b; the structure highlighted by the black circle in Figure 6-4a breaks up in Figure 6-4b. This shows that the structure is still dynamic.
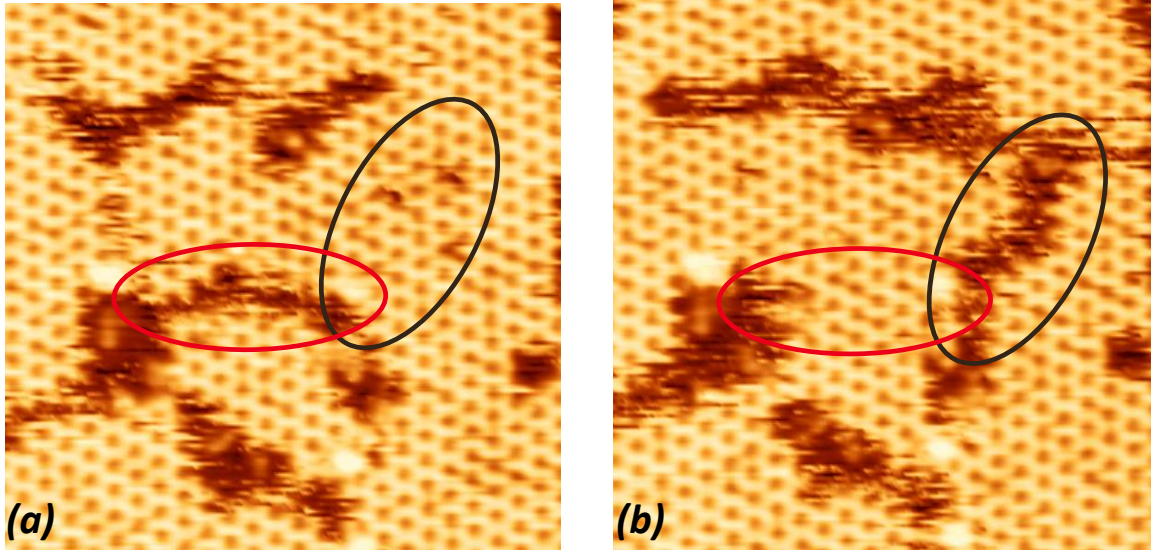
Figure 6-4. The structure kept evolving after the transformation complete. The black ellipse indicates the cracking down of the honeycomb; the red ellipse indicates the formation of honeycomb from a crack. STM tunneling condition: (1.0 V, 1.0 nA).

Further inspection of the surface by STM reveals structural changes within the reconstructed $(4x4)_{hc}$ layer as shown in Figure 6-5. In Figure 6-5a, two $(4x4)_{hc}$ domains meet at a boundary marked by the blue circle. The domain boundary then splits in two (Figure 6-5c) and ultimately disappears as the domains are shifted with respect to each other by half of the $(4x4)_{hc}$ lattice spacing. In addition, "point" defects, seen as triangles in Figure 6-5a and b, eventually form "corners" and "snow-flakes" in Figure 6-5d to f. Such behavior can be described as merging and splitting of $(4x4)_{hc}$ domains like "living cells", which implies a very weak interaction with the Pt(111) surface and high structural flexibility of the domain borders.
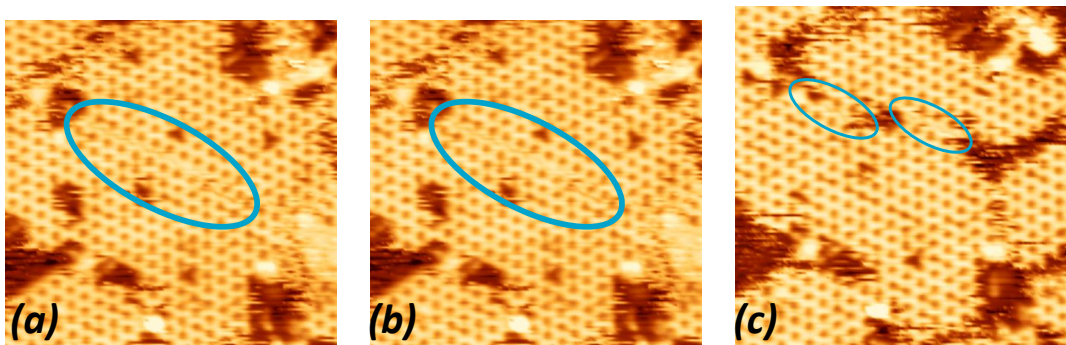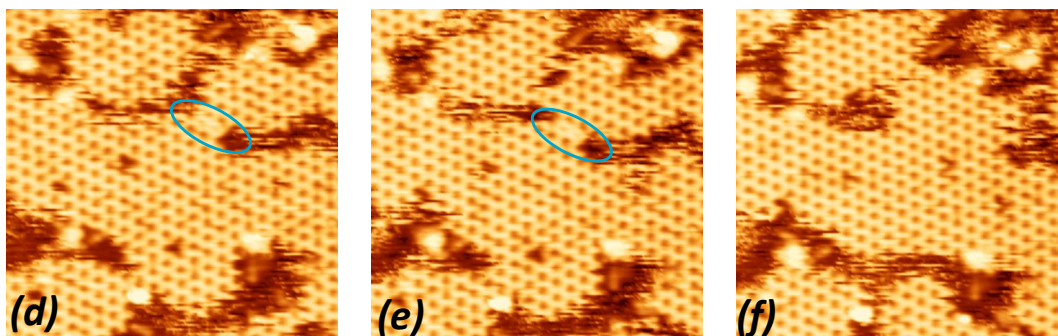
Figure 6-5. The domain boundary of the 4x4 honeycomb, as highlighted in the blue ellipse. The evolution of such a domain boundary is shown from (a) to (f). The time between each frame is about 14 minutes. The boundary disappears in the end. STM tunneling condition: (1.0 V, 1.0 nA).

The STM images presented above show that the $(4x4)_{hc}$ is formed on areas initially uncovered by $(6x6)_{cp}$ islands. This implies the presence of small ZnO_x clusters that migrate across the Pt(111) surface. Such species may also account for the tip instability and streaky STM images shown in Figure 6-3b. It seems plausible that migrating clusters are formed by detachment from the compact $(6x6)_{cp}$ islands, thus giving rise to a two-dimensional gas of adsorbed species, similar to the situation on the coinage metal surfaces where metal adatoms continuously attach to and detach from the terrace step edges (see, for instance, reviews in refs [136] and [137]). Ultimately, the adclusters aggregate into the $(4x4)_{hc}$ structure. Therefore, the whole process seems to proceed via (i) detachment, (ii) diffusion, and (iii) self-assembly of ZnO_x ad-species.

The structural flexibility of the ZnO domain borders, as shown in Figure 6-4 and Figure 6-5 for the $(4x4)_{hc}$ structure, suggests easy breaking and forming of bonds at the rim of islands, which could, in principle, explain the detachment of ZnO_x species as proposed. The diffusion of small ad-species is difficult to address with an STM operated at 300 K. To see whether the $(4x4)_{hc}$ structure is, indeed, the most stable under UHV conditions at room temperature, we examined ZnO films prepared at 300 K. When submonolayer amounts of Zn were deposited onto Pt(111) in 10^{-7} mbar of O_2, aggregates of poorly defined nanoparticles dominated the surface. In contrast, Zn deposition in vacuum onto the oxygen precovered $O(2\times2)$-Pt(111) surface (prepared by oxidation of the clean Pt(111) crystal in $\sim10^{-6}$ mbar of O_2 at 600 K) immediately resulted in the structure, as shown in Figure 6-6. The striking difference between these two films may be explained by the presence of atomic oxygen on Pt(111) in the latter case, which facilitates oxidation of Zn adatoms, whereas the oxidation of a Zn overlayer by ambient

molecular O_2 may be hindered at room temperature. Indeed, using XPS, Deng et al. [80] observed that the reactive deposition of Zn with O_2 at pressures up to 2 x 10^{-6} mbar was unable to fully oxidize Zn supported on Au(111) at 300 K. Therefore, the results indicate that, at low coverage, the $(4x4)_{hc}$ structure on Pt(111) is the most stable one in UHV at 300 K, provided that Zn is fully oxidized. In an oxygen ambient atmosphere and at elevated temperatures (10^{-6} mbar, 600 K as used here), the $(6x6)_{cp}$ structure dominates the surface. The transition between the two structures is fully reversible, thus indicating that both structures are not metastable and/or not formed due to kinetic effects. It should be emphasized that such transformations are found only for single-layer structures. Bilayer (6 × 6) islands, which were observed on as-prepared films in small amounts, remained basically unchanged through the treatments used in the present study.
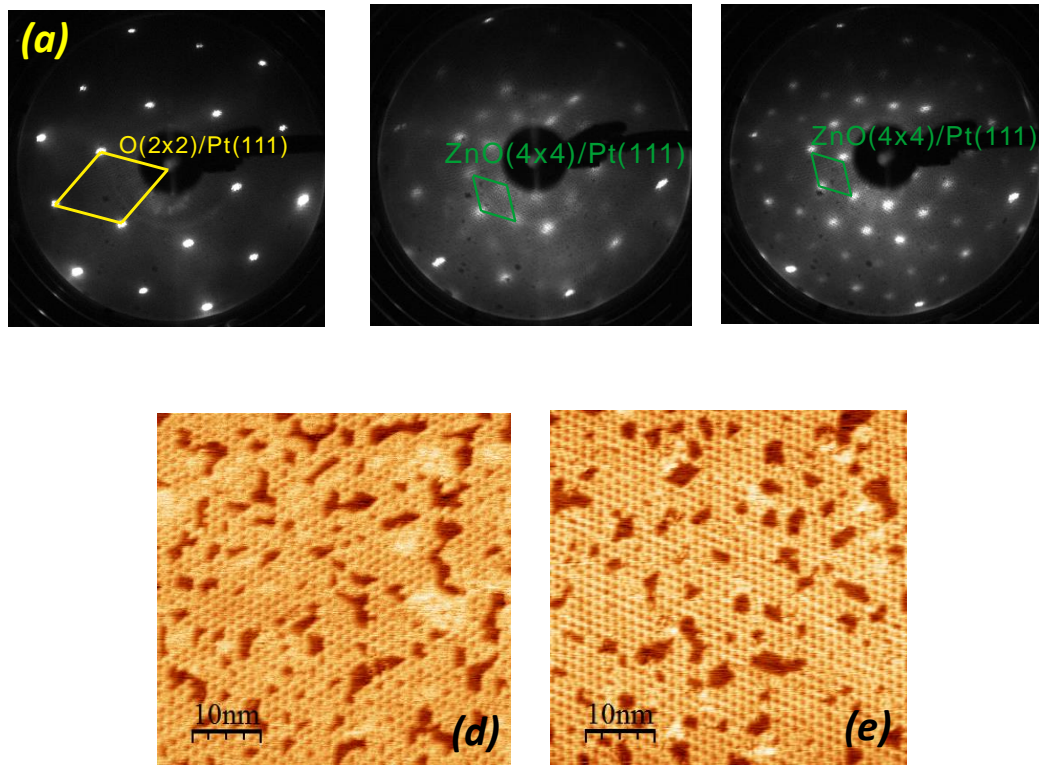
Figure 6-6. The 4x4 honeycomb structure prepared by zinc metal deposition on the O(2x2)-Pt(111) at room temperature. (a) O(2x2)-Pt(111). (b, d) The 4x4 honeycomb prepared by dosing zinc metal on O(2x2)-Pt(111). STM tunneling condition: (1.07 V, 0.5 nA). (c, e) The 4x4 honeycomb placed in UHV overnight. STM tunneling condition: (1.0 V, 0.5 nA). All LEED images are taken with 64 eV incident electron.

The atomic structure of $(4x4)_{hc}$ on Pt(111) is still not understood. However, based on the similarity with that on Pd(111), it could be assumed that its atomic structure is the same as that predicted by DFT in Figure 2-19c, which shows that each side of a hexagon is formed by three

protrusions tentatively assigned to hydroxyls. To test this hypothesis, we measured the IRAS of the film. The spectra in Figure 6-7 show an intense peak at 3600 cm^{-1}, which is characteristic for OH. The peak intensity was doubled as the coverage of the 4x4 structure was doubled. This excludes the possibility that the signal comes from background or other contamination. Based on this result, the atomic structure of the $(4x4)_{hc}$ on Pt(111) is very likely to be $Zn_6(OH)_5$.
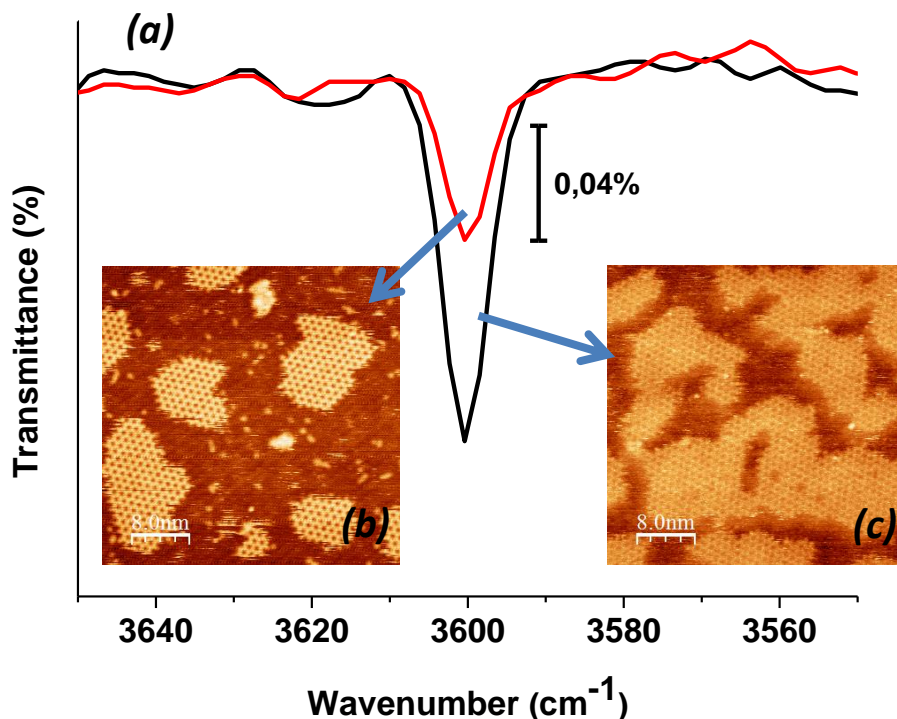
Figure 6-7. (a) IRA spectra of the "4x4 honeycomb" structure in the OH stretching region. As indicated by the arrows, the smaller peak corresponds to the lower coverage film shown in (b); the larger peak to the higher coverage film shown in (c).

The source of the hydrogen remains a question to be answered. It is assumed to be provided by the Pt(111) surface rather than by the gas phase. The analogies of the $(4x4)_{hc}$ structure has not yet been observed on Ag(111) and Au(111) substrates. Apparently, this support effect must be attributed to a much higher affinity of the Pt(111) and Pd(111) surfaces toward H_2 as compared to Ag(111) and Au(111). Since H_2 was not used in the film preparation, we have examined the possible role of the residual gases in UHV on film structures.

In the first set of experiments, the STM chamber was filled by 5 x 10^{-8} mbar of H_2 while scanning the "as prepared" $(6x6)_{cp}$ surface. The results, shown in Figure 6-8, revealed that the $(6x6)_{cp} \rightarrow (4x4)_{hc}$ transformation occurred within a few minutes, much faster than observed under UHV conditions. In another experiment, the (6×6) surface was exposed to 10^{-6} mbar of CO at 300 K for 10 s immediately after the preparation. CO is expected to readily adsorb onto the uncovered patches of the Pt(111) surface. No $(4x4)_{hc}$ was observed by STM and LEED, and subsequent introduction of 5×10^{-8} mbar of H_2 into the chamber could not trigger the transformation either. The latter finding may be explained by CO blocking H_2 dissociation on Pt(111), thus suppressing the promotional effect of H_2.
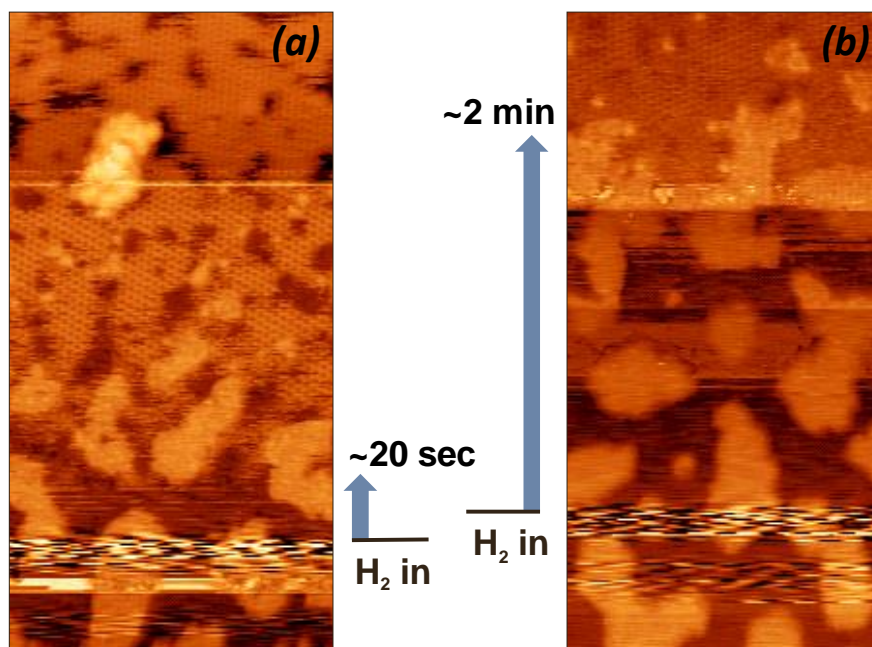
Figure 6-8. H_2-induced 6x6 to 4x4 honeycomb transformation. The vibration in the image indicates the injection of H_2. STM tunneling condition: (1.5 V, 0.5 nA).

Following the line of the experiment, 20 Langmuir of water or deuterium at room temperature were dosed on the submonolayer covered zinc oxide on Ag(111) support. No structural transformation was observed. This finding supports the argument that supports play an important role in the $(6x6)_{cp} \rightarrow (4x4)_{hc}$ transformation.

6.2 Structural variety of monolayer zinc oxide films

As shown in section 5-1, the monolayer zinc oxide film on Pt(111) is hydroxylated. When being heated in UHV, the film is transferred into a $(6 \times 6)_{hc}$ structure, as shown previously in Figure 5-5b, upon losing surface hydroxyls by water desorption. What would happen if the dehydroxylated $(6 \times 6)_{hc}$ surface is exposed to H_2O? Figure 6-9a and b show the STM image and LEED pattern respectively, of the $(6 \times 6)_{hc}$ after dosing 3 L of H_2O. In the STM image, the periodic holes in the $(6 \times 6)_{hc}$ film disappears. It seems more uniform, very similar to the appearance of a $(6 \times 6)_{cp}$ film. The LEED pattern conveys a similar message: the pattern looks almost the same as that of $(6 \times 6)_{cp}$, as shown in Figure 4-2. Both LEED patterns show ZnO(0001) spots, Pt(111) spots, and coincident spots from the ZnO to Pt(111) interface. Putting the observations from STM and LEED together, it seems that the $(6 \times 6)_{hc}$ film is transformed to a $(6 \times 6)_{cp}$ film, by dosing 3 L of H_2O.
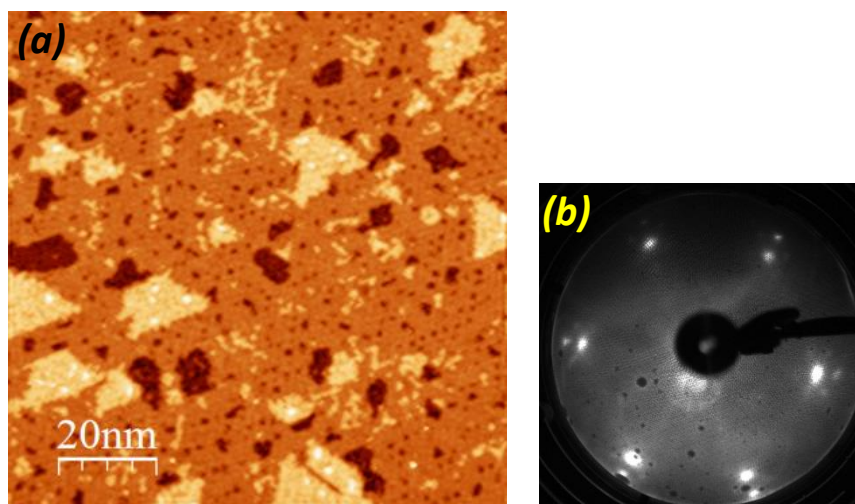
Figure 6-9 STM image and LEED pattern after 3 L H_2O dosed at room temperature on the dehydroxylated monolayer zinc oxide film on Pt(111). (a) STM image with tunneling condition: 2.0 V, 0.5 nA. (b) LEED pattern of 75 eV incident beam.

Further experiments were performed to test this hypothesis. The film shown in Figure 6-9 was annealed in UHV up to 600 K once again. One could expect to see the $(6 \times 6)_{hc}$ structure again, if the hypothesis is true. The annealing procedure was monitored by QMS. The corresponding water TPD is shown in Figure 6-10. As in the case of the water TPD of $(6 \times 6)_{cp}$ film that shown in the inset of Figure 5-5a, the spectrum contains two peaks. However, the higher temperature peak is obviously shifted to lower temperature (526 to 456 K) and the lower temperature peak is shifted to higher temperature (360 to 401 K). It is difficult to assign the

origin of the peaks at this stage; however, it is an indication that the film is somewhat different from the initially $(6x6)_{cp}$. The flashed film was characterized by STM and LEED, as shown in Figure 6-11. The film morphology in STM image seems like a flat layer decorated with scattered islands. Zoom-in image shows that the flat layer is actually some kind of honeycomb structure, which has a periodicity much shorter than the previously observed $(6x6)_{hc}$ and $(4x4)_{hc}$. The LEED pattern also shows a new complex structure, as shown in Figure 6-11b. There are two spots that are close to the Pt(111) spot, which probably come from two different overlayer structures, having similar but not the same periodicity. Groups of three spots located between two Pt(111) spots are eye-catching. Looking more carefully, one might see that the groups actually contain more spots, even though they are dim and difficult to be distinguished; therefore, these spots are marked by dash yellow circle to guide the eyes. Based on the reciprocal lattice length measurement, it can only be concluded that this structure has a (2x2) registry with respect to one of the two overlayer structures that has similar periodicity to Pt(111). This new honeycomb structure is named as $(2x2)_{hc}$.
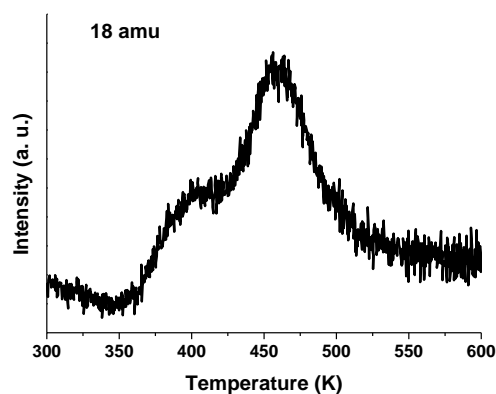
Figure 6-10. 18 amu TPD spectrum of the water dosed $(6x6)_{hc}$ film. Two peaks appear at 401 K and 456 K, respectively.
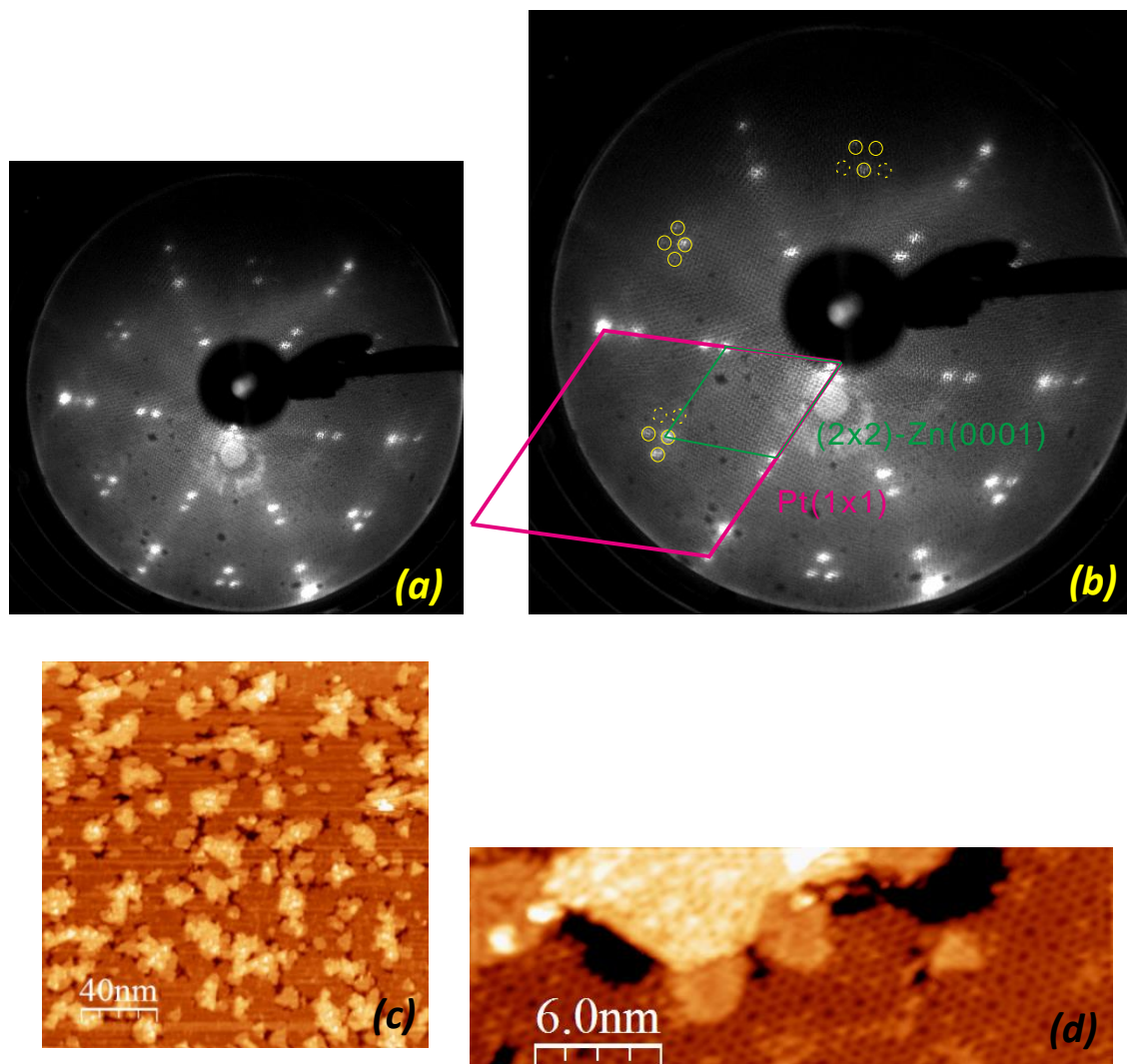
Figure 6-11. The (2x2)$_{hc}$ decorated with islands. (a) LEED pattern of 75 eV incident beam. (b) A duplicate of (a) with assigned reciprocal lattice and highlights of Moiré spots. Dash circle indicates the spots that are not fully certain. (c) STM image, tunneling condition: 2.0 V, 0.5 nA. (d) Zoom-in of the (2x2)$_{hc}$, STM tunneling condition: 0.12 V, 0.5 nA

Further attempts have been made to extract more structural information of the (2x2)$_{hc}$ from the LEED pattern. The group of the LEED spots that corresponds to the (2x2)$_{hc}$ seems very much like a set of Moiré pattern that encodes the relative periodicity of two adjacent epitaxial layers. By measuring the distance between spots and compare it to that of the Pt(111) spots, one can know that the coincident lattice which forms the Moiré pattern has a periodicity between 30 and 45 Å. The large uncertainty comes from the error when gauging the reciprocal

lattice length. It is a considerable percentage to the reciprocal lattice length, which is less than one centimeter on the LEED screen. This uncertainty, unfortunately, impedes the attempt to gain more detail of the $(2x2)_{hc}$ structure.

Extended two dimensional honeycomb structures are not uncommon in surface science. A famous example is the single-layer carbon honeycomb structure, or graphene, consisting of a network of sp^2 carbon atoms [138]. Examples of similar bicomponent structures are boron nitride (BN) [139] and silicon carbide (SiC) [140]. Recently, two-dimensional silicon-containing ring structures were discovered on metal supports. Examples are silicon oxide (silica) [141] and zeolite (aluminium silicate) [142].

AES characterization was performed to investigate the chemical composition of the $(2x2)_{hc}$. It was shown that the ratio of Auger electron intensity between zinc (994 eV) and oxygen (512 eV) is around 1:5, which is similar to that of other dense zinc oxide films. Based on this, the chemical composition of the $(2x2)_{hc}$ can be concluded as some kind of oxidized zinc. The possibility of zinc oxide being reduced to zinc metal can be excluded.

Two-dimensional crystal defects induce property changes in the same way that three-dimensional crystal defects do. In the case of graphene and carbon nanotubes, the common point defects are Stone-Wales defects and missing atoms. These defects affect both their adsorption [143] and chemical properties [144, 145]. An electronic property change is reported with the introduction of a single vacancy on graphene[146], as revealed by STM. The mechanical property of carbon nanotubes is also affected by defects [147, 148]. In graphene the ring size variation defects were shown to be accompanied by vertical buckling of the structure [149]. This implies that the defect not only changes the planar structure as can be obviously observed in STM, but also affected the vertical structure.

Looking in more detail at the $(2x2)_{hc}$ structure, one can see there are numerous defects spread over the film. They could be roughly classified in two types that are observed in graphene: the ring size variation and the single or multiple vacancies. As shown in Figure 6-12a, besides the majority of hexagonal rings, some seven-membered rings (heptagon) and five-membered rings (pentagon) are also scattered over the surface. See the region marked by green circle as an example. These heptagons and pentagons are very often adjacent to each other, appearing in pairs. This arrangement could reduce the tension stemming from angular distortion,

which comes from the ring size variation. One thing worth mentioning is that, throughout the images presented here, there are no 5-7 ring arrangements that generates a Stone-Wales defect, even though the Stone-Wales defect is a common defect in graphene and carbon nanotubes, and is also recently being observed on a copper oxide film on Cu(111) support [150]. The other kind of defect is called vacancy. As indicated in Figure 6-12c and d, some building block of the honeycomb is missing, resulting in a larger ring with presumably dangling bonds pointing towards the ring.
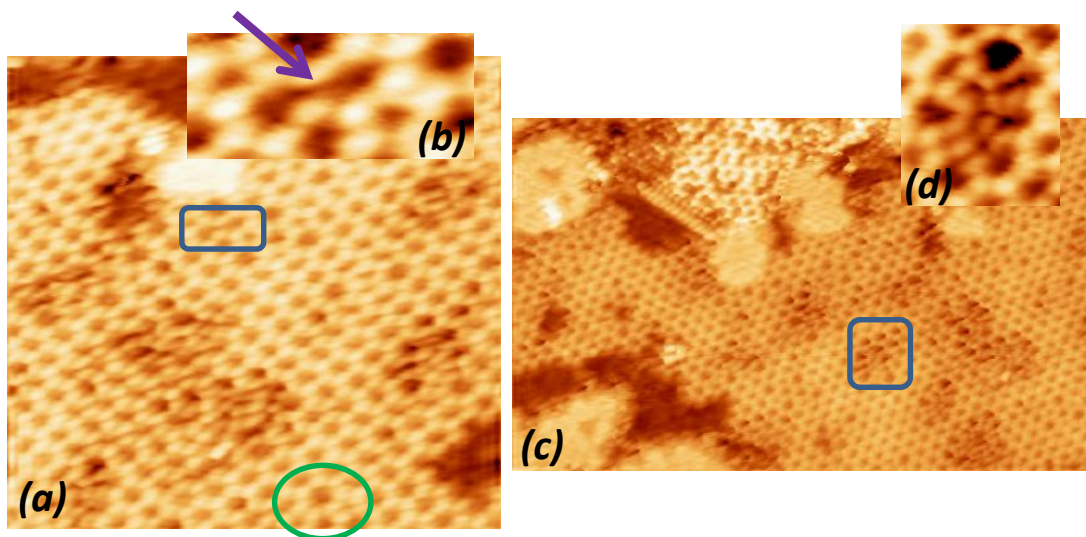
Figure 6-12. Zoom-in STM images of (2x2)$_{hc}$ structure. Tunneling condition: (a, b) (0.11V, 0.5nA); (c, d) (0.12V, 0.5nA).

Also shown in Figure 6-12b is a depression between two protrusions, as indicated by the purple arrow. This is also a defect since it is different from the general structure; however, it does not belong to the abovementioned defects. The two rings adjacent to this indentation are both heptagonal, with six protruding spots on each. This type of defect seems to come from the missing atom, which does not contribute a bright spot in the STM image. To clarify, assuming the protrusion in the image come from oxygen, then the indentation in this image is from the missing zinc, or vice versa. Zooming in to one of the depressed structures, as shown in Figure 6-12d, one can see that the bridges between the central bright spot and its surroundings are all gone. This shows that collapsed structures consisting of partially broken honeycombs could result from the loss of a bridging atom of the normal honeycomb.

Based on the existing experimental data, an exact atomic structure cannot be concluded. DFT calculation would be a big help to establish an atomic model. In addition, to better study the layer structure along the surface normal, other techniques, such as helium ion scattering spectroscopy, electron energy loss spectroscopy, X-ray standing wave and surface X-ray diffraction, would provide useful information.

Aside from the extended $(2\times2)_{hc}$ structure, there are some islands scatted throughout the surface. The atomically resolved image of the island is shown in Figure 6-12c. One can see that on top of the island the pattern seems to resemble the $(2\times2)_{hc}$ structure, even though the vacancy defects are extremely dense, such that one could not even refer to them as defects anymore. The island is terminated with an ordered one-dimensional row structure at the edge.

Noteworthily, an alternative way to prepare the $(2\times2)_{hc}$ film is by flashing the $(4\times4)_{hc}$ film to 600 K. A separated experiment done in another chamber, which is equipped with IRAS, showed that the hydroxyls on the $(4\times4)_{hc}$ disappear after the sample was annealed to 600 K, as shown in Figure 6-13. This suggested that the $(2\times2)_{hc}$ structure is a hydroxyl-free structure. Unlike most of the zinc oxide structures on the Pt(111) support, the $(2\times2)_{hc}$ is one of the two "dehydrated" structures observed on Pt(111) in this work. It is not a stable structure, however. The $(2\times2)_{hc}$ film, when being placed in UHV chamber for a while under a background pressure lower than 1×10^{-9} mbar, transfers to an unresolved structure, which produces a complex LEED pattern shown in Figure 6-14. It could be speculated that the transformation is due to its sensitivity to residual H_2O or H_2 in the background.
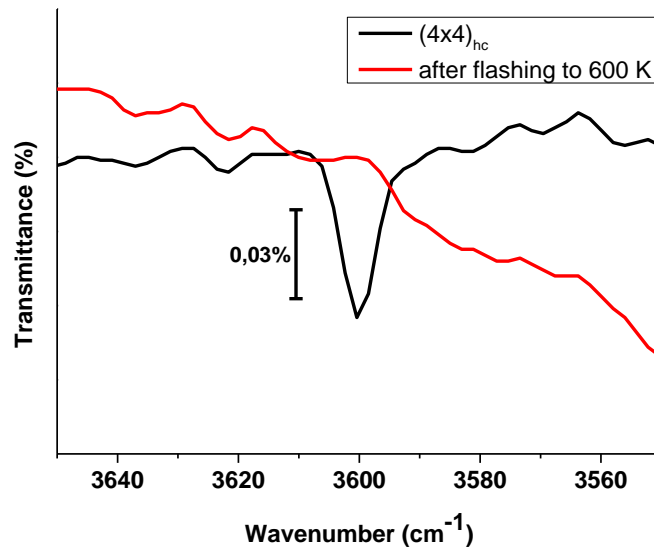
Figure 6-13. IRAS of (4x4)$_{hc}$ structure. (blue: before flashing to 600 K; red: after flashing to 600 K).
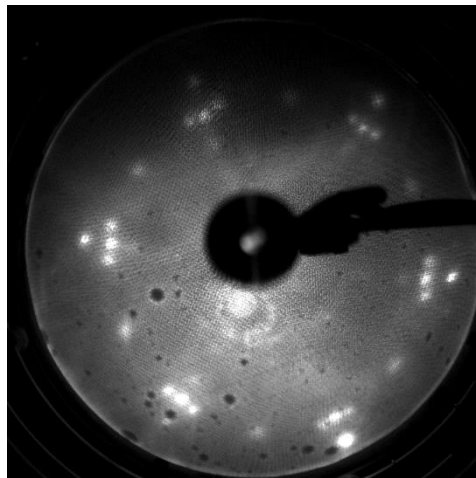
Figure 6-14. LEED pattern of the film, produced from the (2x2)$_{hc}$ film after placing in the UHV chamber for 1.5 days. Incident electron energy 75 eV.

The (6x6)$_{hc}$ transferred into a variety of structures upon dosing 0.5 L water, as shown in Figure 6-15. Despite the different appearance in the STM, all the structures share the same periodicity of 16.6 Å, which is deduced from the LEED. As already discussed in section 4-1, the periodicity comes from the lattice mismatch of the zinc oxide with the Pt(111) substrate, as the periodicity already appears in the as-prepared film before any treatment. Apart from this, the

detailed atomic structure could not be resolved without additional information, such as DFT calculation. Even though the atomic model of these structures is not clear, the rich phase diagram is in line with the structural variety observed in the zinc oxide nano-objects. As a consequence, when establishing a structure-reactivity relationship of zinc oxide based catalyst, the structural variety should be taken into account. Reaction schemes based on single spiecies might be oversimplified.
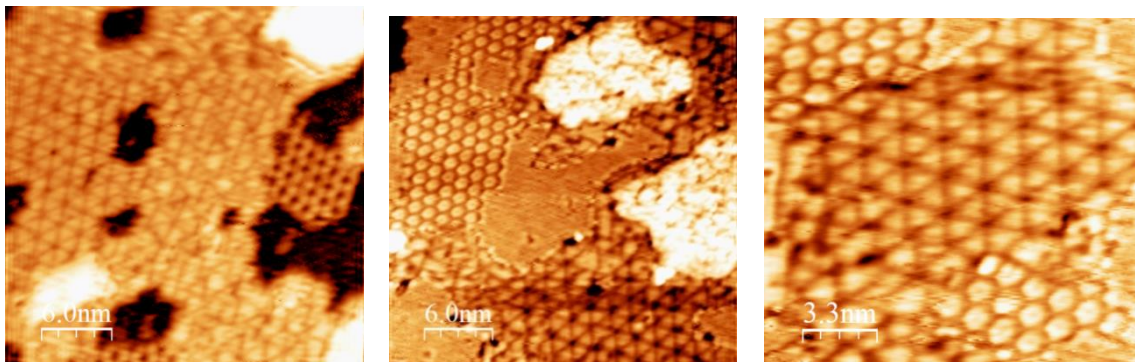
Figure 6-15. Gallery of structures formed by dosing 0.5 L H_2O on dehydrated zinc oxide on Pt(111).

6.3 Summary and conclusions

This chapter focused on the morphology of zinc oxide films on Pt(111) in different exposure conditions. At sub-monolayer coverage, the monolayer islands may readily transform into the (4x4)$_{hc}$ structure even at room temperature. The transformations are more facile in H_2 environment, and are accompanied by substantial mass transport across the surface, indicating the presence of Zn-containing mobile species. Such a behavior is observed neither on Ag(111) nor on Cu(111), thus supporting the conclusions on the critical role of a Pt(111) support in the film growth and stabilization. All structures on Pt(111) reported in this thesis are hydroxylated. The dehydroxylated structures, which were observed upon UHV annealing, are either unstable in UHV condition or very sensitive to water. It can therefore be concluded that hydroxyl groups play a crucial role for the observed zinc oxide structures and stabilizing the zinc oxide structures on Pt(111).

Chapter 7 Structural Aspects of Reactivity of Zinc Oxide Films in CO Oxidation

Low-temperature CO oxidation reaction is a common test reaction in surface science [151]. The zinc oxide overlayer on Pt(111) showed enhancement of CO oxidation reactivity at near-atmospheric pressures [152]. The reactivity measurements were performed in an excess of oxygen in order to prevent possible oxide film reduction and dewetting. With zinc oxide overlayer, the reactivity of the system is enhanced significantly at submonolayer regime, as shown in Figure 7-1a. The study of the thickness dependency of the film is feasible, thanks to the layer-by-layer growth mode of the zinc oxide overlayer on Pt(111) discussed in chapter 4. The CO_2 production rate dependency on the film thickness measured prior to the reaction is plotted in Figure 7-1b. The reaction rate is enhanced by the presence of zinc oxide. The enhancement is maximized at the submonolayer coverage regime. The reactivity disappears when the film is thicker than 2 MLE.
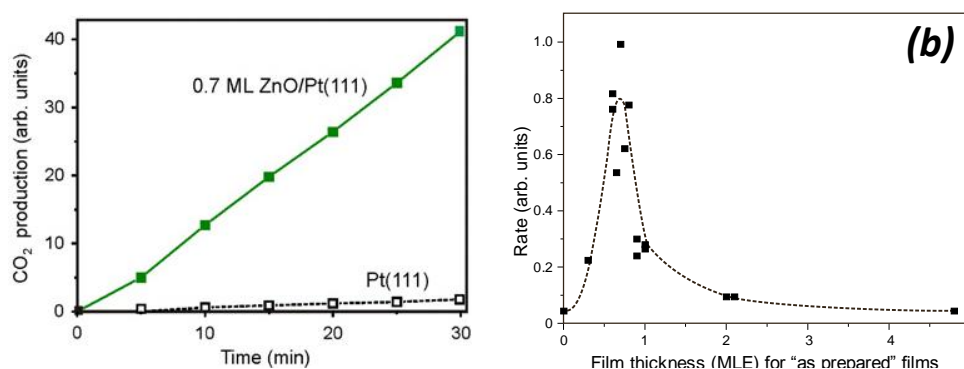
Figure 7-1. (a) The CO_2 production rate of 0.7 ML zinc oxide film on Pt(111) support through low-temperature CO oxidation reaction. Reaction condition: 10 mbar CO + 50 mbar O_2 balanced to 1 bar by He; temperature 450 K. (b) The thickness dependence of the low temperature CO oxidation reaction catalyzed by zinc oxide on Pt(111). Experiment conducted by Dr. Yulia Martynova.

The morphology of the spent catalyst was characterized by STM *ex situ*. The step height measurement indicates that the height of the islands in all submonolayer films increases from 2.2 Å to around 4 Å. This indicates that the monolayer films transformed to bilayer thickness. On the other hand, the zinc oxide film became partially dewetted after the reaction condition treatment: the coverage of 0.25 MLE film reduced to 0.18 MLE (72 %); that of the 0.55MLE film

to 0.32 MLE (58 %); and that of the 1.2 MLE to 0.75 MLE (63 %). The coverage of the spent catalyst might be overestimated due to the tip convolution effect for small objects in STM. Therefore, it could be concluded that the coverages after exposure to the reaction condition reduced to about one half of the original film. Once again, this indicates that the film transferred to bilayer structure. The surface of these reacted films is rough, and the Moiré superstructure disappears. This agrees well with the LEED patterns in Figure 7-2. Notably, the spent catalyst becomes more ordered after annealing at 600 K in 2×10^{-6} mbar O_2 for 20 minutes: the Moiré structure reappears on the surface in STM images, yet the layer structure remains bilayer, decorated with the island of the third layer. An example is shown in Figure 7-3.
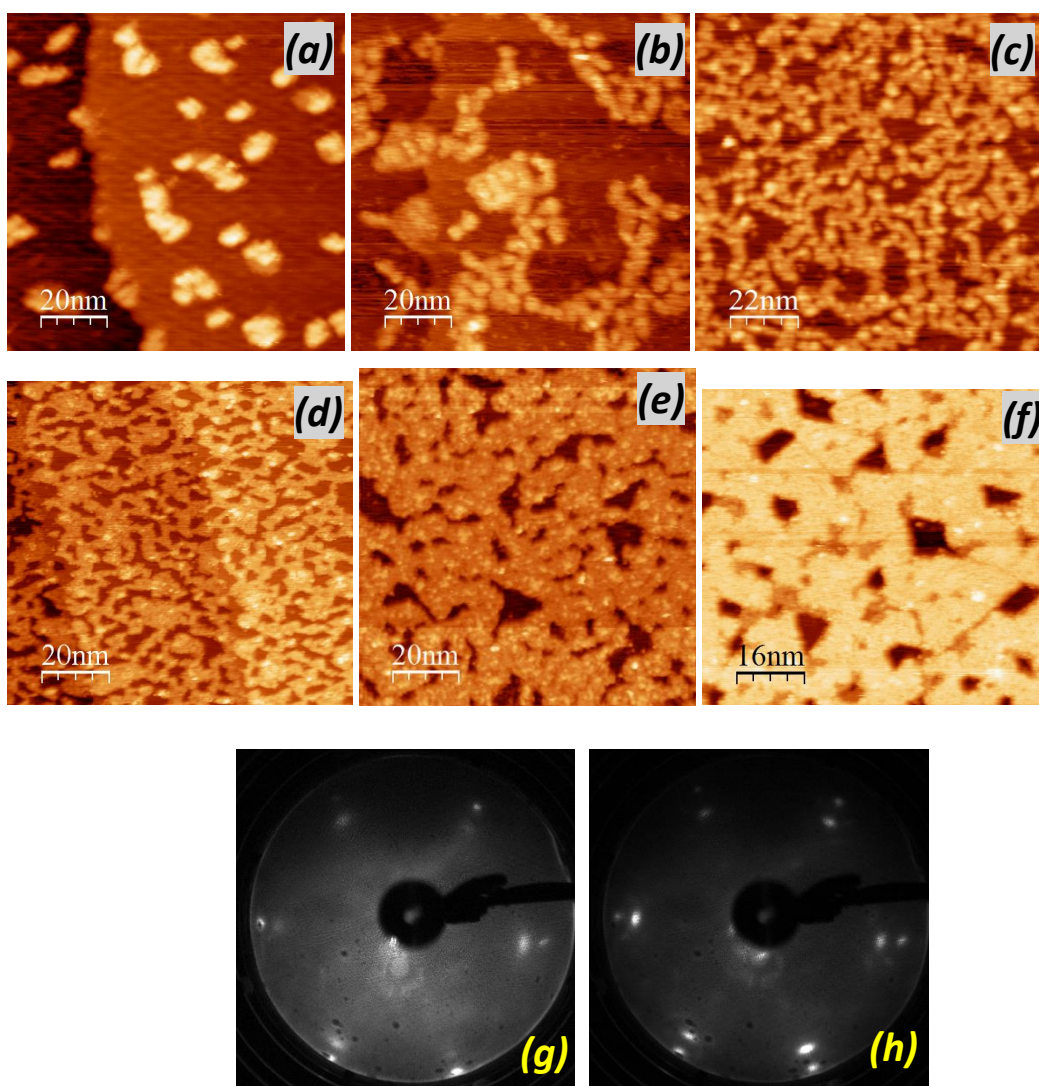
Figure 7-2. STM and LEED of the "spent" catalyst. STM: (a) 0.2 ML, 1.0 V, 0.7 nA; (b) 0.6 ML, 1.5 V, 1.5 nA; (c) 0.8 ML, 1.2 V, 0.7 nA; (d) 1.2 ML, 1.5 V, 0.3 nA; (e) 1.8 ML, 2.0 V, 0.4 nA; (f) >5 ML, 1.5 V, 0.6 nA; (g) LEED pattern of the 0.8
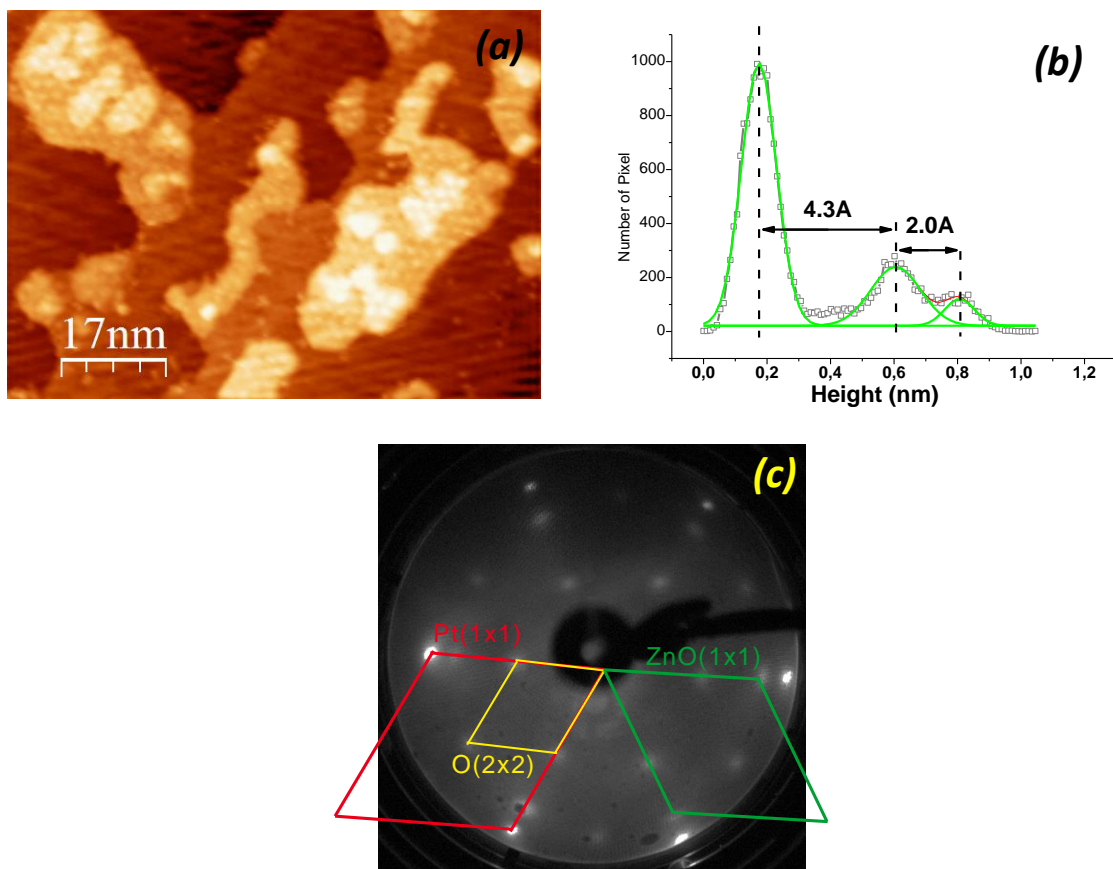
Figure 7-3. STM and LEED of the "spent" catalyst after annealing in O_2 at 600 K for 20 minute. (a) STM image 3.0 V, 0.8 nA. (b) The histogram shows that the step heights are 4.3 Å and 2.0 Å for the first and second step, respectively. (c) LEED image taken by 64 eV incident electron. The (2x2)/Pt(111) registry represents the oxygen atom on the base Pt(111) surface.

The coexistence of the zinc oxide overlayer and the Pt(111) substrate seems crucial for the reaction. Neither the bare Pt(111) nor the fully covered thick zinc oxide layer shows significant reactivity. The rate enhancement of the partially oxide-covered metal surface is commonly attributed to that the reaction happening at the metal/oxide boundary, which has been studied on so-called inverse model catalyst [153, 154]. In order to test this hypothesis, the perimeter length of the islands is measured and compared with the reactivity. In Figure 7-4, the plot shows the perimeter length of the islands per unit area with respect to the coverage, from

the film after the reaction treatment. It can be seen that the trend shows a fairly good correlation to the reactivity shown in Figure 7-1b, although the exact position of the maximum deviates. This could be due to the fact that the STM measurements were conducted *ex situ* in another experimental setup. The correlation suggests that the reaction happens at the metal/oxide boundary. This metal oxide synergy effect may result from the formation of a highly active site at the metal/oxide boundary.
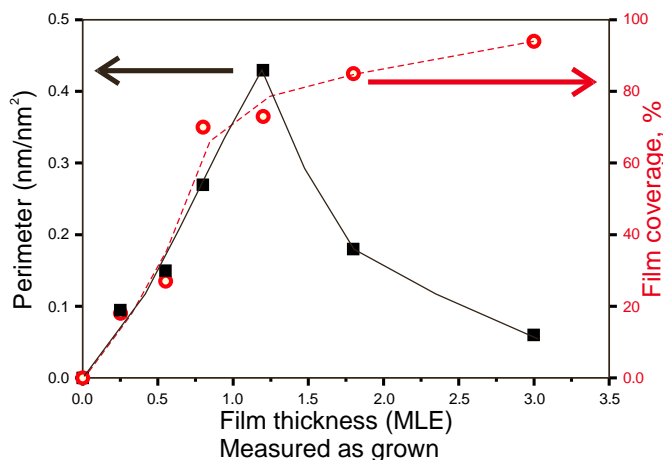
Figure 7-4 The perimeter length per unit area of the "spent" zinc oxide film on Pt(111). The maximum appears at around 1 monolayer.

For the zinc oxide film on Ag(111) and Cu(111) supports [155], the reactivity tests were done by Dr. Qiushi Pan, and no enhancement was observed; conversely, the zinc oxide films somewhat inhibit the catalytic reactivity of the pure supports (see Figure 7-5).
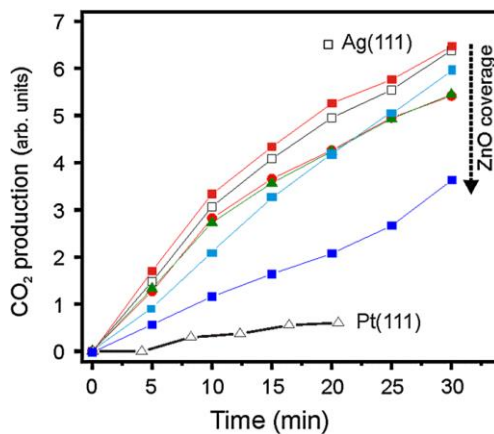
The structure of zinc oxide on Ag(111) basically does not change upon exposure to the reaction condition. Upon exposure to diluted reaction mixture (1 mbar CO + 5 mbar O_2) and heated up to 500 K, as depicted in Figure 7-6, the AES shows no significant change; the STM shows that the film retained the planar structure. The intensity of the Ag spots and ZnO spots in LEED remain at a similar level, indicating that overlayer still follows the registry defined by the substrate. These observations point to the conclusion that the film structure remains basically unchanged upon exposure to reaction condition, although it seems to be slightly contaminated. The reactivity chart in Figure 7-5 shows that the zinc oxide overlayers suppress the reactivity. The data are too scattered to draw a coverage-dependent relation. Therefore, it appears that the reactivity depends on the precise morphology of system.
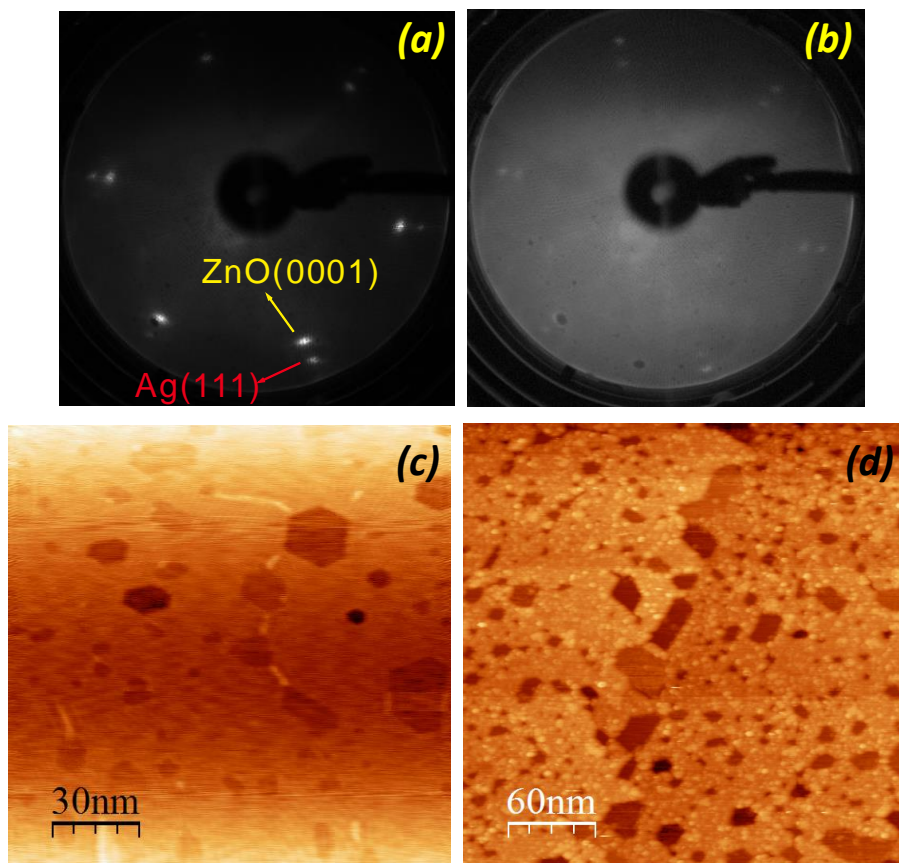
AES	Zn(994)/Ag(301)	O(512)/Ag(301)	Ag(266)/Ag(301)
Clean Ag(111)	-	-	56.9
ZnO as prepared	2.4	9.8	54.3
Reaction treatment	2.1	9.6	64.9

Figure 7-6. LEED, STM and AES of the zinc oxide film on Ag(111). (a, c) As prepared. (b, d) After exposure to 1 mbar CO + 5 mbar of O_2 at 450 K for 10 minutes. (a, b) Incident electron energy 64 eV. (c) 1.5 V, 0.6 nA. (d) 2.5 V, 1.5 nA. The Ag(266)/Ag(301) ratio serves as an indication to the amount of carbon, whose peak in AES is at 272 eV and overlaps with Ag(226).

Same set of experiments were done on Cu(111). The presence of zinc oxide overlayer shows no promotional effect. As shown in Figure 7-7, for the 0.4 MLE zinc oxide-covered Cu(111), the CO_2 production rate is similar to the pristine surface; the 0.9 MLE coverage results in reduced reactivity. In Figure 7-8, post-characterization of the spent catalyst by AES showed no identifiable zinc signal. Since the decomposition temperature of zinc oxide films are around 900 K [152], it is safe to assume that the zinc diffused into the copper substrate rather than sublimating to the vacuum. Estimating from the mean free path of the zinc 994 eV Auger electron, there is no zinc within 3 nm of the surface. STM images of the bare Cu(111) and Cu(111) supported zinc oxide films are very similar after treated in the same condition as in the reactivity tests. It seems that when the zinc oxide film exceeds a certain amount, it suppresses the active element in the model catalyst.
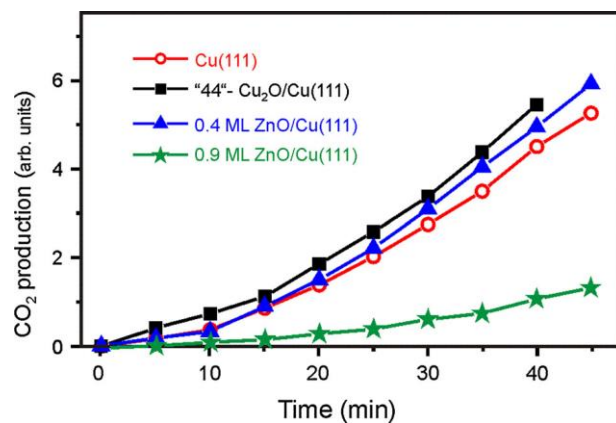
Figure 7-7 CO$_2$ production rate through low-temperature CO oxidation reaction on different amount of zinc oxide supported Cu(111). Reaction condition: 10 mbar CO + 50 mbar O$_2$ balanced to 1 bar by He; temperature 450 K. Experiment conducted by Dr. Qiushi Pan.

(e)

(f)
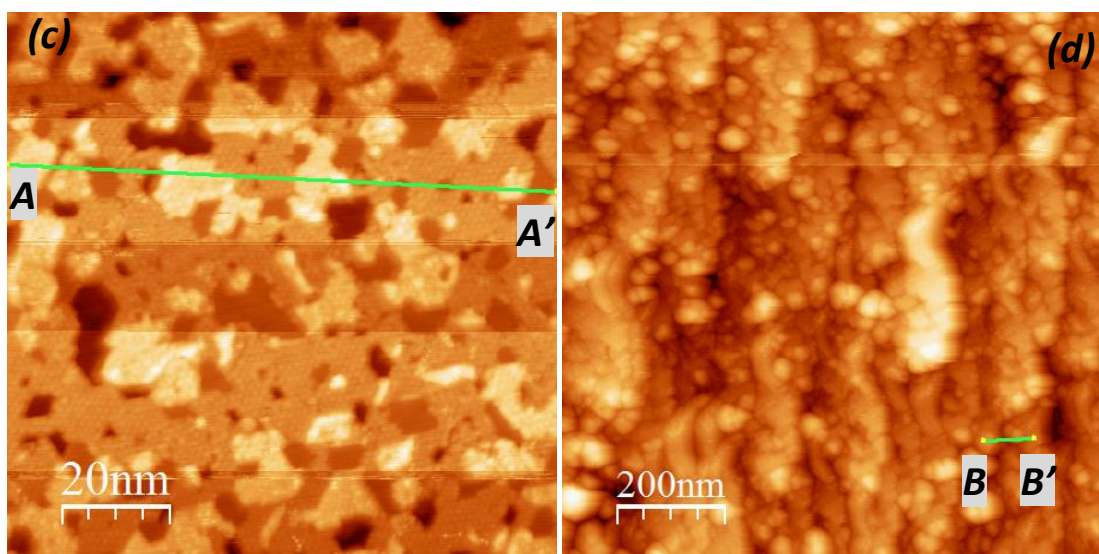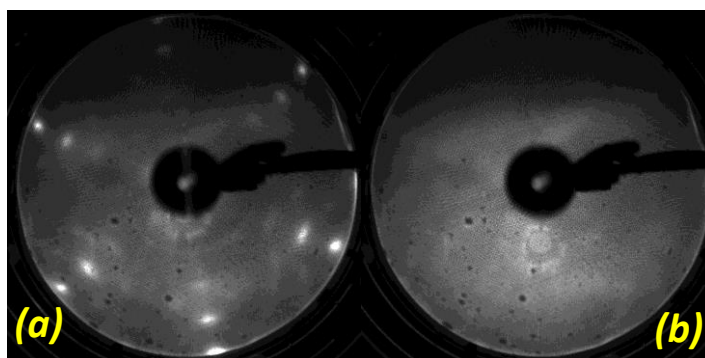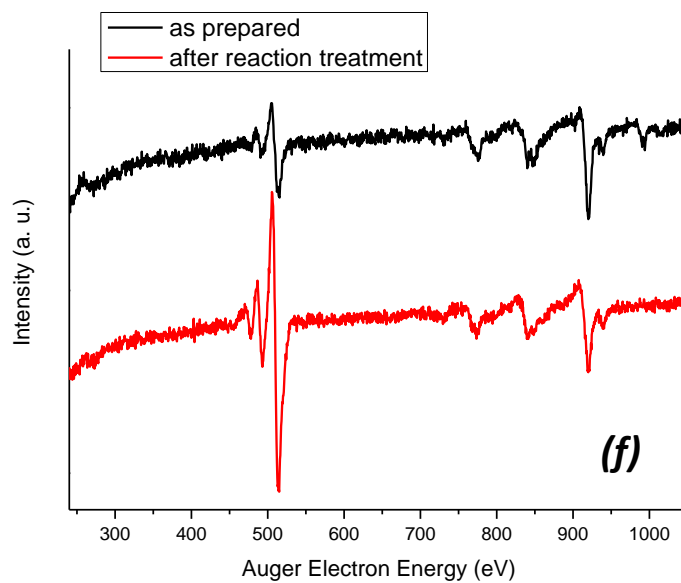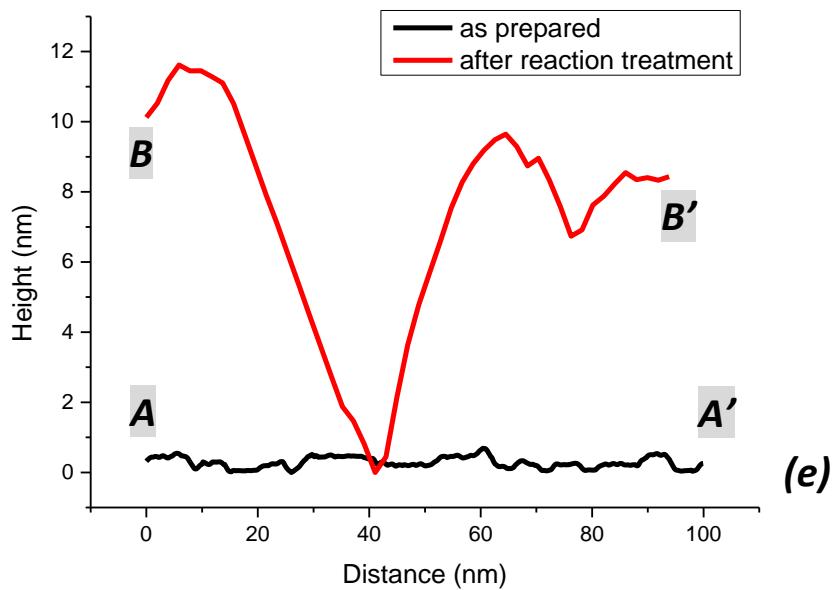
AES	Cu(920) intensity (a.u.)	O(512)/Cu(920)	Zn(994)/Cu(920)
ZnO as prepared	0.15	0.83	0.24
Reaction treatment	0.13	3.25	-

Figure 7-8. LEED, STM and AES of the zinc oxide film on Cu(111). (a, c) As prepared; (b, d) after exposure to 10 mbar CO + 50 mbar of O_2 balanced to 1 bar by He at 450 K for 10 minutes. The surface roughness is indicated by the scale bars of the line profiles of the STM images. (a, b) Incident electron energy 64 eV. (c) 1.5 V, 0.6 nA; (d) 2.5 V, 1.5 nA. Both LEED pattern are taken by 64 eV incident electron; both STM image are taken by the tunneling condition 1 V, 1 nA. (e) Line profiles from the STM images (c) and (d). (f) AES of the as-prepared film and the film after the reaction treatment, notice the increase of oxygen (512 eV) and disappearance of zinc (994 eV).

Summary and conclusions

Closed ZnO films on Pt(111) were found to be inactive in CO oxidation at near-atmospheric pressures. If sub-monolayer coverages are considered, the system showed considerable activity. This chapter addressed morphological aspects of model catalysts under reaction conditions. It is found that initially monolayer zinc oxide structures are transformed into a bilayer structure. Correlation between reactivity and perimeter length provided compelling evidence that CO oxidation primarily occurs on the oxide/metal interface. On the Ag(111), the presence of zinc oxide overlayer suppresses the reactivity of Ag. STM results indicate that ZnO probably blocks the active sites. On the Cu(111), the zinc oxide film intermixes with the support under reaction conditions, resulting in rough and poorly defined surfaces, mainly exposing Cu (sub-)oxides.

Conclusions

The presented work addresses the preparation and atomic structure of ultrathin zinc oxide films on metal single crystal supports, namely Pt(111), Ag(111) and Cu(111). Besides the general interest in ultrathin oxide films as two-dimensional systems, interest in ZnO films has recently been reinforced due to the observation of interlayer structural relaxations resulting in graphene-like structures.

We first developed the fabrication of well-ordered ultrathin zinc oxide films on three metal supports using Zn physical vapor deposition. On all substrates, the film grows in [0001] orientation. On Pt(111), the film grows in a layer-by-layer mode, starting from a monolayer, and ultimately reaching surface structures characteristic for ZnO(0001) single crystal surfaces. On Ag(111), the alloying of zinc and silver made it necessary to deposit Zn in relatively high O_2 pressures. The resulting films form bilayer structures (i.e., two ZnO sheets) from the onset. Further growth to obtain multilayer films turned out to be very difficult, indicating some sort of "self-limiting" growth. The latter behavior is observed on a Cu(111) substrate as well. Since the Cu surface has relatively high affinity for oxygen, the ZnO films on Cu(111) are more complex in structure when compared to the films grown on Pt(111) and Ag(111), in particular at sub-monolayer oxide coverages.

The termination of the zinc oxide films was addressed using IRAS to monitor hydroxyl species. In contrast to the films grown on Ag(111), all films on Pt(111) reveal substantial amounts of hydroxyls. It therefore appears that surface restructuring of otherwise polar unstable ZnO(0001) surfaces may proceed more efficiently through hydroxylation than relaxation, provided that H atoms are available in the system. It seems that Pt readily dissociates H_2 and provides H atoms to form surface hydroxyls.

The thermal stability of OH species on ZnO/Pt depends on film thickness: the thicker the film, the more strongly the OH is bound. Thermal dehydroxylation of the monolayer film is accompanied by a certain mass transfer, by which partial film dewetting occurs with concomitant OH spillover onto bilayer islands.

Zinc oxide films on Pt(111) are found to exhibit a very rich structural variety, depending on exposure conditions. At sub-monolayer coverage, the $(6\times6)_{cp}$ islands readily transforms into

the (4x4)$_{hc}$ structure even at room temperature. The transformations are more facile in H$_2$ ambient, and are accompanied by substantial mass transport across the surface, indicating the presence of Zn-containing mobile species. Such a behavior is not observed on either Ag(111) or Cu(111), thus supporting the conclusions about the critical role of a "more reactive" Pt surface in film growth and stabilization.

Combining the results obtained in this thesis with those available in the literature, it becomes clear that the structural characteristics and film performance on the low temperature CO oxidation critically depend on the support, and as such can be divided into two groups: those grown on Ag(111) and Au(111), on the one hand, and those on Pt(111) and Pd(111), on the other. Indeed, the as grown zinc oxide monolayer films on Pt(111) and Pd(111) are hydroxylated (even though that on Pd(111) is not proven experimentally yet). By contrast, the films on Au(111) and Ag(111) grown as bilayer from the onset and are graphene-like in nature without hydroxyls on the surface. In addition, more structural variations are observed on Pt(111) and Pd(111), whereas the films on Ag(111) and Au(111) show basically only one structure. The film on Cu(111) is less ordered and cannot be classified in any of the two groups.

To rationalize the support effects, we first refer to the surface energies [156], summarized in Table 1. A general trend is clear: films grown on surfaces which have a higher surface energy appears as monolayer, while those on surfaces with lower surface energy prefer a bilayer structure. According to Figure 3-18, a surface with higher surface energy is prone to be wetted by an oxide overlayer.

Pt(111)	Pd(111)	Cu(111)	Au(111)	Ag(111)
2.48	2.05	1.83	1.50	1.25
Mono-, bi-, multi-layer	Mono-, bilayer	Bilayer, "self-limiting" growth	Bilayer	Bilayer, "self-limiting" growth

Table 1. Surface energy (J/m^2) of the substrates and the morphology of films.

Another factor is the extent of lattice mismatch between the substrate and the zinc oxide, which may also affect the structure of the overlayer. The surface lattice constants of

Cu(111), Ag(111), Au(111), Pt(111) and Pd(111) surfaces are shown in Table 2. The Cu(111) has a 27.5 % lattice mismatch to the overlayer, which is the largest. As a consequence, the film is the least ordered. The extent of lattice mismatch on the other four substrates is similar. As a result, films on these substrates have larger domains.

	Surface lattice constant	Lattice mismatch to Wurtzite ZnO (3.25 Å)
Cu(111)	2.55 Å	27.5 %
Ag(111)	2.89 Å	11.1 %
Au(111)	2.88 Å	11.3 %
Pt(111)	2.77 Å	14.8 %
Pd(111)	2.75 Å	15.3 %

Table 2. Lattice constants of Cu(111), Ag(111), Pt(111) and Au(111) surfaces, and the lattice mismatch to zinc oxide.

The observed self-limiting growth may also be affected by substrate. As discussed earlier, hydroxylation and relaxation are the two mechanisms to cancel the inherent dipole moment on basal ZnO(0001) surfaces. On Ag(111), the film adopts the relaxation mechanism. This may be the reason why its growth is self-limited: The co-planar structure could not be maintained when it gets thicker as suggested by DFT. On the other hand, the Pt(111)-supported films, which adopt hydroxylation as the dipole cancellation mechanism, are able to grow thicker, albeit only OH-covered. This could be attributed to the fact that the hydroxyl density is increased in response to the increasing dipole moment accumulated in the thicker films.

As the reactivity of oxide surfaces may strongly depend on the degree of surface hydroxylation, our observation, that the zinc oxide films exhibit different hydroxylation behavior when the substrate is changed, provides the possibility to tune a model system to further elucidate the effects of hydroxylation on the reactivity of zinc oxide surfaces.

Finally, the structural diversity of the ZnO structures observed here for the film supported by Pt(111) suggests that ZnO-based materials must be considered very dynamic and not static. The surface could be even more dynamic and complex under reaction conditions.

Appendix: Film Thickness Determination Based on Auger Electron Spectroscopy

Spectroscopies are useful tools for determining the thicknesses of homogeneous extended thin films. In the literature [157], the mathematical expression reads:

$$d = c \times \lambda(E) \times \sin\theta \times ln(\frac{I_f/I_s}{I_f^0/I_s^0} + 1)$$

(Eq. a1)

where d: thickness

$\lambda(E)$: mean free path of the electron with kinetic energy E

Θ: the angle between the sample surface plane and the analyzer axis

I_f: signal of the film

I_s: signal of the substrate

I_f^0: signal of the film at infinite thickness

I_s^0: signal of the clean substrate

c: a constant

In the case of zinc oxide Pt(111), the I_s^0 was determined by measuring the clean Pt(111) surface. The I_f^0 could be obtained from the thick film, which shows saturated Zn signal; meanwhile the substrate signal almost disappeared. In the case of Ag(111), the I_s^0 could also be obtained from the clean Ag(111) surface; the I_f^0 could simply adopt the one obtained from the thick film grown on Pt(111), since they were measured with the same setup.

To determine precisely the film thickness from the formula, the remaining three constants should be determined. A more feasible way of making use of this model was to determine the relative film thickness of two films. To do that, equations from the two films were divided. By doing so, the c, λ and Θ could be cancelled out.

The Auger electron spectra of zinc oxide film on Pt(111) and Ag(111) and the in Figure a-1. The film thicknesses were determined by STM. The height of the Auger peaks is measured and summarized in Table 3.
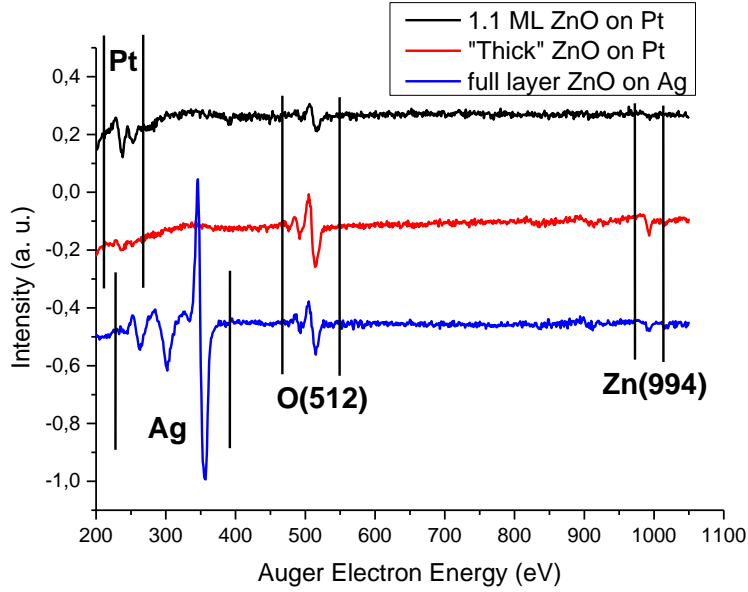
Figure a1. AES spectra of zinc oxide film on Pt(111) and Ag(111) with different thickness

Auger electron energy	1.1 ML zinc oxide/Pt(111)		full zinc oxide layer/Ag(111)		Saturate signals		
	Zn(994)	Pt(237)	Zn(994)	Ag(356)	Zn(994)	Pt(237)	Ag(356)
Intensity	0.017	0.11	0.033	0.95	0.059	0.20	2.0

Table 3. AES peak heights measured in Figure a1. The saturated Pt and Ag peak heights are measured from cleaned crystal surfaces.

Putting the values into the eq. (a1), we obtain

$$d_{(Ag)} = c \times \lambda \times sin\theta \times Ln \left(\frac{0.03277/0.945}{0.059/2.017} + 1 \right) = 0.78 \times c \times \lambda \times sin\,\theta \; ; \text{for the film on Ag(111)}$$

$$d_{(Pt)} = c \times \lambda \times sin\theta \times Ln\left(\frac{0.0167/0.1125}{0.059/0.196} + 1\right) = 0.40 \times c \times \lambda \times sin\,\theta \; ; \text{for the film on Pt(111)}$$

$$\rightarrow \quad \frac{d_{Ag}}{d_{Pt}} = \frac{0.78}{0.40} = 1.95$$

Therefore, the zinc oxide on Ag(111) is roughly twice as thick as that on Pt(111). Since STM results showed that the films on Pt(111) grows as a monolayer, we concluded that the film on Ag(111) is bilayer.

Abbreviations

AES: auger electron spectroscopy

ALD: atomic layer deposition

CVD: chemical vapor deposition

DFT: density functional theory

DLaTGS: deuterated L-alanine doped triglycine sulfate

FM: Frank-van der Merwe

FT: fourier transformation

HAS: helium atom scattering

h-BN: hexagonal boron nitride

HREELS: high resolution electron energy loss spectroscopy

IETS: inelastic electron tunneling spectroscopy

IRAS: infrared reflective absorption spectroscopy

LDOS: local density of states

LEED: low energy electron diffraction

MBE: molecular beam epitaxy

MCT: mercury cadmium telluride

MIM junction: metal-insulator-metal junction

MLE: monolayer equivalent

nc-AFM: non-contact atomic force microscope

PLD: pulsed laser deposition

PSTM: photon emission scanning tunneling microscope

PVD: physical vapor deposition

QMS: quadruple mass spectrometer

RHEED: reflection high-energy electron diffraction

SK: Stranski-Krastanov

SP-STM: spin-polarized scanning tunneling microscopy

STM: scanning tunneling microscopy

STS: scanning tunneling spectroscopy

SXRD: surface x-ray diffraction

TEM: transmission electron microscopy

TERS: tip-enhanced Raman spectroscopy

TPD: temperature-programmed desorption

UHV: ultra-high vacuum

VW: Vollmer-Weber

WKB semiclassical approximation: Wentzel-Kramers-Brillouin semiclassical approximation

XPS: X-ray photoemission spectroscopy

References

1. Morkoc, H. and Ü. Özgür, *Zinc Oxide Fundamentals, Materials and Device Technology*. 2009, Weinheim: Wiley-VCH.
2. Jagadish, V.A.C.a.C., *Zinc Oxide Bulk, Thin Films and Nanostructures - Chapter 1*, ed. C.J.a.S. Pearton. 2006: Elsevier.
3. Wang, Z.L., *Zinc oxide nanostructures: growth, properties and applications.* Journal of Physics-Condensed Matter, 2004. **16**(25): p. R829-R858.
4. Wang, Z.L., *Nanostructures of zinc oxide.* Materials Today, 2004. **7**(6): p. 26-33.
5. Mitra, P., A.P. Chatterjee, and H.S. Maiti, *ZnO thin film sensor.* Materials Letters, 1998. **35**(1-2): p. 33-38.
6. Zhang, R., A. Ludviksson, and C.T. Campbell, *THE CHEMISORPTION OF METHANOL ON CU FILMS ON ZNO(000(1)OVER-BAR)-O.* Catalysis Letters, 1994. **25**(3-4): p. 277-292.
7. Yoshihara, J. and C.T. Campbell, *Chemisorption of formic acid and CO on Cu particles on the Zn-terminated ZnO(0001) surface.* Surface Science, 1998. **407**(1-3): p. 256-267.
8. Gutierrez-Sosa, A., et al., *Modifying behaviour of Cu on the orientation of formate on ZnO(000(1)over-bar)-O.* Surface Science, 2001. **477**(1): p. 1-7.
9. Dulub, O., L.A. Boatner, and U. Diebold, *STM study of Cu growth on the ZnO(1010) surface.* Surface Science, 2002. **504**(1-3): p. 271-281.
10. Dulub, O., M. Batzill, and U. Diebold, *Growth of copper on single crystalline ZnO: Surface study of a model catalyst.* Topics in Catalysis, 2005. **36**(1-4): p. 65-76.
11. Ay, M., et al., *Structural properties of Cu clusters on the O-terminated ZnO (000(1)over-bar) surface.* Applied Surface Science, 2004. **226**(4): p. 405-411.
12. *Handbook of Heterogeneous Catalysis*, in *Handbook of Heterogeneous Catalysis*, G. Ertl, et al., Editors. 2008, WILEY-VCH Verlag GmbH & Co. KGaA: Weinheim, Germany.
13. Behrens, M., et al., *The Active Site of Methanol Synthesis over Cu/ZnO/Al2O3 Industrial Catalysts.* Science, 2012. **336**(6083): p. 893-897.
14. Yoshihara, J., J.M. Campbell, and C.T. Campbell, *Cu films on a Zn-terminated ZnO(0001) surface: structure and electronic properties.* Surface Science, 1998. **406**(1-3): p. 235-245.
15. Ernst, K.H., et al., *GROWTH-MODEL FOR METAL-FILMS ON OXIDE SURFACES - CU ON ZNO(0001)-O.* Physical Review B, 1993. **47**(20): p. 13782-13796.
16. Campbell, C.T., K.A. Daube, and J.M. White, *CU/ZNO(0001-BAR) AND ZNOX/CU(111) - MODEL CATALYSTS FOR METHANOL SYNTHESIS.* Surface Science, 1987. **182**(3): p. 458-476.
17. Ertl, G., *Reactions at surfaces: From atoms to complexity (Nobel lecture).* Angewandte Chemie-International Edition, 2008. **47**(19): p. 3524-3535.
18. Hammer, B. and J.K. Norskov, *Theoretical surface science and catalysis - Calculations and concepts*, in *Advances in Catalysis, Vol 45: Impact of Surface Science on Catalysis*, B.C. Gates and H. Knozinger, Editors. 2000. p. 71-129.
19. Bonzel, H.P., *ROLE OF SURFACE SCIENCE EXPERIMENTS IN UNDERSTANDING HETEROGENEOUS CATALYSIS.* Surface Science, 1977. **68**(1): p. 236-258.
20. Freund, H.-J., *Metal-supported ultrathin oxide film systems as designable catalysts and catalyst supports.* Surface Science, 2007. **601**(6): p. 1438-1442.
21. Shaikhutdinov, S. and H.J. Freund, *Ultrathin Oxide Films on Metal Supports: Structure-Reactivity Relations*, in *Annual Review of Physical Chemistry, Vol 63*, M.A. Johnson and T.J. Martinez, Editors. 2012. p. 619-633.

22.   Gao, F. and D.W. Goodman, *CO oxidation over ruthenium: identification of the catalytically active phases at near-atmospheric pressures.* Physical Chemistry Chemical Physics, 2012. **14**(19): p. 6688-6697.
23.   Over, H., *Surface Chemistry of Ruthenium Dioxide in Heterogeneous Catalysis and Electrocatalysis: From Fundamental to Applied Research.* Chemical Reviews, 2012. **112**(6): p. 3356-3426.
24.   Martynova, Y., S. Shaikhutdinov, and H.-J. Freund, *CO Oxidation on Metal-Supported Ultrathin Oxide Films: What Makes Them Active?* ChemCatChem, 2013. **5**(8): p. 2162-2166.
25.   Sun, Y.-N., et al., *The Interplay between Structure and CO Oxidation Catalysis on Metal-Supported Ultrathin Oxide Films.* Angewandte Chemie-International Edition, 2010. **49**(26): p. 4418-4421.
26.   Giordano, L., et al., *Oxygen-Induced Transformations of an FeO(111) Film on Pt(111): A Combined DFT and STM Study.* Journal of Physical Chemistry C, 2010. **114**(49): p. 21504-21509.
27.   Sun, Y.-N., et al., *When an Encapsulating Oxide Layer Promotes Reaction on Noble Metals: Dewetting and In situ Formation of an "Inverted" FeO(x)/Pt Catalyst.* Catalysis Letters, 2008. **126**(1-2): p. 31-35.
28.   Wöll, C., *The chemistry and physics of zinc oxide surfaces.* Progress in Surface Science, 2007. **82**(2-3): p. 55-120.
29.   Claeyssens, F., et al., *Growth of ZnO thin films - experiment and theory.* Journal of Materials Chemistry, 2005. **15**(1): p. 139-148.
30.   Tusche, C., H.L. Meyerheim, and J. Kirschner, *Observation of depolarized ZnO(0001) monolayers: Formation of unreconstructed planar sheets.* Physical Review Letters, 2007. **99**(2).
31.   *CRC handbook of Chemistry and Physics*. 73 ed. 1992, New York: CRC Press.
32.   Bates, C.H., R. Roy, and W.B. White, *NEW HIGH-PRESSURE POLYMORPH OF ZINC OXIDE.* Science, 1962. **137**(3534): p. 993-&.
33.   Ashrafi, A., et al., *Growth and characterization of hypothetical zinc-blende ZnO films on GaAs(001) substrates with ZnS buffer layers.* Applied Physics Letters, 2000. **76**(5): p. 550-552.
34.   Kresse, G., O. Dulub, and U. Diebold, *Competing stabilization mechanism for the polar ZnO(0001)-Zn surface.* Physical Review B, 2003. **68**(24).
35.   Heiland, G. and Kunstman.P, *POLAR SURFACES OF ZINC OXIDE CRYSTALS.* Surface Science, 1969. **13**(1): p. 72-&.
36.   Vanhove, H. and R. Leysen, *LEED STUDY ON POLAR SURFACES OF ZNO.* Physica Status Solidi a-Applied Research, 1972. **9**(1): p. 361-&.
37.   Becker, T., et al., *Interaction of hydrogen with metal oxides: the case of the polar ZnO(0001) surface.* Surface Science, 2001. **486**(3): p. L502-L506.
38.   Dulub, O., U. Diebold, and G. Kresse, *Novel stabilization mechanism on polar surfaces: ZnO(0001)-Zn.* Physical Review Letters, 2003. **90**(1).
39.   Staemmler, V., et al., *Stabilization of polar ZnO surfaces: Validating microscopic models by using CO as a probe molecule.* Physical Review Letters, 2003. **90**(10).
40.   Lyle, M.J., et al., *Coverage and charge-state dependent adsorption of carbon monoxide on the zinc oxide (0001) surface.* Physical Review B, 2010. **82**(16).
41.   Becker, T., et al., *Adsorption dynamics of CO on the polar surfaces of ZnO.* Journal of Chemical Physics, 2000. **113**(15): p. 6334-6343.

42. Debye, P., *Interferenz von Röntgenstrahlen und Wärmebewegung.* Annalen der Physik, 1913. **348**(1): p. 49–92.

43. Waller, I., *Zur Frage der Einwirkung der Wärmebewegung auf die Interferenz von Röntgenstrahlen.* Zeitschrift für Physik A, 1923. **17**: p. 398–408.

44. Batyrev, E.D. and J.C. van den Heuvel, *Modification of the ZnO(0001)-Zn surface under reducing conditions.* Physical Chemistry Chemical Physics, 2011. **13**(28): p. 13127-13134.

45. Onsten, A., et al., *Water Adsorption on ZnO(0001): Transition from Triangular Surface Structures to a Disordered Hydroxyl Terminated phase.* Journal of Physical Chemistry C, 2010. **114**(25): p. 11157-11161.

46. Kunat, M., et al., *Stability of the polar surfaces of ZnO: a reinvestigation using He-atom scattering.* Physical Review B (Condensed Matter and Materials Physics), 2002. **66**(8): p. 81402-1-3.

47. Shi, S.H., et al., *An ab initio study of the adsorption of CO on a Zn4O4 cluster with wurtzite-like structure.* Chemical Physics, 2003. **287**(1-2): p. 183-195.

48. Noei, H., et al., *The identification of hydroxyl groups on ZnO nanoparticles by infrared spectroscopy.* Physical Chemistry Chemical Physics, 2008. **10**(47): p. 7092-7097.

49. Dulub, O., L.A. Boatner, and U. Diebold, *STM study of the geometric and electronic structure of ZnO(0001)-Zn, (000(1)over-bar)-O, (10(1)over-bar0), and (11(2)over-bar0) surfaces.* Surface Science, 2002. **519**(3): p. 201-217.

50. Lauritsen, J.V., et al., *Stabilization Principles for Polar Surfaces of ZnO.* Acs Nano, 2011. **5**(7): p. 5987-5994.

51. Qiu, H., et al., *Ionization Energies of Shallow Donor States in ZnO Created by Reversible Formation and Depletion of H Interstitials.* Physical Review Letters, 2008. **101**(23).

52. Hovel, S., et al., *Pyridine adsorption on the polar ZnO(0001) surface: Zn termination versus O termination.* Journal of Chemical Physics, 2000. **112**(8): p. 3909-3916.

53. Ay, M., et al., *Structure and surface termination of ZnO films grown on (0001)- and (11(2)over-bar-0)-oriented Al2O3.* Thin Solid Films, 2006. **510**(1-2): p. 346-350.

54. Deinert, J.C., et al., *Ultrafast Exciton Formation at the ZnO(10(1)over-bar0) Surface.* Physical Review Letters, 2014. **113**(5).

55. Gao, Y.K., et al., *Probing the interaction of the amino acid alanine with the surface of ZnO(10(1)over-bar0).* Journal of Colloid and Interface Science, 2009. **338**(1): p. 16-21.

56. Wang, Y., et al., *Hydrogen induced metallicity on the ZnO(10(1)over-bar0) surface.* Physical Review Letters, 2005. **95**(26).

57. Yan, Y. and M.M. Al-Jassim, *Structure and energetics of water adsorbed on the ZnO(10(1)over-bar0) surface.* Physical Review B, 2005. **72**(23).

58. Wander, A. and N.M. Harrison, *An ab initio study of ZnO(10(1)over-bar0).* Surface Science, 2000. **457**(1-2): p. L342-L346.

59. Duke, C.B., et al., *LOW-ENERGY-ELECTRON-DIFFRACTION ANALYSIS OF ATOMIC GEOMETRY OF ZNO(1010).* Physical Review B, 1977. **15**(10): p. 4865-4873.

60. Wang, Y., et al., *Hydrogen induced metallicity on the ZnO(10(1)over-bar0) surface.* Physical Review Letters, 2005. **95**(26).

61. Yin, X.L., et al., *Adsorption of atomic hydrogen on ZnO(1010): STM study.* Physical Chemistry Chemical Physics, 2006. **8**(13): p. 1477-1481.

62. Diebold, U., L.V. Koplitz, and O. Dulub, *Atomic-scale properties of low-index ZnO surfaces.* Applied Surface Science, 2004. **237**(1-4): p. 336-342.

63.	Meyer, B., et al., *Partial dissociation of water leads to stable superstructures on the surface of zinc oxide.* Angewandte Chemie-International Edition, 2004. **43**(48): p. 6642-6645.

64.	Dulub, O., B. Meyer, and U. Diebold, *Observation of the dynamical change in a water monolayer adsorbed on a ZnO surface.* Physical Review Letters, 2005. **95**(13).

65.	Zuniga-Perez, J., et al., *Polarity effects on ZnO films grown along the nonpolar 11(2)over-bar0 direction.* Physical Review Letters, 2005. **95**(22).

66.	Li, M.-B., T.-X. Zhang, and L.-B. Shi, *Magnetic properties of N-doped(1120) ZnO thin films.* Acta Physica Sinica, 2011. **60**(9).

67.	Tasker, P.W., *STABILITY OF IONIC-CRYSTAL SURFACES.* Journal of Physics C-Solid State Physics, 1979. **12**(22): p. 4977-4984.

68.	Noguera, C. and J. Goniakowski, *Polarity in oxide nano-objects.* Chem Rev, 2013. **113**(6): p. 4073-105.

69.	Nilius, N., *Properties of oxide thin films and their adsorption behavior studied by scanning tunneling microscopy and conductance spectroscopy.* Surface Science Reports, 2009. **64**(12): p. 595-659.

70.	Barbier, A., et al., *Atomic structure of the polar NiO(111)-p(2 x 2) surface.* Physical Review Letters, 2000. **84**(13): p. 2897-2900.

71.	Finocchi, F., et al., *Stability of rocksalt (111) polar surfaces: Beyond the octopole.* Physical Review Letters, 2004. **92**(13).

72.	Wang, X.G., A. Chaka, and M. Scheffler, *Effect of the environment on alpha-Al2O3 (0001) surface structures.* Physical Review Letters, 2000. **84**(16): p. 3650-3653.

73.	Goniakowski, J., C. Noguera, and L. Giordano, *Prediction of uncompensated polarity in ultrathin films.* Physical Review Letters, 2007. **98**(20).

74.	Poon, H.C., et al., *Structure of the hydrogen stabilized MgO(111)-(1 x 1) surface from low energy electron diffraction (LEED).* Surface Science, 2006. **600**(12): p. 2505-2509.

75.	Kitakatsu, N., V. Maurice, and P. Marcus, *Local decomposition of NiO ultra-thin films formed on Ni(111).* Surface Science, 1998. **411**(1-2): p. 215-230.

76.	Kourouklis, H.N. and R.M. Nix, *THE GROWTH AND STRUCTURE OF ZNOX OVERLAYERS ON LOW-INDEX SILVER SURFACES.* Surface Science, 1994. **318**(1-2): p. 104-114.

77.	Weirum, G., et al., *Growth and Surface Structure of Zinc Oxide Layers on a Pd(111) Surface.* Journal of Physical Chemistry C, 2010. **114**(36): p. 15432-15439.

78.	Meyerheim, H.L., et al., *Wurtzite structure in ultrathin ZnO films on Fe(110): Surface x-ray diffraction and ab initio calculations.* Physical Review B, 2014. **90**(8).

79.	Stavale, F., N. Nilius, and H.-J. Freund, *STM Luminescence Spectroscopy of Intrinsic Defects in ZnO(000(1)over-bar) Thin Films.* Journal of Physical Chemistry Letters, 2013. **4**(22): p. 3972-3976.

80.	Deng, X., et al., *Growth of Single- and Bilayer ZnO on Au(111) and Interaction with Copper.* The Journal of Physical Chemistry C, 2013. **117**(21): p. 11211-11218.

81.	Schott, V., et al., *Chemical Activity of Thin Oxide Layers: Strong Interactions with the Support Yield a New Thin-Film Phase of ZnO.* Angewandte Chemie-International Edition, 2013. **52**(45): p. 11925-11929.

82.	Binnig, G., et al., *TUNNELING THROUGH A CONTROLLABLE VACUUM GAP.* Applied Physics Letters, 1982. **40**(2): p. 178-180.

83.	Binnig, G. and H. Rohrer, *SCANNING TUNNELING MICROSCOPY.* Helvetica Physica Acta, 1982. **55**(6): p. 726-735.

84.   R. Wiesendanger, e., *Scanning Tunneling Microscopy and Spectroscopy: Methods and Applications*. 1994, Cambridge University Press: Cambridge.

85.   Logan, R.M. and R.E. Stickney, *SIMPLE CLASSICAL MODEL FOR SCATTERING OF GAS ATOMS FROM A SOLID SURFACE.* Journal of Chemical Physics, 1966. **44**(1): p. 195-&.

86.   Thomson, G.P., *The analysis of surface layers by electron diffraction.* Proceedings of the Royal Society of London Series a-Containing Papers of a Mathematical and Physical Character, 1930. **128**(808): p. 649-661.

87.   Parratt, L.G., *SURFACE STUDIES OF SOLIDS BY TOTAL REFLECTION OF X-RAYS.* Physical Review, 1954. **95**(2): p. 359-369.

88.   Clarke, T.A., et al., *CHEMISORPTION OF CARBON-MONOXIDE ON PLATINUM(100) SURFACE - DEFINITION OF ELECTRONIC STATES BY PHOTOELECTRON-SPECTROSCOPY.* Chemical Physics Letters, 1975. **31**(1): p. 29-32.

89.   Gersten, J.I., *THEORY OF INELASTIC PROCESSES IN LOW-ENERGY ELECTRON-LOSS SPECTROSCOPY .1.* Physical Review, 1969. **188**(2): p. 774-&.

90.   Henderso.B and J.E. Wertz, *DEFECTS IN ALKALINE EARTH OXIDES.* Advances in Physics, 1968. **17**(70): p. 749-&.

91.   Bardeen, J., *TUNNELLING FROM A MANY-PARTICLE POINT OF VIEW.* Physical Review Letters, 1961. **6**(2): p. 57-&.

92.   Tersoff, J. and D.R. Hamann, *THEORY OF THE SCANNING TUNNELING MICROSCOPE.* Physical Review B, 1985. **31**(2): p. 805-813.

93.   Tersoff, J. and D.R. Hamann, *THEORY AND APPLICATION FOR THE SCANNING TUNNELING MICROSCOPE.* Physical Review Letters, 1983. **50**(25): p. 1998-2001.

94.   Chen, C.J., *ORIGIN OF ATOMIC RESOLUTION ON METAL-SURFACES IN SCANNING TUNNELING MICROSCOPY.* Physical Review Letters, 1990. **65**(4): p. 448-451.

95.   Hamers, R.J., *ATOMIC-RESOLUTION SURFACE SPECTROSCOPY WITH THE SCANNING TUNNELING MICROSCOPE.* Annual Review of Physical Chemistry, 1989. **40**: p. 531-559.

96.   Lang, N.D., *SPECTROSCOPY OF SINGLE ATOMS IN THE SCANNING TUNNELING MICROSCOPE.* Physical Review B, 1986. **34**(8): p. 5947-5950.

97.   Ekvall, I., et al., *Preparation and characterization of electrochemically etched W tips for STM.* Measurement Science & Technology, 1999. **10**(1): p. 11-18.

98.   Stipe, B.C., M.A. Rezaei, and W. Ho, *Single-molecule vibrational spectroscopy and microscopy.* Science, 1998. **280**(5370): p. 1732-1735.

99.   Lorente, N. and M. Persson, *Theory of single molecule vibrational spectroscopy and microscopy.* Physical Review Letters, 2000. **85**(14): p. 2997-3000.

100.   Bonca, J. and S.A. Trugman, *EFFECT OF INELASTIC PROCESSES ON TUNNELING.* Physical Review Letters, 1995. **75**(13): p. 2566-2569.

101.   Gimzewski, J.K., et al., *PHOTON-EMISSION WITH THE SCANNING TUNNELING MICROSCOPE.* Zeitschrift Fur Physik B-Condensed Matter, 1988. **72**(4): p. 497-501.

102.   Wiesendanger, R., et al., *TOPOGRAPHIC AND MAGNETIC-SENSITIVE SCANNING TUNNELING MICROSCOPE STUDY OF MAGNETITE.* Science, 1992. **255**(5044): p. 583-586.

103.   Wiesendanger, R., et al., *OBSERVATION OF VACUUM TUNNELING OF SPIN-POLARIZED ELECTRONS WITH THE SCANNING TUNNELING MICROSCOPE.* Physical Review Letters, 1990. **65**(2): p. 247-250.

104.   Stockle, R.M., et al., *Nanoscale chemical analysis by tip-enhanced Raman spectroscopy.* Chemical Physics Letters, 2000. **318**(1-3): p. 131-136.

105.   Pettinger, B., et al., *Nanoscale probing of adsorbed species by tip-enhanced Raman spectroscopy.* Physical Review Letters, 2004. **92**(9).

106. Busca, G., *The use of vibrational spectroscopies in studies of heterogeneous catalysis by metal oxides: An introduction.* Catalysis Today, 1996. **27**(3-4): p. 323-352.

107. Sogoshi, N., et al., *High-resolution infrared absorption spectroscopy of C-60 molecules and clusters in parahydrogen solids.* Journal of Physical Chemistry A, 2000. **104**(16): p. 3733-3742.

108. Pearce, H.A. and N. Sheppard, *POSSIBLE IMPORTANCE OF A METAL-SURFACE SELECTION RULE IN INTERPRETATION OF INFRARED-SPECTRA OF MOLECULES ADSORBED ON PARTICULATE METALS - INFRARED-SPECTRA FROM ETHYLENE CHEMISORBED ON SILICA-SUPPORTED METAL-CATALYSTS.* Surface Science, 1976. **59**(1): p. 205-217.

109. Greenler, R.G., *REFLECTION METHOD FOR OBTAINING INFRARED SPECTRUM OF A THIN LAYER ON A METAL SURFACE.* Journal of Chemical Physics, 1969. **50**(5): p. 1963-&.

110. Greenler, R.G., *INFRARED STUDY OF ADSORBED MOLECULES ON METAL SURFACES BY REFLECTION TECHNIQUES.* Journal of Chemical Physics, 1966. **44**(1): p. 310-&.

111. Greenler, R.G., *DESIGN OF A REFLECTION-ABSORPTION EXPERIMENT FOR STUDYING IR-SPECTRUM OF MOLECULES ADSORBED ON A METAL-SURFACE.* Journal of Vacuum Science & Technology, 1975. **12**(6): p. 1410-1417.

112. Hoffmann, F.M., *Infrared reflection-absorption spectroscopy of adsorbed molecules.* Surface Science Reports, 1983. **3**(2-3): p. 107-92.

113. Francis, S.A. and A.H. Ellison, *INFRARED SPECTRA OF MONOLAYERS ON METAL MIRRORS.* Journal of the Optical Society of America, 1959. **49**(2): p. 131-138.

114. Pendry, J.B., *Low energy electron diffraction : the theory and its application to determination of surface structure*. 1974, London: Acad. Pr.

115. Davisson, C. and L.H. Germer, *The scattering of electrons by a single crystal of nickel.* Nature, 1927. **119**: p. 558-560.

116. Davisson, C. and L.H. Germer, *Diffraction of electrons by a crystal of nickel.* Physical Review, 1927. **30**(6): p. 705-740.

117. Stroscio, J.A., D.T. Pierce, and R.A. Dragoset, *HOMOEPITAXIAL GROWTH OF IRON AND A REAL-SPACE VIEW OF REFLECTION-HIGH-ENERGY-ELECTRON DIFFRACTION.* Physical Review Letters, 1993. **70**(23): p. 3615-3618.

118. Lüth, H., *Solid Surfaces, Interfaces and Thin Films*. 2001: Springer.

119. Garrett, S.J., *Surface Diffraction and the Reciprocal Lattice.*

120. Grant, J.T. and D. Briggs, *Surface Analysis by Auger and X-ray Photoelectron Spectroscopy*. 2003, Chichester: IM Publ.

121. Persson, L., *Pierre Auger - A life in the service of science.* Acta Oncologica, 1996. **35**(7): p. 785-787.

122. Garin, F., *Mechanism of NOx decomposition.* Applied Catalysis a-General, 2001. **222**(1-2): p. 183-219.

123. Siegbahn, K., et al., *ESCA applied to free molecules*. 1969, Amsterdam: North Holland.

124. Darwin, H., *Zur Formelmäßigen Darstellung der Ionisationsquerschnitte gegenüber Elektronenstoß.* Z. Phys., 1961. **164**: p. 513-521.

125. CHO, A.Y. and J.R. ARTHUR, *MOLECULAR BEAM EPITAXY* Progress in Solid-State Chemistry, 1975. **10**(3): p. 157-191.

126. Brown, I.G., *Cathodic arc deposition of films.* Annual Review of Materials Science, 1998. **28**: p. 243-269.

127. Singh, R.K. and J. Narayan, *PULSED-LASER EVAPORATION TECHNIQUE FOR DEPOSITION OF THIN-FILMS - PHYSICS AND THEORETICAL-MODEL.* Physical Review B, 1990. **41**(13): p. 8843-8859.

128. Tarng, M.L. and G.K. Wehner, *AUGER-ELECTRON SPECTROSCOPY STUDIES OF SPUTTER DEPOSITION AND SPUTTER REMOVAL OF MO FROM VARIOUS METAL-SURFACES.* Journal of Applied Physics, 1972. **43**(5): p. 2268-&.

129. Jasinski, J.M., B.S. Meyerson, and B.A. Scott, *MECHANISTIC STUDIES OF CHEMICAL VAPOR-DEPOSITION.* Annual Review of Physical Chemistry, 1987. **38**: p. 109-140.

130. George, S.M., *Atomic Layer Deposition: An Overview.* Chemical Reviews, 2010. **110**(1): p. 111-131.

131. Shiotari, A., et al., *Local Characterization of Ultrathin ZnO Layers on Ag(111) by Scanning Tunneling Microscopy and Atomic Force Microscopy.* Journal of Physical Chemistry C, 2014. **118**(47): p. 27428-27435.

132. Yang, B., S. Shaikhutdinov, and H.-J. Freund, *Tuning Spatial Distribution of Surface Hydroxyls on a Metal-Supported Single-Layer Silica.* Journal of Physical Chemistry Letters, 2014. **5**(10): p. 1701-1704.

133. Schiek, M., et al., *Water adsorption on the hydroxylated H-(1x1) O-ZnO(0001) surface.* Physical Chemistry Chemical Physics, 2006. **8**(13): p. 1505-1512.

134. Meyer, B., *First-principles study of the polar O-terminated ZnO surface in thermodynamic equilibrium with oxygen and hydrogen.* Physical Review B, 2004. **69**(4).

135. Lindsay, R., et al., *ZnO(000(1)over-bar)-O surface structure: hydrogen-free (1x1) termination.* Surface Science, 2004. **565**(2-3): p. L283-L287.

136. Brune, H., *Microscopic view of epitaxial metal growth: nucleation and aggregation.* Surface Science Reports, 1998. **31**(4-6): p. 121-229.

137. Thiel, P.A., et al., *Adsorbate-enhanced transport of metals on metal surfaces: Oxygen and sulfur on coinage metals.* Journal of Vacuum Science & Technology A, 2010. **28**(6): p. 1285-1298.

138. Geim, A.K. and K.S. Novoselov, *The rise of graphene.* Nature Materials, 2007. **6**(3): p. 183-191.

139. Golberg, D., et al., *Boron Nitride Nanotubes and Nanosheets.* Acs Nano, 2010. **4**(6): p. 2979-2993.

140. Emtsev, K.V., et al., *Towards wafer-size graphene layers by atmospheric pressure graphitization of silicon carbide.* Nature Materials, 2009. **8**(3): p. 203-207.

141. Loeffler, D., et al., *Growth and Structure of Crystalline Silica Sheet on Ru(0001).* Physical Review Letters, 2010. **105**(14).

142. Boscoboinik, J.A., et al., *Modeling Zeolites with Metal-Supported Two-Dimensional Aluminosilicate Films.* Angewandte Chemie-International Edition, 2012. **51**(24): p. 6005-6008.

143. Picozzi, S., et al., *Ozone adsorption on carbon nanotubes: The role of Stone-Wales defects.* Journal of Chemical Physics, 2004. **120**(15): p. 7147-7152.

144. An, W., et al., *Adsorption and surface reactivity on single-walled boron nitride nanotubes containing stone-wales defects.* Journal of Physical Chemistry C, 2007. **111**(38): p. 14105-14112.

145. Boukhvalov, D.W. and M.I. Katsnelson, *Chemical Functionalization of Graphene with Defects.* Nano Letters, 2008. **8**(12): p. 4373-4379.

146. Ugeda, M.M., et al., *Missing Atom as a Source of Carbon Magnetism.* Physical Review Letters, 2010. **104**(9).

147. Tunvir, K., et al., *Mechanical properties of carbon nanotubes with randomly distributed vacancy defects.* Journal of the Korean Physical Society, 2007. **51**(6): p. 1940-1947.

148. Mielke, S.L., et al., *The role of vacancy defects and holes in the fracture of carbon nanotubes.* Chemical Physics Letters, 2004. **390**(4-6): p. 413-420.

149. Yazyev, O.V. and S.G. Louie, *Topological defects in graphene: Dislocations and grain boundaries.* Physical Review B, 2010. **81**(19).

150. Yang, F., et al., *Identification of 5-7 defects in a copper oxide surface.* J Am Chem Soc, 2011. **133**(30): p. 11474-7.

151. Haruta, M., et al., *LOW-TEMPERATURE OXIDATION OF CO OVER GOLD SUPPORTED ON TIO2, ALPHA-FE2O3, AND CO3O4.* Journal of Catalysis, 1993. **144**(1): p. 175-192.

152. Martynova, Y., et al., *CO oxidation over ZnO films on Pt(111) at near-atmospheric pressures.* Journal of Catalysis, 2013. **301**: p. 227-232.

153. Boffa, A.B., et al., *LEWIS ACIDITY AS AN EXPLANATION FOR OXIDE PROMOTION OF METALS - IMPLICATIONS OF ITS IMPORTANCE AND LIMITS FOR CATALYTIC REACTIONS.* Catalysis Letters, 1994. **27**(3-4): p. 243-249.

154. Schoiswohl, J., et al., *Vanadium oxide nanostructures on Rh(111): Promotion effect of CO adsorption and oxidation.* Surface Science, 2005. **580**(1-3): p. 122-136.

155. Pan, Q., et al., *Reactivity of Ultra-Thin ZnO Films Supported by Ag(111) and Cu(111): A Comparison to ZnO/Pt(111).* Catalysis Letters, 2014. **144**(4): p. 648-655.

156. Skriver, H.L. and N.M. Rosengaard, *SURFACE-ENERGY AND WORK FUNCTION OF ELEMENTAL METALS.* Physical Review B, 1992. **46**(11): p. 7157-7168.

157. Ross, D. and M. Maier, *THICKNESS MEASUREMENT OF THIN DIELECTRICS WITH ELECTRON-SPECTROSCOPY.* Fresenius Zeitschrift Fur Analytische Chemie, 1989. **333**(4-5): p. 488-491.